MECHANICAL PROPERTY AND HYDROGEN SORPTION IN MG BASED NANOLAYERS

A Dissertation

by

BYOUNGSOO HAM

Submitted to the Office of Graduate and Professional Studies of
Texas A&M University
in partial fulfillment of the requirements for the degree of

DOCTOR OF PHILOSOPHY

Chair of Committee,	Xinghang Zhang
Committee Members,	Haiyan Wang
	Karl T. Hartwig
	Raymundo Arroyave
Head of Department,	Andreas Polycarpou

December 2013

Major Subject: Mechanical Engineering

ABSTRACT

Hydrogen storage technology is vital for the application of hydrogen as an alternative fuel for sustainable energy related applications. Mg is a promising light-weight material that has superior hydrogen storage capacity (7.6 wt. % of hydrogen) and low cost for large scale applications. However, the stability of Mg hydride is a key challenge for on-board applications of Mg. Bulk Mg hydride has a tetragonal crystal structure (referred to as T-MgH_2), and desorbs H at ~ 573K. In contrast the application of H for automobile fuel cells requires a H_2 desorption temperature at ~ 350K. In spite of active studies in the past decade, such a goal has not been achieved for practical application of T-MgH_2.

This thesis focuses on tackling this challenge and consists of several major components.

First we have demonstrated that stress-induced orthorhombic Mg hydride (O-MgH_2) is thermodynamically destabilized at ~ 373K or lower. This destabilization arises from a large tensile stress in single layer O-MgH_2 bonded to a rigid substrate, or a compressive stress due to the large volume change incompatibility in Mg/Nb multilayers. H desorption occurred at room temperature in O-MgH_2 10 nm / O-NbH 10 nm multilayers. These studies provide key insight into the mechanisms that can significantly destabilize Mg hydride and other type of metal hydrides.

Second, we have shown that the morphology of DC magnetron sputtered Mg thin films on rigid SiO_2 (substrate) varied from a continuous dense morphology to a porous columnar structure when the films grew thicker. Thermal desorption spectroscopy studies show that thinner dense MgH_2 films desorb H_2 at a lower temperature than thicker porous MgH_2 films. The influence of stress on the formation of the metastable MgH_2 phase and consequent reduction of H sorption temperature are discussed.

Finally we investigated the microstructure and mechanical behavior of Mg/Nb multilayers, with an with an individual layer thickness, h, of 2.5 to 200 nm because it is desirable to have inherently stable multilayers for cyclic hydrogenation applications. High resolution TEM studies reveal the formation of metastable Mg with a body-centered cubic (bcc) structure along the interface in multilayers with h of 5 nm or less. As h decreases, the hardnesses of multilayers increase and approach a maximum of ~ 2.7 GPa at a few nm layer thickness. The strengthening mechanisms in Mg/Nb multilayers are discussed.

ACKNOWLEDGEMENTS

First, I must thank my advisor, Dr. Xinghang Zhang for his support, guidance, and encouragement during my studies here at Texas A&M University. Without his guidance, I would never have arrived this far. I thank my committee members, Drs. Ted Hartwig, Raymundo Arroyave, and Haiyan Wang for their guidance and support throughout the course of this research. I also thank Dr. Wang for the use of her laboratory facilities.

I wish to thank my collaborators from Anchalee Junkeaw from Dr. Arroyave's group, Dr. Yang Ren from Argonne national lag, and Drs. Jarek Majewski and Peng Wang from Los Alamos National Laboratory, for their direct contributions to this work. I also thank Dr. Zhou and Dr. Jinhee Park from Chemistry department, and Dr. Ravi K. Arvapally, Dr. Ushasree Kaipa and Dr. Mohammad A. Omary from University of North Texas for the experimental help. I want to thank former Zhang research group members, Drs. Osman Anderoglu, Engang Fu, and Nan Li for their guidance as I began my graduate school career. I also want to thank my friends and coworkers, Dr. Danial Bufford, Steven Rios, Dr. Kaiyuan Yu, Yue Liu, Youxing Chen, Dr. Cheng Sun, David Foley, Shreyas Balachandran, for contributions during meeting discussions, for help to get through this course of journey. Finally, my deepest appreciation goes to my parents and sister for their unconditional faith and love. I owe this degree to all of them.

I acknowledge financial support by NSF-CBET, Energy for Sustainability program, under grant no. 0932249. Use of the Advanced Photon Source was supported by the U.S. Department of Energy, Office of Science, Office of Basic Energy Sciences, under Contract No. DE-AC02-06CH11357. I also acknowledge the Texas A&M University Microscopy Center and Materials Characterization Facility for the use of numerous microscopes and other instruments.

DEDICATION

This dissertation is dedicated to:

The memory of my grandparents, Jonghyup Ham and Hyunjeong Choi

My parents, Kyungchun Ham and Younghee Jeong

My sister, Sungyoun Ham

And to My wife, Nayung Yu

TABLE OF CONTENTS

Page

LIST OF FIGURES

Page

LIST OF TABLES

Page

CHAPTER I

INTRODUCTION AND LITERATURE REVIEW

I.1 Hydrogen storage in general

I.1.1 Hydrogen and hydrogen as alternative fuels

Hydrogen is an important type of energy carriers. A majority of the easy-to-get oil has already been found, and it may take more energy to extract the remaining fossil fuels than the energy they contain. Under the pressure of finite fossil fuel resources, continuous increase of oil prices, and environmental problems related to the use of fossil fuel, there is growing consensus on energy security. Hydrogen fuel has become a viable alternative candidate since it is environmentally benign and there is abundant source of hydrogen (shown in Figure 1). The advantages of hydrogen as the next generation energy carrier include clean by-product (water), and 3-4 times higher energy density per unit weight compared to fossil fuels. [1, 2]

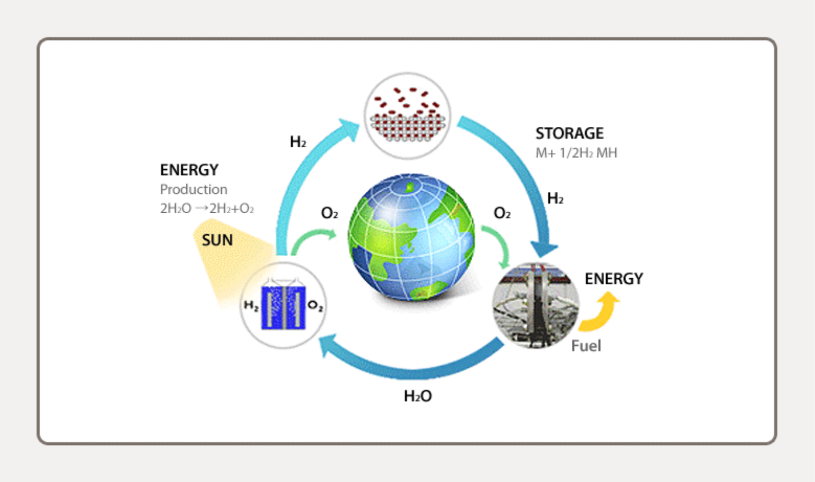

Figure 1. Hydrogen is a clean and renewable eco-friendly energy source that does not generate pollutants at combustion.

Most of hydrogen is made by reacting natural gas with high temperature steam to separate the hydrogen from the carbon. Although this method is accompanied by the CO_2 production, the emission is still lower than that of burning the same amount of natural gas. Hydrogen can be acquired by electrolysis of water, but it is a relatively energy intensive process.

Hydrogen powered fuel cells could replace batteries in many portable applications including automobiles, and satisfy residential and commercial electrical needs. For many of these applications, it is imperative to achieve high storage efficiency and subsequent release of hydrogen at practical temperature. It remains a challenge to meet these technical criteria due to a lack of efficiency and cost competitive hydrogen storage materials [3]. The “ideal” commercial H_2 storage system must be cost-effective, light-weight and compact, can store a high volumetric density of hydrogen, have both accessible energetics for activation and low temperature release, have high stability against moisture and O_2 for extended cycles, have minimum energy loss during charge and discharge of H_2 and have a high degree of reversibility [4].

I.1.2 Physical hydrogen storage

In this section, categories of hydrogen storage methods will be introduced and their hydrogen storage properties are evaluated for automotive applications.

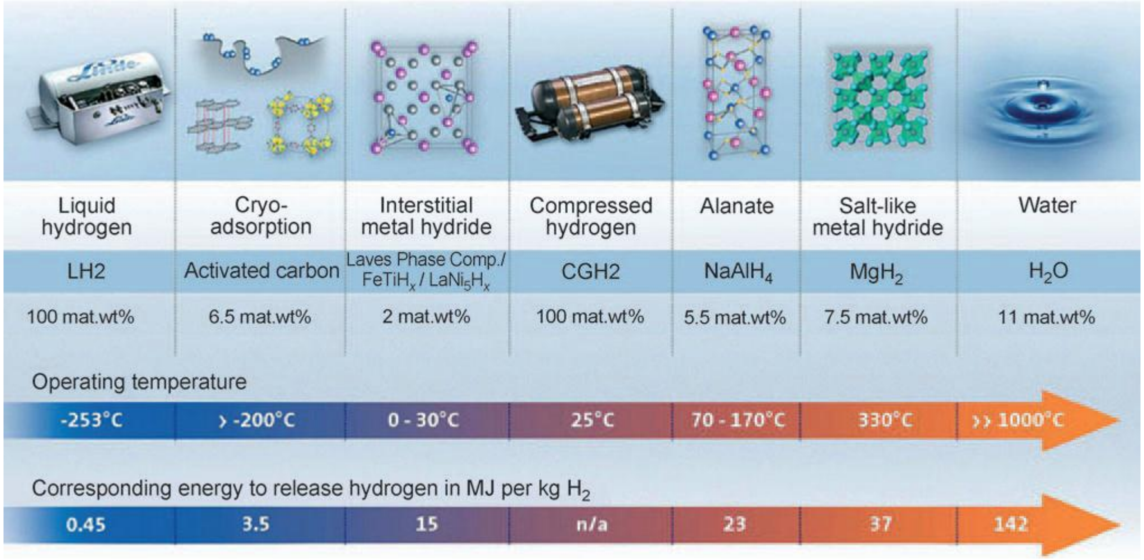

Figure 2. Several hydrogen storage technologies and their operating conditions [5].

Physical storage methods can be generally categorized as three sub-technologies below (Figure 2).

(1) Compressed gaseous hydrogen (CGH2), 35-70 MPa, room temperature

(2) Liquid hydrogen (LH2), 0.1-1 MPa, -253 °C

(3) Cryoadsorption on high-surface-area materials, 0.2-0.5 MPa, -193 °C

Currently, the physical storage technologies, and in particular CGH2 and LH2, are most mature; most prototypes of fuel-cell powered cars use one of these storage systems. 70MPa CGH2 is considered to be the state-of-the art technology [6].

I.1.2.1 Compressed gaseous hydrogen (CGH2)

Compressed gaseous hydrogen vessel (shown in Figure 3) can store about 5-6 kg of hydrogen on board for automobiles to achieve a driving distance of 500 km. Due to limited available space on vehicles, a high operation pressure of 35-70 MPa is necessary.

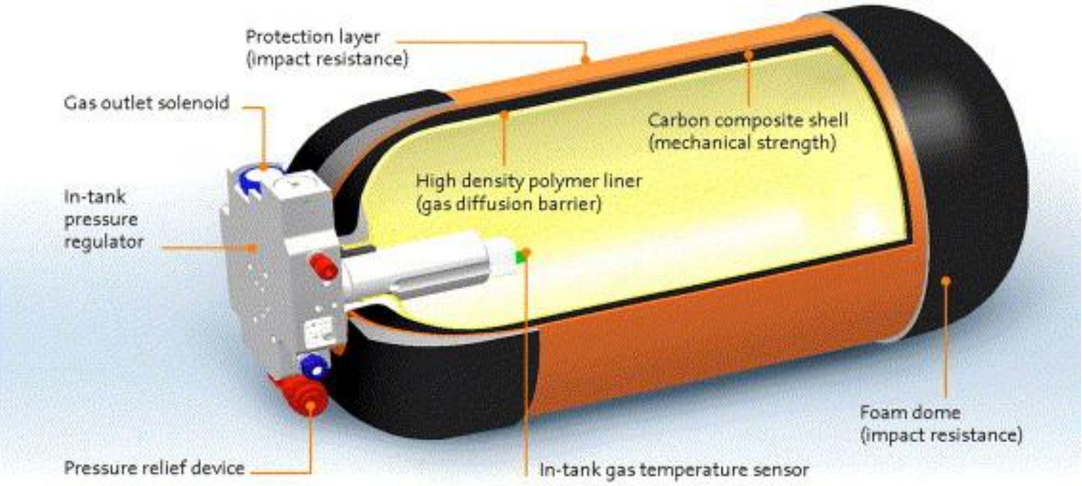

Figure 3. Type IV compressed gaseous hydrogen vessel [5].

When working at such high pressures, special vessel designs must be implemented. Due to space availability on vehicles, cylinders would be the preferred geometry. When anticipating increasing the volume stored inside a pressure vessel, extending the vessel length and not the diameter is preferable. Also, high-strength materials, such as carbon composites, should be used. Other options would lead to a correspondingly thicker wall. Thus the usage of small- to mid-scale pressure vessels makes more sense. Despite volumetric limitations of the CGH2 technology, this option yields the best overall technical performance to date and shows the highest maturity for automotive applications. Furthermore, it is feasible to refill an empty CGH2 system completely within three minutes [5].

I.1.2.2 Liquid hydrogen (LH2)

The use of liquid hydrogen requires an ultra low storage temperature, -253 °C [7]. For any cryogenic tank system, the use of a very efficient multilayer vacuum superinsulation is required, consisting of approximately 40 layers of foils as radiation shields. The wrapping around the cylindrical part, inlets and outlets connections is highly demanding [8]. Another disadvantage is the cooling loss during refilling of hydrogen at the station. The complete transfer line has to be cooled down to -253 °C to avoid additional evaporational loss. Thus even though the volumetric storage density of LH2 is slightly higher than CGH2 systems, most automobile manufacturers are hesitant for the usage of LH2 system. In addition, the design flexibility of LH2 systems is not really better than CGH2 tank systems [9].

I.1.2.3 Cryoadsorption on high-surface-area materials

Adsorption is a borderline situation between physical and chemical storage, and it is mostly categorized as a physical storage technology. The difference between cryoadsorption and chemical storage in a hydride is shown in Figure 4 [6]. Adsorptive storage solutions need an extremely large quantity of liquid nitrogen for cooling purposes and this is a significant engineering challenge for automotive applications. Furthermore, it creates additional costs which make this solution highly unattractive. Therefore, more sophisticated and advanced heat management technologies and tank operating strategies are required to provide a technically convenient way for storing acceptable amount of hydrogen.

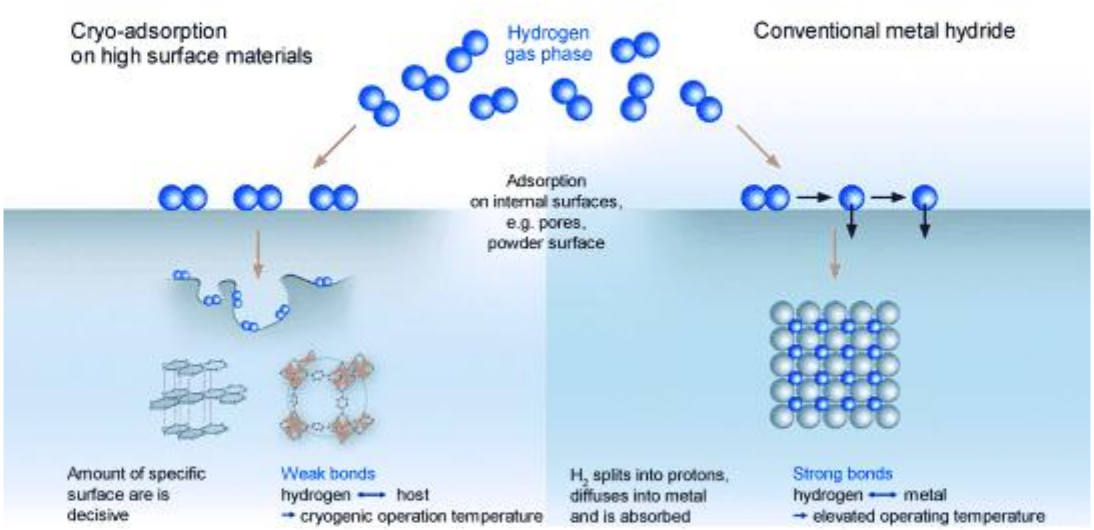

Figure 4. Representation of cryoadsorption and chemical storage in a hydride.

I.1.2.4 Zeolites

Zeolites are microporous, aluminosilicate minerals commonly used as commercial adsorbents [10]. Weitkamp et al. [11] reported a relationship between the amount of encapsulated hydrogen and the size of the exchanged cation in zeolite A. However, it showed the low hydrogen uptake of 9.2 cm^3/g (0.082 wt.%) at 300 °C under 10 MPa pressure. The storage capacity of zeolite samples can be increased substantially when loaded at liquid nitrogen temperatures. Jhung et al. [12] studied hydrogen adsorption on sodium forms of faujasite and found a hydrogen storage capacity of 1.5 wt.% at 77 K. The close relationship between the BET surface area of zeolite and the hydrogen uptake capacity at low temperature was noticed [13]. The zeolitic material ITO-33 [14] was predicted to have the storage capacity about 2.5 wt.%, which is one of the highest, if it is filled by liquid hydrogen. Thus, little attention has been paid to this media as a hydrogen storage material in technical applications.

I.1.2.5 Nanostructured Carbon

Nanostructured carbon materials, such as activated carbons of different origin, multiwall carbon nanotubes (MWNT), single wall carbon nanotubes (SWNT), carbon nanohorns, and carbon cloth, have been studied for hydrogen storage. Although extremely high sorption capacities over carbon nanotubes were reported, in some of the first reports (a storage capacity of 67 wt.% of hydrogen for graphitic nanofibers [15]), it is now widely accepted that these results were erroneous. And more consistent data have been published in the last few years, suggesting that the adsorption on carbon nanotubes and nanohorns also roughly obeys the same scaling behavior as observed for other carbon samples [6]. Thus it appears highly unlikely that carbon-based materials will be developed with a sufficient hydrogen storage capacity.

I.1.2.6 Metal organic frames(MOFs)

Metal Organic Frameworks (MOFs) attract attention as materials for adsorptive hydrogen storage because of their exceptionally high specific surface areas and chemically tunable structures [16]. They are crystalline compounds consisting of metal ions or clusters coordinated to often rigid organic molecules to form one-, two-, or three-dimensional structures that can be porous [17]. MOFs show exceedingly high surface area and they are the lightest known crystalline materials with densities down to 0.21

g/cm^3 and have gained considerable interest because of their capability of storing hydrogen and light hydrocarbons, such as methane [18] in their frameworks. Many MOFs are highly porous and these materials show high possibilities for gas storage applications [19-21]. Compared to an empty gas cylinder, a MOF-filled gas cylinder can store more gas because of adsorption that takes place on the surface of MOFs. (Note that molecular hydrogen adsorbs to the surface, not atomic hydrogen.) Furthermore, MOFs are free of dead-volume, so there is almost no loss of storage capacity as a result of space-blocking by non-accessible volume [22].

I.1.3 Chemical hydrogen storage

I.1.3.1 Complex hydrides-Alanates

In complex metal hydrides, hydrogen is covalently bound to a metal (or, as in the case of boron, a non-metal) atom to form a complex anion. Aluminum hydrides (alanates) have been considered promising materials for on-board hydrogen storage applications because of their high storage capacity. Lithium and sodium salts are commercially available; which is another attractive feature of alanates. Among a variety of alanate compounds with light cations for hydrogen storage, sodium analate ($NaAlH_4$) is the most intensively studied reversible complex aluminum hydride (shown in Figure 5) and promising hydrogen carrier due to its high hydrogen storage capacity and thermodynamic properties.

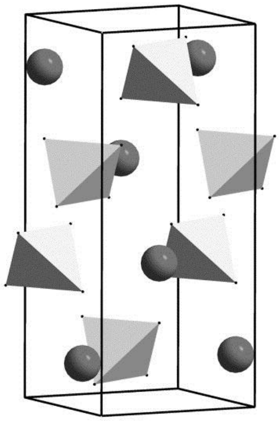

Figure 5. Crystal structure of $NaAlD_4$. The complex AlH_4- anions are depicted as tetrahedral and the Na cations as black spheres [23].

$NaAlH_4$ has a reversible hydrogen content of 5.6 wt.% H and it decomposes in three steps: [24]

First step: $3NaAlH_4$ -> Na_3AlH_6 + 2Al + $3H_2$ (3.7 wt.% H)

Second step: Na_3AlH_6 -> 3NaH + Al + $3/2H_2$ (1.8 wt.% H)

The first decomposition step has an equilibrium pressure of 1 bar at ~ 30 °C and the second step has a pressure of 1 bar at ~ 130 °C. The third step occurs at too high temperature, thus this step is not considered for a technical application. Bogdanović [25] showed that $NaAlH_4$ can be used as a solid reversible hydrogen storage material by doping it with titanium compounds. One of the most frequently used doping precursors is $TiCl_3$.

$TiCl_3 + 3NaAlH_4 \rightarrow Ti + 3Al + 3Nacl + 6H_2$

The active catalytic species is produced during treatment of the material in a ball-milling procedure [26-28]. During ball-milling process, a dopant is highly dispersed within the hydride material, which is necessary for good kinetics in solid-state reactions. Some other sodium analate compounds with Sc, Ce and Pr were reported in 2006 [29]. Other complex hydrides that have a high hydrogen content are the alkaline earth compounds $Mg(AlH_4)_2$ [30, 31], and $Ca(AlH_4)_2$. With a total hydrogen content of 9.3 wt % H_2 for the magnesium compound and 7.9 wt % H_2 for the calcium compound, both materials are in principle potential hydrogen storage materials [6].

It appears that a practical hydrogen storage system based on alanates would most likely require off-board recharging. Currently, only sodium alanate can be directly charged under hydrogen pressure, and thus until new highly economical chemical processes for the regeneration of alanates are developed, it is the only member of this class of materials which is a plausible candidate for practical hydrogen storage for vehicular applications. Despite the problems discussed above, Ti-doped sodium alanate to date stands as the hydrogen storage material with the best combination of materials properties that are suited for vehicular hydrogen storage [32].

I.1.3.2 Metal Hydrides

In contrast to the classical complex hydrides (hydrogen is covalently bound to a metal or, as in the case of boron, a non-metal atom to form a complex anion), interstitial sites are occupied with hydrogen atoms in metal hydrides. First, hydrogen molecules dissociate at the surface of host metal, and the hydrogen typically occupies interstitial sites in the host lattices. Such bulk transition metals form interstitial binary hydrides when exposed to hydrogen. These systems are usually non-stoichiometric, with variable amounts of hydrogen atoms in the lattice.

The most popular hydrogen storage alloys are the AB5–type compounds (Figure 6) $LaNi_5$, first reported by Van Vught et al. in 1970 [33], shows the hydrogen content of $LaNi_5H_6$ corresponding to roughly 1.4 wt % and an equilibrium pressure of 0.2 MPa at room temperature [34]. The high price of lanthanum and relatively low gravimetric storage capacity of the alloy make this material unattractive for on-board hydrogen storage.

AB2 compounds also have been explored; however, hydrogen storage capacity of AB2-type compounds can reach up to 2 wt % H_2. For instance, $ZrCr_2$ and $ZrMn_2$ shows 1.94 and 1.79 wt.% H respectively [35]. “A” is an element with high affinity for hydrogen and “B” is later transition metals from V to Ni. These materials are cheaper compared to the $LaNi_5$ alloy (A=Ti, Zr or a mixture, Mg; B=V, Cr, Fe, Mn), but their hydrogen equilibrium pressures are not sufficiently high at room temperature for fuel cell applications [6]. The storage capacities of the intermetallic hydrides are not high enough to meet the requirements for an on-board storage system; targets for on-board hydrogen storage of DOE by 2015 is the system meets 5.5 wt% gravimetric density, 40 g/L volumetric density, and operation condition under ~ 85 °C and 12 bar.

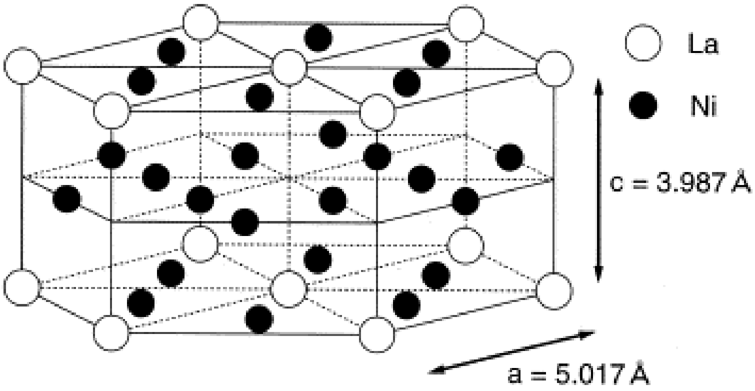

Figure 6. The crystal structure of LaNi5 with the hexagonal CaCu5 structure. [36]

I.1.4 Hydrogen sorption in metal hydride

I.1.4.1 Reaction between metal and hydrogen

The hydrogen molecule dissociates in the process of entering the absorbing metal and the resulting hydrogen occupies one or more of the available types of interstitials sites in the metal lattice. Reaction kinetics has to be addressed in order to meet the practical requirements of reloading time and delivery of hydrogen to the fuel cell for adequate performance. The reaction between hydrogen and metals involves heterogeneous solid-gas reactions and thus multiple energy barriers limit the rate of the (de)hydriding reaction [37].

The reaction of metal with hydrogen consists of five distinct steps shown in Figure 7, the dissociation of hydrogen molecules, chemisorption (recombination), the surface penetration of hydrogen ions/atoms within the metal particle, the nucleation of the β phase (diffusion), and finally the diffusion of hydrogen through the hydride layer that has formed around the particle (hydride nucleation and growth) [37].

The hydrogen atoms contribute their electron to the band structure of the metal. Far from the metal surface, the potential of a hydrogen molecule and of two hydrogen atoms are separated by the dissociation energy ($H_2 \rightarrow 2H$, E_D=435.99 kJ mol^{-1}). The first attractive interaction of the hydrogen molecule approaching the metal surface is the Van der Waals force leading to the physisorbed state ($E_{Phys} \approx 10$ kJ^{-1}) approximately one hydrogen molecule radius (≈ 0.2 nm) from the metal surface. Closer to the surface, the hydrogen has to overcome an activation barrier for dissociation and formation of the hydrogen metal bond. The height of the activation barrier depends on the surface elements involved. Hydrogen atoms sharing their electron with the metal atoms at the surface are then in the chemisorbed state ($E_{Chem} \approx 50$ kJ^{-1} H_2). The chemisorbed hydrogen atoms may have a high surface mobility, interact with each other, and form surface phases at sufficiently high coverage. In the next step, the chemisorbed hydrogen atom can jump in the subsurface layer and finally diffuse on the interstitial sites through the host metal lattice [2].

The slowest step determines the overall kinetic rate, and the experimentally measured kinetics represents the kinetics of the slowest part in each phase of the reaction. The kinetic curve at each step has a characteristic form, which can be formulated as equations relating the transformed phase fraction to time. Thus, it is possible to deduce the rate-limiting step of the kinetics, if a good fit of experimental data with a specific kinetic equation can be obtained [38]. Efforts over the past years to overcome kinetic limitations have been quite successful in particular for metal hydrides for which nanostructures and surface catalysis have led to a significant improvement of (de)hydriding kinetics [37].

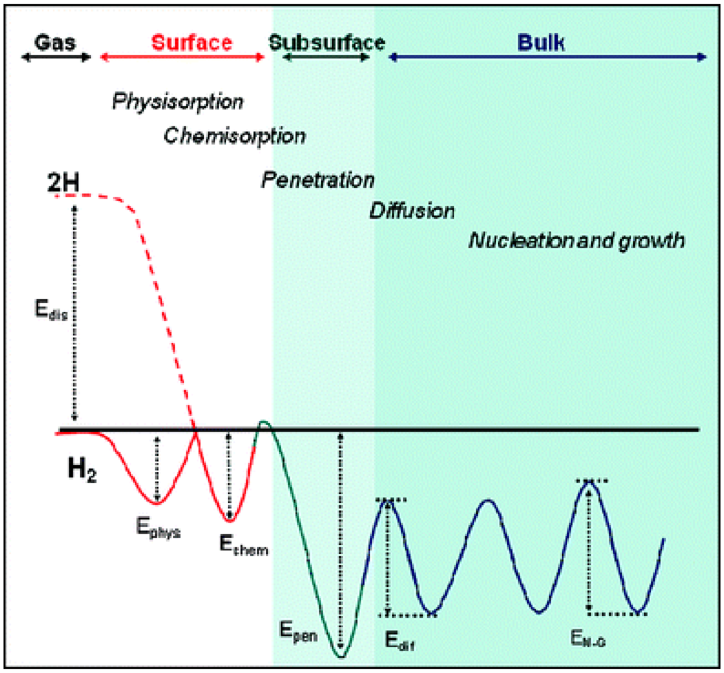

Figure 7. Lennard-Jones potential diagram corresponding to the successive energy barriers encountered by hydrogen during absorption/desorption in a metal. E_{phys}: energy for hydrogen physisorption, E_{chem}: energy for hydrogen chemisorption, E_{pen}: energy for hydrogen penetration in the subsurface, E_{dif}: energy for hydrogen diffusion in the bulk, and E_{N-G}: energy for the nucleation and growth of the hydride phase [37].

I.1.5 Mg hydride

I.1.5.1 Thermodynamics of hydrogenation

MgH_2 has a very high reversible storage capacity, a gravimetric capacity (7.6 wt.% H), making it in a very attractive hydrogen storage medium in principle. High capacity of hydrogen storage along with the fairly accessible and low cost of pure magnesium makes magnesium a promising medium for hydrogen storage applications. Upon hydrogenation, Mg with a hcp structure transforms into a rutile structure, i.e. tetragonal beta-MgH_2 shown in Figure 8 [39]. The rutile phase transforms into the metastable orthorhombic structure (gamma-MgH_2) under 9 GPa pressure (HP1-phase), and further to another orthorhombic phase (HP2-phase) at around 17 GPa [40]. The difference is in the arrangement of the hydrogen atoms, which form an octahedron around the central Mg atom shown in Figure 8.

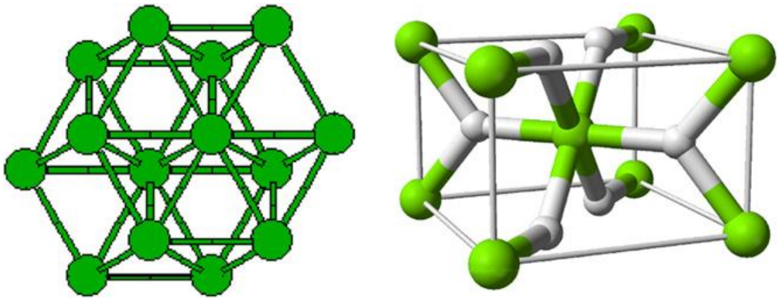

Figure 8. Crystal structure of Magnesium (Left) and tetragonal magnesium Hydride (MgH2) (Right).

However, a major disadvantage of MgH_2 is its extremely slow absorption and desorption kinetics, arising both from diffusion limitations and high oxidation sensitivity of the Mg surface, hindering the dissociation of hydrogen molecules. Figure 9 shows the high stability of MgH_2.The kinetics of hydrogenation of Mg is limited by several factors, including the formation of an MgO barrier impermeable to H, the low diffusion rate of H inside in Mg, the mobility of the metal/hydride interface during hydrogenation and the limited dissociation rate of H into Mg. The kinetics of absorption is considered to be controlled by chemical reaction, absorption of H, or permeation of adsorbed H through the surface [41, 42]. Numerous studies have aimed to overcome the kinetic limitations. The addition of catalyst elements can improve the dissociation rate of hydrogen. A short diffusion length can be accomplished by reducing the particle (grain) size by ball-milling, for example [43-45].

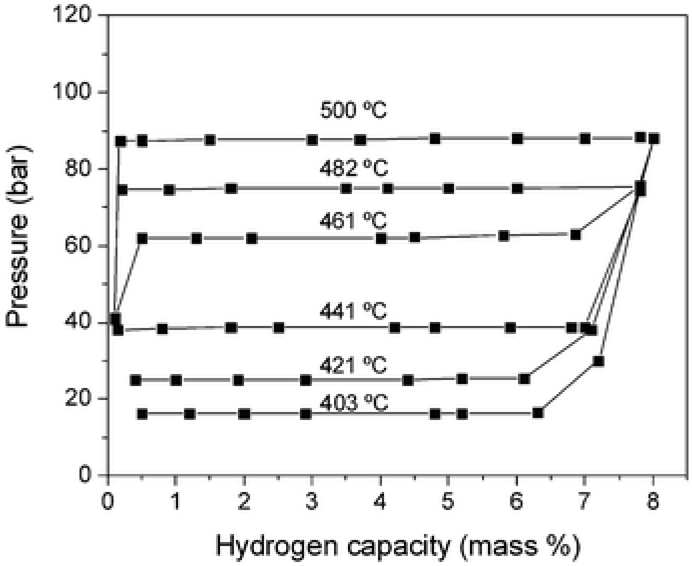

Figure 9. PCI of the Norsk Hydro Mg powder, particle size 25–40 µm, in the temperature range 403–500 °C [46].

Besides kinetic limitations, MgH_2 is also highly stable. MgH_2 has a large formation enthalpy of -74.7 kJ/mol H_2 and an entropy of 130 J/K mol H_2 [1, 47]. It is a high-temperature metal hydride (300 °C) with a minimum operating pressure of 0.1

MPa. Extensive experimental efforts have been made to modify Mg based systems to improve its hydrogen sorption characteristics.

I.1.5.2 Nanostructured Mg alloy

The hydrogenation rate in Mg decreases as thickness of hydride layers increases after the formation of MgH_2 layer, and becomes zero after reaching a critical thickness of MgH_2 ~ 50 µm [48]. Several approaches have been used to improve H sorption kinetics in Mg. Mechanical alloying can lead to several changes by introducing grain boundaries (GBs). GBs provide fast diffusion path for hydrogen and act as nucleation sites for MgH_2, and thus the refinement of grain size leads to the increase of hydrogenation kinetics. Mechanically milled MgH_2 (Figure 10) showed hydrogen absorption at 300 °C and desorption at 350 °C with faster kinetics compared to unmilled counterparts [49]. Nanocrystalline (nc) Mg with high-angle GBs prepared by mechanical milling can expedite the kinetics, but nanograins coarsen during thermal desorption [50, 51]. MgH_2, produced by milling pure Mg powder under hydrogen atmosphere [52], showed the improvement of the hydrogenation kinetics.

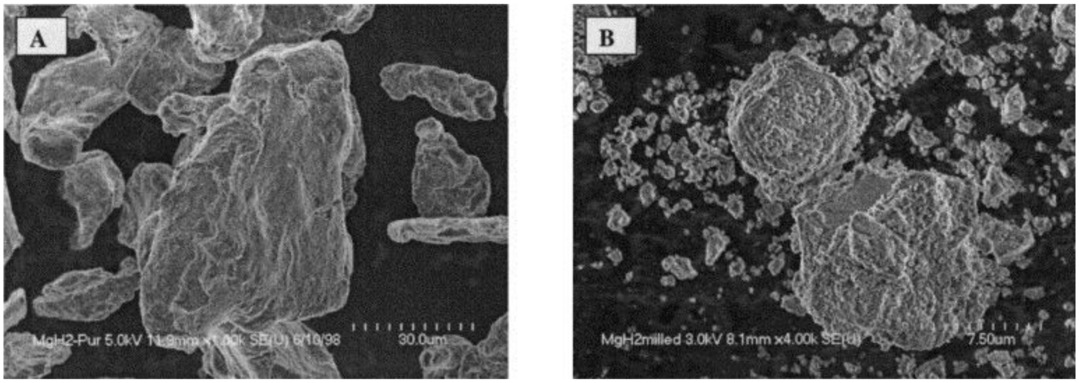

Figure 10. SEM micrographs of MgH_2 before (A) and after milling for 20 h (B). The specific surface area before and after milling was 1.2 $m^2\ g^{-1}$ and 9.9 $m^2\ g^{-1}$, respectively, as measured using the BET method.

I.1.5.3 Nanograins with catalyst

To enhance the kinetics even further in Mg-based nc materials, a variety of catalyst and additives (metals and transition-metal oxides) have been incorporated [51, 53-56]. Transition metals dissociate hydrogen molecules and enable them to diffuse and penetrate along GBs between Mg and catalysts acting as nucleation sites for the hydride phase.

Mg_2Ni was reported by Reilly [57] in 1968 for the first time, and became the most popular alloy since ball milled Mg with Ni dramatically improved kinetics. The addition of one atomic percent of nickel to magnesium showed the hydrogen capacity increase by 50%, ten times faster dehydrogenation rate than Mg, 100 °C lower temperature for onset of hydrogenation and 50 °C lower temperature for onset of dehydrogenation [58]. However, as Mg and other transition metals do not form any intermetallic compound, the hydride phase is more difficult to synthesize [59].

Mg-Al system [60] exhibits lower hydride formation enthalpy due to a slightly endothermic disproportionation reaction. However this alloy shows a lower gravimetric hydrogen density in the hydrogenated product. MgH_2 powders were ball milled with 5wt. % Nb and 5wt.% V [61]. The hydrogenation kinetics in MgH_2–Nb nanocomposite is similar to MgH_2–V system. The activation energies measured for different processes indicate that the presence of a metastable niobium hydride phase decreases the energy barrier for dehydrogenation of MgH_2. It is believed that transition metals such as Nb and V act as hydrogen pumps, facilitating both hydrogen absorption and desorption [37]. SEM images of MgH_2 powders ball milled with V are shown in Figure 11.

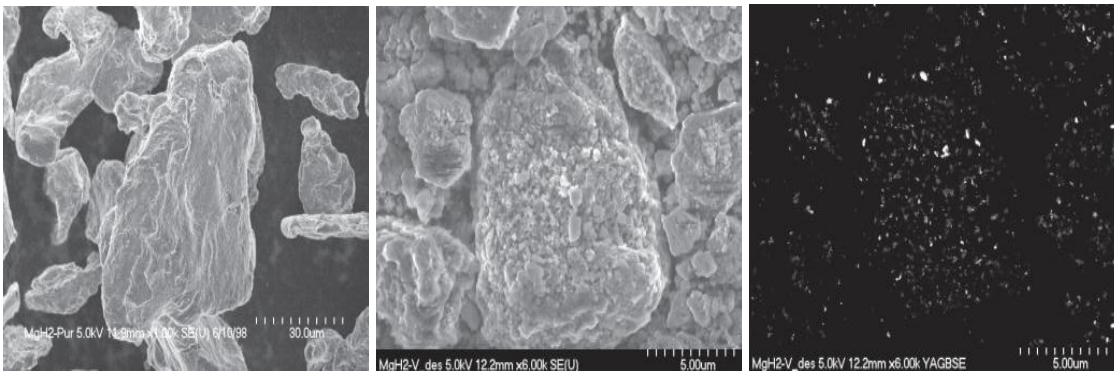

(a) **(b)** **(c)**

Figure 11. SEM micrographs of unmilled MgH_2 (a), nanocrystalline MgH_2 +5 at.%V composite (b), and backscattered electron image of nanocrystalline MgH_2 +5 at.%V composite (c) where the white marks represent vanadium particles.

BCC $Mg_{50}Co_{50}$ alloy was produced by 200 hours ball milling [62]. The maximum hydrogen absorption content was 2.7 mass% when the Co content was 40 at.%, but, this system was irreversible. Vajo et al. showed that thermodynamic destabilization in metal hydrides can be achieved by using certain additives that form new compounds during dehydrogenation [63-65]. Also many supersaturated Mg solid solutions are not stable; i.e., they decompose upon hydrogenation [66]. However, a majority of these additives have little influence on absorption temperature.

Metal oxides act as catalytic additives to MgH_2 to expedite hydrogen diffusion. Among the different oxides i.e. Nb_2O_5, TiO_2, V_2O_5, Cr_2O_3, Mn_2O_3, Fe_3O_4, CuO, SiC; Nb_2O_5 were shown to have better performance in comparison to the other oxides (Figure 12) [59]. MgH_2 powders ball milled with Nb_2O_5 catalyst increased the BET specific surface area of powders and showed hydrogen sorption at 200 °C [67].

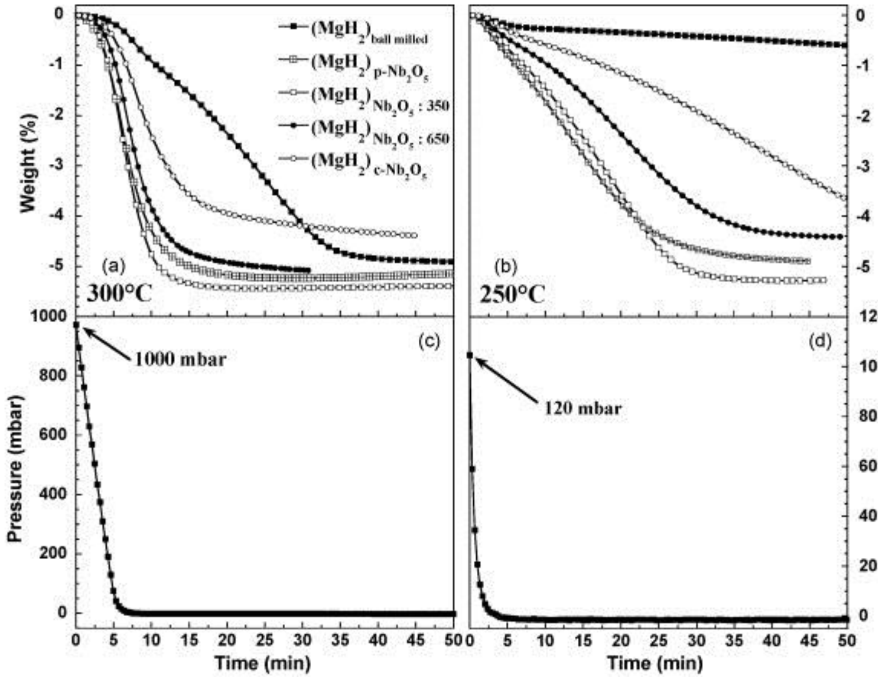

Figure 12. Hydrogen desorption kinetics of $(MgH_2)_{ball\ milled}$ and selected $(MgH_2)_{catalyst}$ at (a) 300 °C and (b) 250 °C, and their corresponding pressure (c) and (d) during desorption, respectively.

Cr_2O_3 doped MgH_2 showed improved absorption kinetics but decreased desorption rate by a factor of four after 1000 cycles at 300 °C [68]. Fe_2O_3 and Fe_3O_4 were ball milled with Mg in hydrogen atmosphere with 300 – 400 nm particle sizes, and showed 5-6 wt% H release. But rehydrogenated composite released only 4 – 4.4 wt% H, indicating degradation during cycling. To reduce formation enthalpy of MgH2, other hydrogen absorbing alloys were added to MgH_2, such as $LaNi_5$, FeTi, $ZrCr_2$, $ZrMn_2$, TiCrMnV. The combination of MgH_2 with other light hydrides is the other route, such as $LiBH_4$, $NaBH_4$ $Ca(BH_4)_2$ which form MgB_2 during desorption and be reversibly hydrogenated [59].

I.1.5.4 Co-sputtered Mg film

Mg-based thin films are an alternative way to improve properties of Mg for hydrogen storage. Thin films provide a large surface area, fast charging/discharging rate for hydrogen. Thin film studies can be also used for screening purpose with the attempt to search for appropriate alloys that can be scaled up as bulk materials subsequently.

Mg thin films are actively studied as model systems for understanding of hydrogen sorption kinetics [69-73]. Mg film with Pd cap layer showed low absorption/desorption temperatures [70], however, interfacial intermixing of Mg and Pd occurs during hydrogenation [74]. To destabilize MgH_2 formation and decomposition, transition metal catalysts were added on Mg matrix and the hydrogen sorption kinetics were improved [75-81]. Transition metal catalysts can be incorporated into Mg by co-sputtering [82-85]. Mg-Ti thin film showed cycling capability [84-86]. Baldi et, al.

observed that co-sputtered Mg-Ti film shows coherent crystalline grain between Mg and Ti and TiH_2 exhibits an accidental equality in terms of molar volumes with Mg causing fcc MgH_2 structure instead of rutile type [84]. Co-sputtered Mg-Nb25 at. % thin film showed the formation of a meta-stable bcc alloy with the enthalpy of -52 kJ/mole H_2 [87]. However, the hydride films desorbed hydrogen at 448 K and a deterioration of the Mg and Nb was observed after extended cycling.

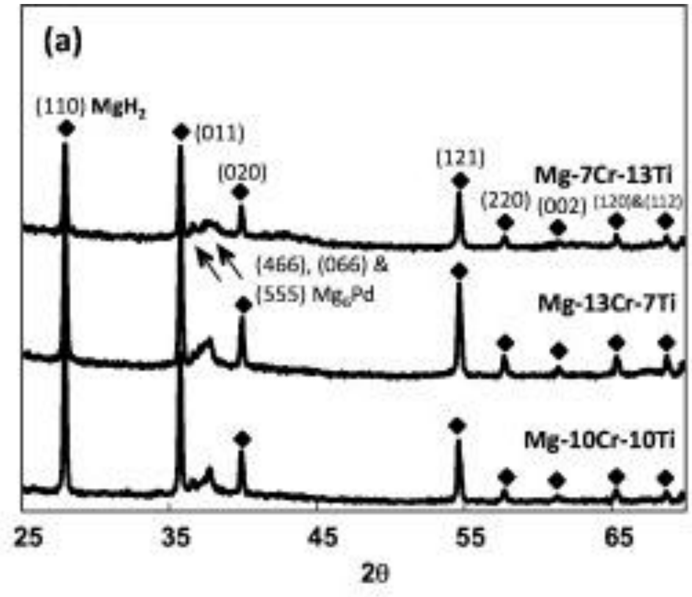

Figure 13. (a) Indexed X-ray diffraction pattern of the postcycled Mg–Cr–Ti alloys in the absorbed state. (b) Bright field STEM micrograph and EDXS elemental maps of Mg, Cr, Ti, and Ta in the Mg-10 at. % Cr-10 at. %Ti postcycled (absorbed) samples. An arrow points to the same region in the micrographs, an asterisk marks a Ta flake [83].

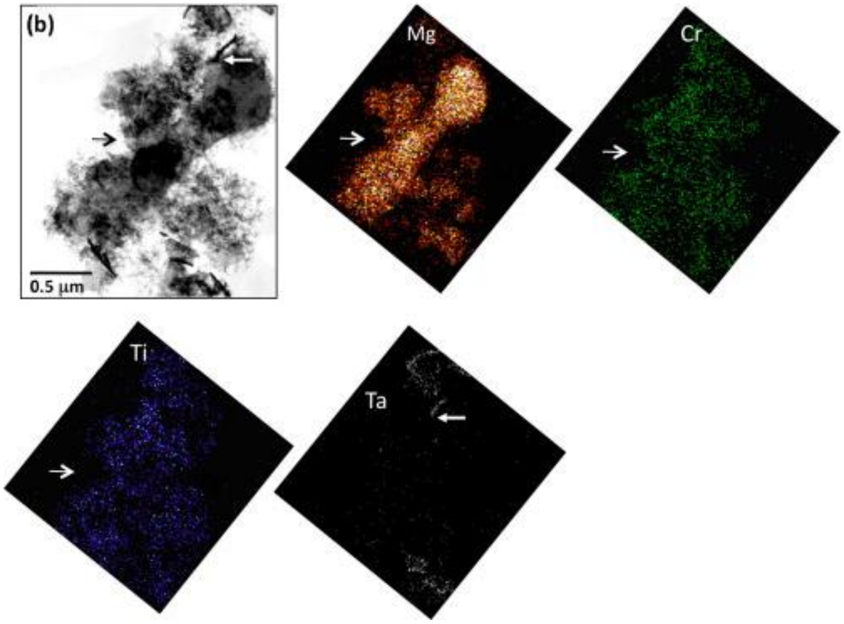

Figure 13. Continued.

Mg-Cr-Ti co-sputtered film in Figure 13 showed the enhanced kinetics due to nanoscale dispersed Cr-Ti phase in Mg matrix. A reduced diffusion distances led to accelarted sorption kinetics [83]. Mg-Ni-Ti ternary thin film exhibited formation enthalpy of -40 kJ/mol H_2 [88, 89]. Mg-rich Mg-Ni-Cu co-sputtered film showed the availability of cycling over 100 times at 200 °C [90]. These films showed two absorption stages: Mg absorbs hydrogen catalyzed by intermetallic Mg_2Ni, and absorption of H by Mg_2Ni and/or Mg_2Cu intermetallics. Pd-decorated Mg blades prepared by oblique incident angle thermal deposition also had a low desorption temperature of 373 K [91].

Some neutron reflectivity (NR) studies for deuterium absorption kinetics in co-sputtered Mg based thin films were reported by Canadian groups [92-96]. $Mg_{70}Al_{30}$ thin film with Ta/Pd bilayer was investigated by NR at room temperature. $Mg_{70}Al_{30}$ film can store up to 5 wt. % H and it was found that Ta layer improves the sorption kinetics and the interfaces in which elastic constraints at the interfaces may affect the nucleation barrier for the formation of hydrides [92, 93]. Mg0.8Fe0.1Cr0.1 co-sputtered film stored 5 wt.% of hydrogen and had fast sorption kinetics at 200 °C up to 140 cycles. The authors concluded that the avoidance of the formation of a blocking MgD2 layer in the early stage of absorption leads to a fast hydrogen absorption kinetics [94].

Mg-based alloy thin films also exhibit interesting optical property variations after hydrogen loading [80, 97-100], while Mg-Ni film showed degradation after 170 cycles [101]. The Mg-Ti [97, 102] and Mg-Ni [98] films also showed optical and switchable mirror effect.

I.1.5.5 Mg based nanolayers

Certain Mg-based multilayer films with addition of proper catalysts showed improved H sorption kinetics. With Pd cap layer, Mg film shows kinetics improvement due to the elastic strain interaction at the interface between Mg and Pd. Mg/Pd multilayer showed significantly enhanced hydrogenation at 100 °C/1 bar and the enhanced performance was explained by cooperative phenomena [70]. It described a mechanism of catalyst-facilitated hydrogenation and desorption of hydrogen. Figure 14 illustrates that the hydrogen absorbed by Pd will lead to tensile stress that facilitates hydrogenation of Mg film. The opposite process occurs during desorption; that is desorption of H_2 from Pd leads to compressive stress that enables rapid dissociation of H_2 from Mg hydride.

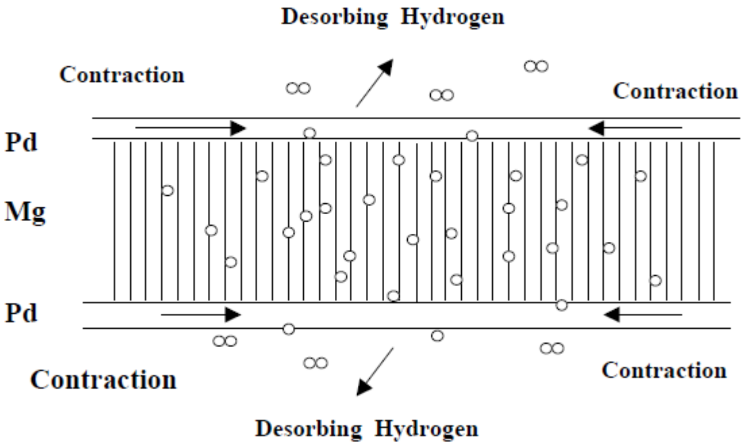

Figure 14. Schematic diagram of hydrogenated Pd/Mg/Pd thin film [70].

Multilayered Mg films with transition metal catalysts have been studied by several groups. The catalyst layers can catalyze the diffusion of hydrogen during sorption process. A Mg/Mm–Ni multilayer film was prepared by thermal evaporation and showed the hydrogenation at 200°C and dehydrogenation at 250 °C [103]. The authors also reported $Mg_{2.9}Ni/MmM_5$ multilayer film prepared by DC sputtering has the hydrogen absorption content of 5 wt% at 250 °C [104]. Baldi et, al. provided a way to tune the thermodynamics of a metal-hydrogen system by elastic constraints [105]. Miscible elements such as Ni and Pd showed a clamping effect on the thermodynamic properties (higher plateau pressure). Mg/Ti multilayers also exhibited enhanced hydrogen sorption properties [106]. Ti layers absorbed hydrogen prior to Mg layers due to their lower hydride formation enthalpy. Ouyang et, al. prepared MgNi/Pd multilayer films on Ni substrate by DC sputtering and measured hydrogen uptake of 4.6 wt.% at room temperature and desorption of 3.4 wt.% after three cycles [107]. Mg/Ni multilayer films were prepared by DC/AC sputtering and annealed below 623 K in vacuum. Polycrystalline Mg_2Ni films were acquired after annealing and the structural and optical properties of Mg2Ni switchable mirrors were discussed [108]. Hydrogenation and dehydrogenation behavior of multilayered stacks of Pd/Fe–Ti/(Mg/Al/Mg)/Fe–Ti/Pd grown by e-beam evaporation techniques was investigated by Ferrer et, al. [109]. Films absorb hydrogen at 150 °C under 1 atm and Al addition has beneficial effect on hydrogenation characteristics of Mg films, without much difference in the desorption temperature.

In spite of kinetic enhancements of hydrogenation process in several Mg-based multilayers, the thermodynamic stability of MgH_2 remained little affected [70, 86, 106, 110-114], and significant interface intermixing frequently occurred during hydrogenation in certain multilayers [112, 115]. The formation of intermetallic compound can be prevented by insertion of a buffer layer [105]. Also clamped metal hydride thin films show modified thermodynamics and varying hydrogen solubility in metal-hydrogen systems [116-118].

I.2 Mechanical properties of metallic multilayers

Metallic multilayers with individual layer thickness (h) of hundreds to a few nm exhibit unique properties [119-121]. By using physical vapor deposition (PVD), multilayers can be synthesized with various individual layer thickness and constituents. These multilayers typically exhibit much greater mechanical strength than their bulk counterparts [122-126]. Interface and layer thickness play a significant role in strengthening of these multilayers [127-130]. Indentation hardness of multilayers increases significantly as h decreases, and maximum hardness may reach ½ to 1/3 of theoretical strength when h is a few nm thick [119, 131-135]. Various mechanisms were proposed to explain the size (layer thickness) dependent enhancement of hardness of multilayers. One example of Cu-based multilayers with different individual layer thickness is shown in Figure 15.

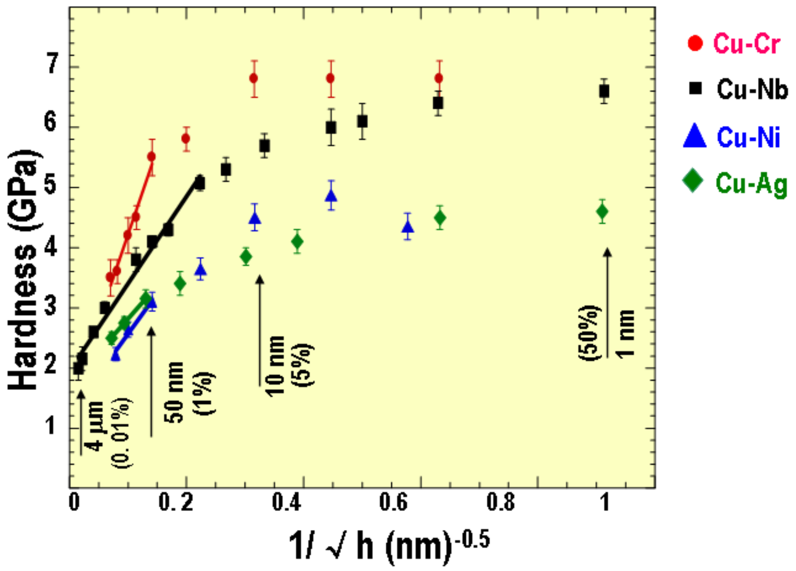

Figure 15. The dependence of hardness on layer thickness (h) for Cu-Cr, Cu-Nb, Cu-Ni and Cu-Ag multilayers. Linear fit at larger h is consistent with the Hall-Petch model. At lower h, the Hall-Petch model breaks down

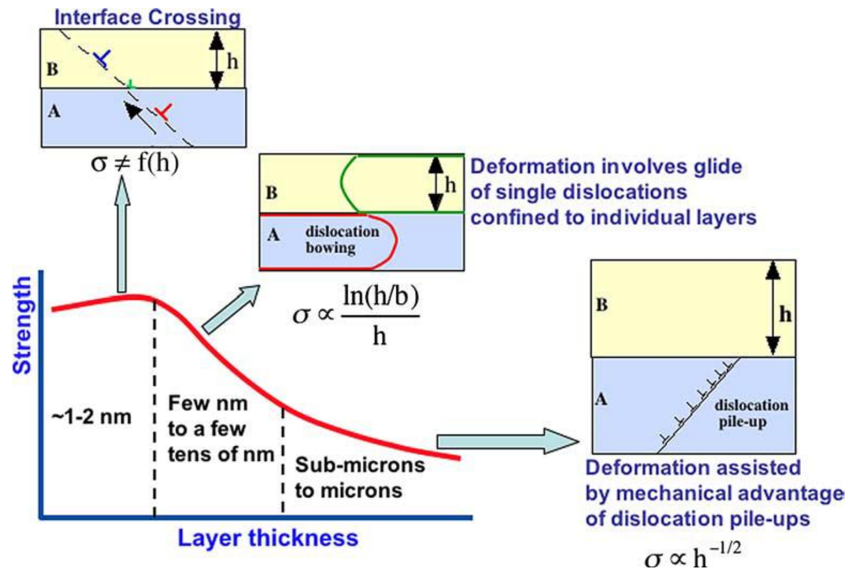

Figure 16. Schematic illustration of the dislocation mechanisms of multilayer strength operative at different length scale [132].

The evolution of H can be explained in three regimes as a function of h shown in Figure 16. When h is larger than a few tens of nanometers (> 50 nm), indentation hardness increases linearly with $1/\sqrt{h}$. In this region, strengthening can be typically interpreted by the Hall-Petch model [136] where dislocations pile up against layer interfaces. When h decreases further from a few tens to several nm, hardness typically deviate from the linear dependence on $1/\sqrt{h}$. Strengthening may be explained by the confined layer slip (CLS) mechanism based on the Orowan model that considers the bowing of single dislocations within layers [119]. When h decreases to a few nm, the hardness may increase (Cu/Nb), or reach a plateau (Cu/Cr) or even decreases (Cu/Ni) [131]. Numerous strengthening mechanisms have been considered at this length scale.

When the layer constituent has a large shear modulus mismatch, Koehler stress (elastic moduli mismatch) due to the image force of dislocations plays an important role in determining the peak strength [137-139]. On the other hand, if a large lattice mismatch exists, coherency stress arises and it can change the dislocation core structure and elastic constants, and hence increases the interface barrier strength in Cu/Ni multilayers [138].

Also coherency stresses can act as retarding force against the glide of dislocations in the layers. In Cu/Nb multilayers, a dislocation spreads its core at the interface (since interface is weak in shear), making it difficult to be reemitted into the opposite layers, and hence the interface is a strong barrier to the transmission of dislocations [123, 140]. Meanwhile at such a small length scale, certain constituents of the layer could form metastable phases, such as bcc Co in Co/Cr [141], fcc Ti in Ti/Al [141] and Ti/Ni [142], and bcc Cu in Cu/Mo [143] and Cu/Nb nanolayers [144]. In these cases, strengthening mechanisms have been developed to consider dislocation penetration [12, 47, 48], misfit dislocations [52, 53] , texture [55, 56], and intermixing at the interface [24].

I.2.1 Dislocation pile-up based hall-petch model

When h > 50 nm, Hall-Petch strengthening mechanism typically dominates in metallic multilayers. Hall-Petch slope is a measure of the strength of the interface boundaries to slip transmission and determines the rate of increase of strength with decreasing h. The slope is typically interpreted in terms of dislocation pile-ups in softer components against interfaces [119, 131, 145, 146]. Straight edge dislocations piled up against an interface, and the leading dislocation is resisted by the interface with a barrier stress of τ^*. During glide on the slip plane, resolved shear stress τ_0 is reached on the plane, which includes the lattice resistance (Peierls-Nabarro stress), solid solution effects and precipitation hardening. The number of dislocations at one end of the pile-up is approximated by [147]

$$N = \frac{\pi L (1 - \nu)(\tau - \tau_0)}{\mu b} \tag{1.1}$$

where b is the Burger's vector of a single dislocation, ν is the Poisson ratio, μ is the shear modulus, τ_0 is the lattice friction stress and L is the distance between source and obstacle. At the point when a leading dislocation is just able to cross the interface, the following relation satisfies

$$\tau = \tau_0 + \left(\frac{G' b \tau^*}{\pi h'}\right)^{\frac{1}{2}} \tag{1.2}$$

where τ^* is the critical resolved shear stress to push the leading dislocation across the interface.

By simplifying equation (2) for indentation hardness, we have

$$H = H_0 + kh^{-1/2} \tag{1.3}$$

where H is hardness of multilayers, H_0 is the hardness, h is individual layer thickness corresponding to L, and k represents all other parameters within brackets of equation (1.2).

I.2.2 Confined layer slip (CLS) model

When h is in the range of tens of nm, dislocation pile-ups become less likely. Deformation occurs by glide of single Orowan-type loops bounded by two interfaces [119, 145, 148, 149]. Dislocations are prone to be confined within layers as described by a confined layer slip (CLS) model [123], which was developed later by Misra et al [123]. The energy balance below shows the applied shear stress (τ_{cls}) required to propagate a glide loop of Burgers vector b confined to one layer.

$$\tau_{cls} b h' = 2W_D \tag{1.4}$$

where h' is the layer thickness measured parallel to the glide pane, W_D is the self-energy of the dislocation segment deposited at the interface.

The modified CLS model considers arrays of misfit dislocations at interface, as well as interface stress. For a 60^{o} dislocation the modified CLS model describes the shear stress to propagate a dislocation across layer interface, τ_{cls}, as follows [123]:

$$W_D = \frac{\mu b^2}{16\pi}\left(\frac{4-\nu}{1-\nu}\right)\left[\ln\frac{\alpha h'}{b}\right] \tag{1.5}$$

where α determines the dislocation core cut-off radius, and *h'* is the layer thickness along the glide plane.

Substituting (1.5) in (1.4), we obtain

$$\tau_{CLS} = \frac{\mu b}{8\pi h'}\left(\frac{4-\nu}{1-\nu}\right)\left(\ln\frac{h'}{b}\right) \tag{1.6}$$

Cu/Nb multilayer showed that the model does not fit the experimental data very well shown in Figure 17. Overall the model predicts strengthening at a much faster rate with decreasing h than that observed experimentally resulting in under prediction of strength at large h and over prediction at low h [132].

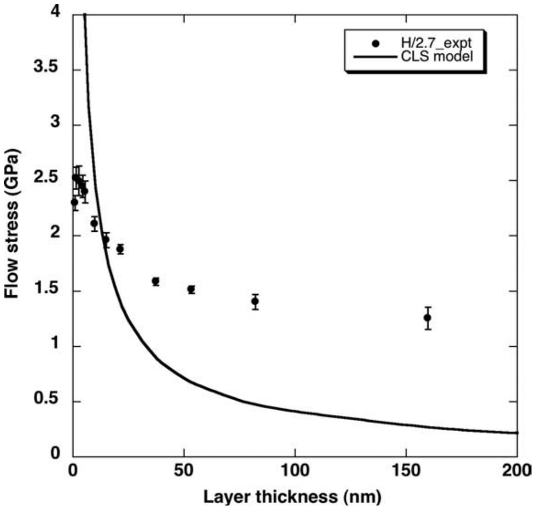

Figure 17. Results of the confined layer slip model compared to the experimental data. Note that the model significantly overestimates (underestimates) the strength at low (high) layer thickness.

After further refinement by taking interface stress and dislocation interactions, we obtain

$$\tau_{cls} = \frac{\mu b}{8\pi h^{'}}\left(\frac{4-\nu}{1-\nu}\right)\ln\left(\frac{\alpha h^{'}}{b}\right) - \frac{f}{h} + \frac{C}{\lambda} \tag{1.7}$$

f is the interface stress, λ is the average spacing between misfit dislocations at interface, and C is approximately μb/(1-ν). A good fit to the plot of hardness vs. layer thickness has been obtained for Cu/Nb multilayers. The comparison of refined CLS model and experiments (Figure 18) verifies that the modified model fits experimental results very well.

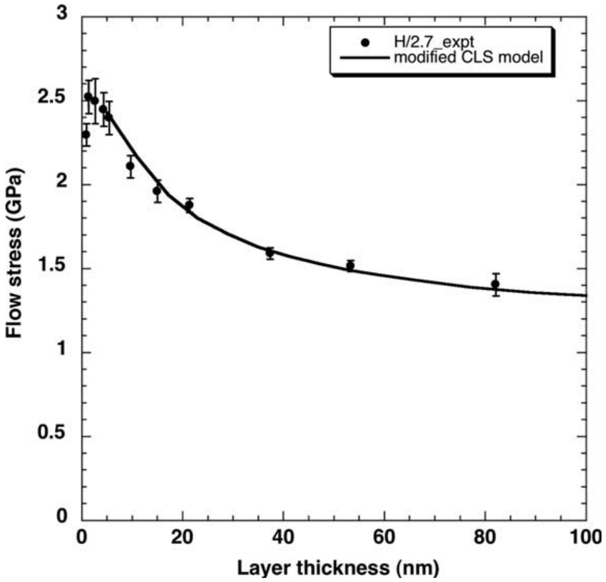

Figure 18. Results of the modified confined layer slip model compared to the experimental data

I.2.3 Dislocation crossing interface model

When h ≤ 5 nm, experimental observation indicates that the strength of metallic multilayers reaches a maximum value and there is no significant increase when h decreases to 1 nm. In this range, interface cutting across interfaces at characteristic interface barrier strength is the operative mechanism. Strength originates from the barrier resistance of interface to dislocation penetration. The glide stress, increasing as h decreases, will exceed the interface barrier strength (τ*) to the transmission of a single glide dislocation when h is very small. The exact layer thickness at which the transition from confined layer slip to interface crossing occurs depends on the magnitude of τ*.

Besides H-P model, some other factors could explain the high strengths of multilayers such as Koehler model [137] and coherency stresses [138, 150]. Koehler stress, τ_K, arises from the elastic modulus mismatch between the two components. For multilayers with large shear modulus mismatch between layers, a dislocation in the lower modulus (hence, lower line energy) phase may need to overcome a significant repulsive image stress from the higher modulus phase before slip can be transmitted across layers [131]. As dislocations approach the harder layer from the softer layer, the image force repels the dislocation with a stress [137]

$$\tau_K^* = \frac{\mu_1(\mu_2 - \mu_1)b}{4\pi(\mu_2 + \mu_1)h} \tag{1.8}$$

where μ is shear modulus. Koehler stress can be the main contributing factor to strengthening for multilayers with different moduli (48 vs. 76 GPa for Cu and Ni in Cu/Ni multilayer), result in a large τ_K.

Multilayers, with very small individual layer thickness for fully coherent interface, coherency stress makes contributions in the Cu/Ni system. The coherent multilayers have large in-plane coherency stresses that alternate from tensile to compressive between layers, giving rise to a periodic resistance to dislocation motion across layers. Above the critical thickness for coherency loss, interfaces are semi-coherent and have dislocation arrays to accommodate the misfit between layers. The stress field of the misfit dislocation array then poses a barrier to dislocations crossing the interface [131].

Design of composite materials with variable mechanical strength has significant practical applications, and is a non-trivial task. Besides the aforementioned strengthening mechanisms, numerous other factors can vary the mechanical strength of composites, such as lattice parameters, elastic constants, misfit dislocation spacing, slip discontinuity across the interface, and mismatch in stacking fault energies.

I.3 Surface morphology of thin film

Thin films are formed from a flux that approaches the substrate from a limited set of directions. The morphology of grains tends to be columnar. The production of thin films usually proceeds through nucleation and growth stages. Such stages involve adsorption, surface diffusion, chemical binding and other atomic processes at surfaces indicated schematically in Figure 19. After the atoms are transported from the target to the substrate (adatom), adatoms are adsorbed onto the surface of the substrate, diffused over the surface, and finally incorporated into the coating or removed from the surface by re-evaporation. Some adatoms may be re-evaporated if they have enough energy to break the bonds formed on the surface. The next step involves movement of the coating atoms to their final position within the coating by processes such as bulk diffusion. In sputter deposition, the transport step is controlled by apparatus geometry and working gas pressure, while the diffusion steps are controlled by the substrate temperature, or may be significantly influenced by energetic particle bombardment. The microstructure of thin film, deposited by physical vapor deposition, can be categorized by polycrystalline, amorphous, and epitaxial films [151].

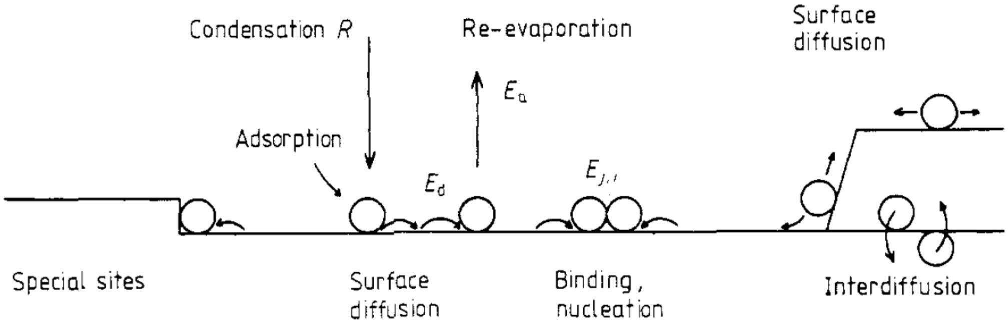

Figure 19. Schematic diagram of processes and characteristic energies in nucleation and growth on surfaces [152].

I.3.1 Polycrystalline films

Table 1 summarizes the kinetic factors and process parameters that affect the evolution of the structure of polycrystalline films. The grain size at impingement is controlled by the relative rates of island nucleation and growth, shown in Figure 20. The nucleation rate depends on the substrate temperature and the deposition rate. The rate of island growth also depends on the deposition rate, rate of adatom diffusion and adatom desorption rate. The grain size at impingement increases as the temperature increases, and is unaffected or decreases with increasing deposition rate [153].

Coarsening processes are faster at higher temperatures. Grain growth can occur during or after film coalescence, during film thickening (type 2 thickening in Figure 20). The rates of grain growth and other coarsening processes are generally reduced by the presence of impurities from either solute of precipitate drag. Precipitates can suppress normal grain growth and lead to abnormal grain growth in which the final grain size of a film can be many times larger than the film thickness. When bulk grain boundaries are immobile, both the grain size at impingement and the corresponding grain size distribution are preserved at the base of a film, and in the absence of impurity effects, films thicken through epitaxial growth on the as-impinged grains at the base of the film. This type 1 thickening mode results in films with columnar grain structures for which the grain size through the thickness of the film is larger than the grain size in the plane of the film [153].

Table 1. Factors affecting structure evolution in polycrystalline films.

Kinetic factors affecting structure evolution	Adatom diffusivities on the substrate surface Adatom self-diffusivities on island surfaces Self-diffusivities in grain boundaries Grain boundary mobilities Adatom cluster nucleation rates Adatom desorption rates
Process parameters	Deposition rate (affects adatom arrival rate, affects adatom diffusion time before cluster nucleation or desorption, affects film purity) Substrate temperature (affects all kinetic processes, increasing rates with increasing temperature Background pressure (affects film and surface purity) In sputter deposition: sputtering gas pressure and substrate bias (affect the angular distribution and energies of arriving adatoms)
Factors affecting zone models	Materials class Impurities incorporation Deposition technique

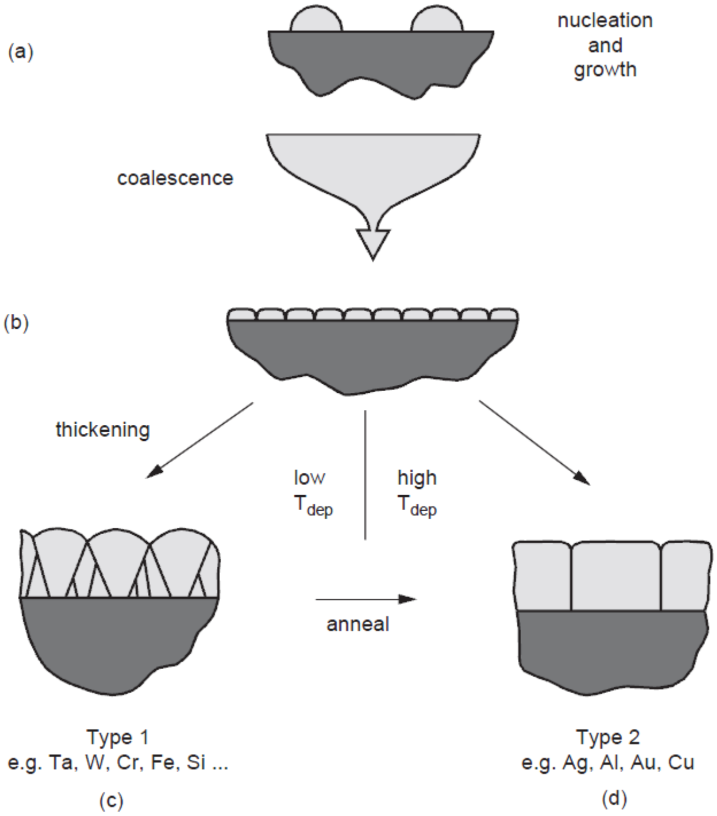

Figure 20. Overview of grain structure evolution during deposition of polycrystalline thin films.

I.3.2 Epitaxial film

Epitaxy refers a thin film on the substrate showing extended single-crystal film formation on top of a crystalline substrate with certain crystallographic orientation relationship. Over the past several decades epitaxial thin films have attracted the attention due to their superior properties over polycrystalline thin films. Epitaxial growth of thin films and the control of defects in thin film hetero structures are key considerations for the next-generation of microelectronic, optical and magnetic devices.

Defect-free epitaxial films exhibiting layer growth are essential. In, depending on the extent of the mismatch, heteroepitaxial thin films can be categorized by three epitaxial regimes (Figure 21).

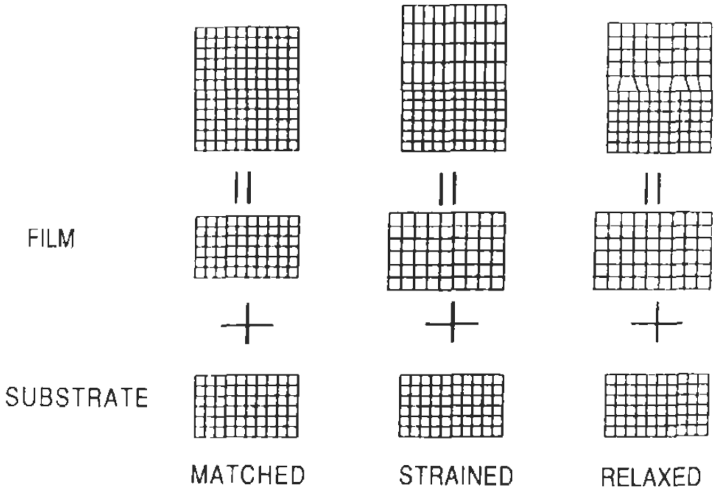

Figure 21. Schematic illustration of lattice-matched, strained, and relaxed heteroepitaxial structures. Homoepitaxy is structurally very similar to lattice-matched heteroepitaxy [154].

If the lattice mismatch is very small, the heterojunction interfacial structure is similar to homoepitaxy. When the film and substrate lattice parameters differ more substantially, either the two lattices strain to accommodate their crystallographic differences or, dislocations form at the interface (relaxed epitaxy). If near the interface the first few film layers strain to match the substrate crystallography (strained-layer), it is called pseudomorphic and it gives coherent epilayers [154].

The lattice matching epitaxy during thin film growth is possible as long as the lattice misfit between the film and the substrate is less than a few percent. Smaller lattice misfit leads to smaller interfacial energy and coherent epitaxy is formed. Films having a large misfit relative to the substrate (>7% -8%) grow epitaxially in the form of single crystals by domain matching epitaxy, where integral multiples of lattice constants match across film–substrate interfaces [155].

I.3.3 Pillar shaped film

Physical vapor deposition with obliquely incident flux and limited adatom diffusion results in a film with a columnar microstructure. These columns will be oriented toward the vapor source and substrate rotation can change the pillar shapes into various morphologies. This is the basis for glancing angle deposition (GLAD), a technique for fabricating porous thin films with engineered structures.

Figure 22 shows the PVD deposition onto the substrate oriented at glancing angles to prepare porous columnar rods films [156]. The wavy shaped film in Figure 23 is the result of the rotation of the substrate relative to the vapor source [157]. An additional adjustment of substrate rotation and tilt will give a variety of flexibility of columnar shapes geometry.

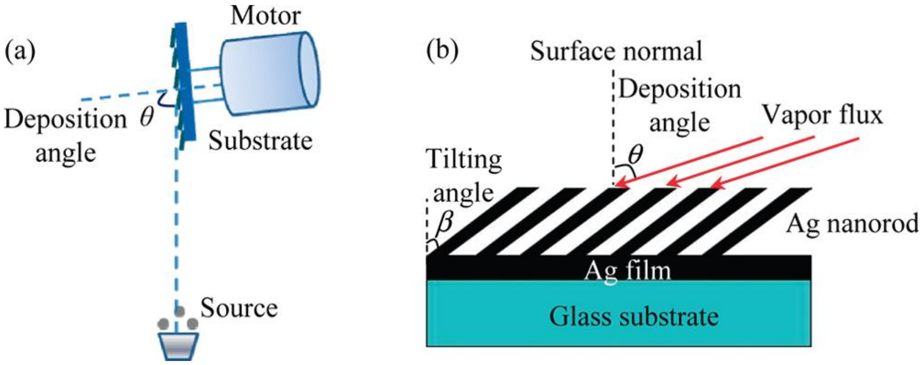

Figure 22. (a) Schematic diagram of the Ag nanorod array fabricated by oblique angle deposition. (b) The definition of deposition angle *θ* and Ag nanorod tilting angle β [156].

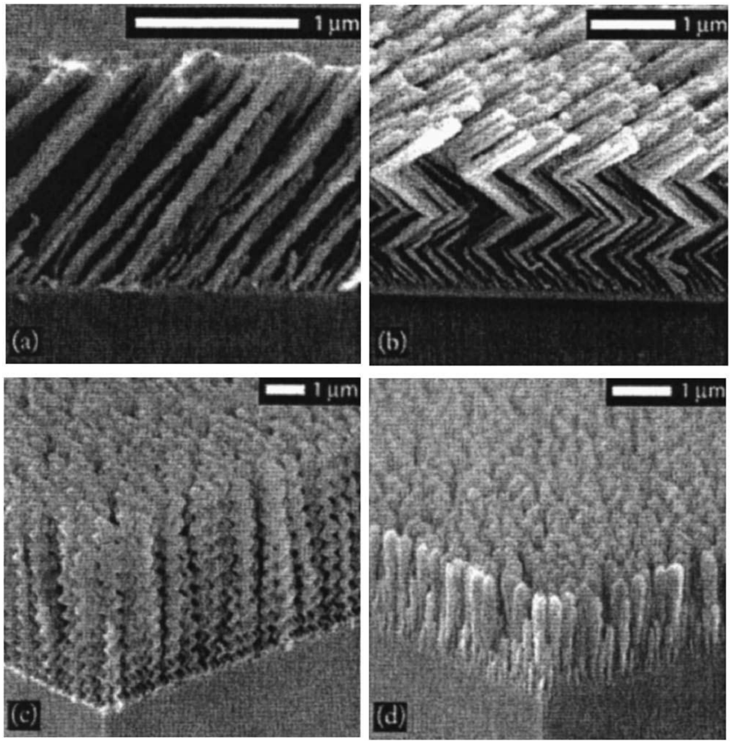

Figure 23 Archetypal GLAD fabricated microstructures, (a) tilted columns, (b) chevronic or zig-zag columns, (c) helical columns, and (d) vertical columns. The particular microstructure is determined by the substrate movement during deposition, with substrate rotation being used to “shadow sculpt” the columns [157].

Due to the porous nature of the films and the increased surface area, a variety of chemical applications and sensor device architectures are possible [154]. Optical properties of these films appear to have received the greatest attention. Silver nanorod arrays with different lengths fabricated by oblique angle deposition at various vapor deposition angles have been studied systematically on their morphologies, optical reflections, and surface-enhanced Raman scattering responses [156]. Indium sulfide nanorod arrays and thin films of various thicknesses were fabricated by using GLAD thermal evaporation. Indium sulfide nanorod layers have significantly lower reflectance and superior optical absorption values compared to conventional flat indium sulfide thin films [158]. However, porosity in optical films shows moisture permeation which is deleterious to their reliability. The dense capping layers by normal deposition would prevent this problem.

CHAPTER II

EXPERIMENTAL DETAILS

II.1 Sputtering

All thin films used in this thesis were deposited by custom-made magnetron sputtering technique shown in Figure 24. Atoms are ejected from targets at room temperature by bombarding their surfaces with energetic ions. The emitted atoms traverse a reduced pressure ambient and deposit atomistically on the substrate to form a film. Detailed information about sputter deposition procedures can be found easily from elsewhere such as [1]. The base pressure of the sputter chamber was less than $5*10^{-8}$ Torr prior to deposition and four sputter guns are installed. UHP Ar gas with a purity of 99.999% was used during the deposition at the pressure of $1.5*10^{-3}$ Torr. Prior to deposition, all targets were pre-sputtered to clean the surface of target itself from contamination. The temperature rise due to atom bombardment was usually less than 50 °C. Multilayers were deposited by alternatively activating two guns, which was controlled by gun shutters. Mg/Nb multilayer films with identical h of 2.5 - 200nm were deposited onto Si (100) substrates with native oxides at room temperature and the targets were purchased from AJA international, Inc. All the targets have 99.95% purity and were 3” in diameter with 1/4” in thickness. For the hydrogen storage study, a Pd cap layer was deposited onto the top of the as-prepared film so that it can protect the film surface from the oxidation and water contamination. Pd cap layer also plays as a catalyst for hydrogen absorption and dissociation for hydrogen loading into the Mg single layer and Mg/Nb multilayer films.

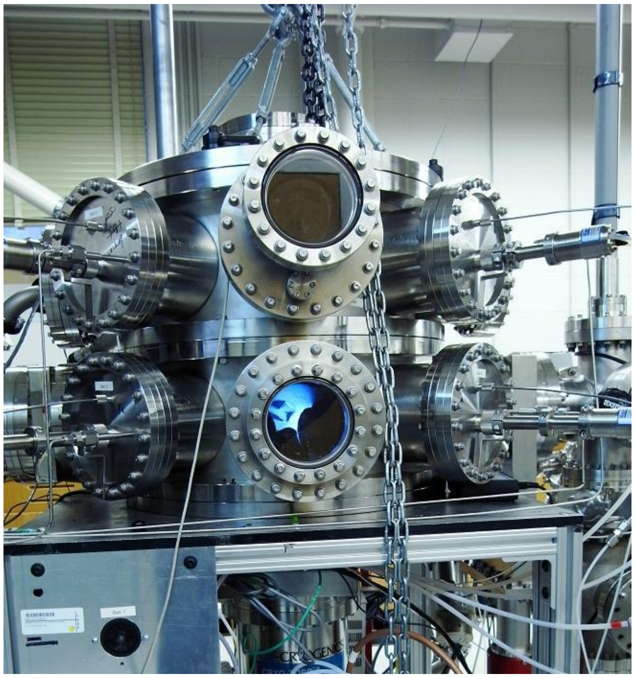

Figure 24. Image of the four-gun magnetron sputtering system used for thin film fabrication.

II.2 Hydrogen storage

A custom-made high vacuum annealing chamber can perform the hydrogen loading and unloading studies. The base pressure of chamber was ~ 5×10^{-7} Torr before hydrogen loading. Samples can be hydrided at a hydrogen pressure of 0.25 MPa up to 300 °C for certain time. Hydrogen desorption can be performed by thermal desorption spectroscopy (TDS) method enabled by a quadruple mass spectrometer in a residual gas analyzer (RGA). The temperature can increase to ~ 400°C at a constant heating rate.

Pressure composition isotherm (PCI) curve measurements were measured by using Micrometics ASAP 2020 surface area and pore size analyzer. The weight of Mg/Nb multilayers was around 50 mg for each measurement. Before the measurement, the sample was dried again by using the “outgas” function of the surface area analyzer for 10 h at 80 °C. The starting hydrogen pressure was 0.01 mbar and increased slowly up to 1 bar.

II.3 Microstructural characterization

II.3.1 X-ray diffraction (XRD)

The microstructure investigation of as-deposited and hydride thin films were determined with XRD. XRD is a powerful and non-destructive tool to analyze the microstructure of thin films. This method does not require any sample preparation and the microstructure can be quickly scanned for further material characterization experiments, such as TEM, SEM, and synchrotron XRD. XRD experiments in this thesis were performed using by a Bruker-AXS D8 advanced Bragg-Brentano X-ray powder diffractometer equipped with Cu-Kα source anode, D8 Goniometer, automatic divergence slit, graphite monochromator on the diffracted beam and Lynxeye PSD for detection. The films are exposed to a monochromatic beam of X-rays from a Cu-K_α source, with a wavelength of 1.5406 Å.

Thin films have the periodic arrays of atoms on specific crystallographic planes, and atoms scatter X-rays and, the scattered x-rays mutually reinforce each other in certain directions. The position (angle θ) of the diffracted beam is given by the Bragg’s law

$$2d \sin \theta = n\lambda \tag{2.1}$$

where λ is the wavelength for the incident x-ray beam which varies by the source, d is the spacing between crystallographic planes, and θ is the angle between incident beam and the crystallographic plane. XRD patterns about the specimen are used to identify crystalline phases and orientation and it also provides lattice parameters, lattice distortion (strain), grain size, epitaxy, phase composition, and preferred orientation etc.

II.3.2 Scanning electron microscopy (SEM)

The morphological changes of as-deposited, hydrogen absorbed and desorbed film were examined by JEOL-7500 SEM equipped with a field emission gun. The cross section specimens of Mg single layer films were prepared by cleaving them right before sample loading for fresh surface observation. SEM samples for Mg single layer films do not need any preparation, however, the cross section samples for Mg/Nb multilayer needs polishing to see the clear interfaces. Since Mg samples are sensitive to the water and hydride samples are vulnerable to heat, an isopropanol was used as a polishing liquid with little usage of the heat. Detailed sample preparation is described in next section below.

II.3.3 Transmission electron microscopy (TEM)

Conventional TEM analysis is performed using the JEOL-2010 microscope, equipped with a Gatan SC1000 ORIUS CCD camera (Model 832), operating at 200 kV accelerating voltage with a LaB_6 filament. The microscope has a maximum 0.23 nm point-to-point resolution. The FEI Tecnai G2 F20 microscope is equipped with a

Fischione ultra-high resolution STEM HAADF detector (0.23 nm in the STEM image mode) and Oxford instruments EDX detector with a spatial resolution of ~ 1- 2 nm.

Since all of the thin films were deposited on single crystal Si substrate, kikuchi pattern was used to align the specimen vertical to the electron beam. Then the microstructure and orientation relationship (OR) between Mg/Nb layers were checked. Conventionally available images by TEM operation, such as high resolution image (HRTEM), diffraction pattern, dark field, STEM (line scan for composition analysis) and EDS mapping, were acquired.

A metastable bcc Mg structure in the interface between Mg and Nb multilayers were observed by HRTEM images analysis. A bcc Mg phase was also confirmed by Fast Fourier Transform (FFT) images by using digital micrograph program. A new orthorhombic Mg hydride structure (Mg hydride has a tetragonal structure in bulk size) was revealed by diffraction pattern (DP) analysis. When these new DPs were observed, EDAM (a program for indexing electron diffraction patterns) was used to generate DPs with acquired d-spacings.

II.3.4 Specimen preparation for TEM and SEM

TEM specimens were prepared with conventional methods including mechanical grinding, polishing, dimple grinding and polishing (Gatan 656) and ion mill polishing (Gatan 691 PIPS). Since all the samples are sensitive to the water, an isopropanol was used as a polishing solution for all grinding and polishing process. In addition, samples are vulnerable to heat, so the heat usage was minimized. If there is a possibility of phase transformation during the TEM sample prep (for example Mg composite hydride dissociates hydrogen during the polishing in my case), then the specimens were observed by TEM directly right after processing.

II.4 Nanoindectation

II.4.1 Definition of indentation hardness

Hardness is one of the important mechanical properties of a material and indicates its resistance to localized plastic deformation or to permanent penetration by another hard material. Nanoindentation testing allows us to probe mechanical properties of film specimens with typically 1um dimensions. Nanoindentation is a commercially available, load-controlled submicron indentation instrument. The Berkovich diamond indenter, a three-sided pyramidal with triangular base, is most frequently employed.

Hardness measurement involves the measurement of load (F) and displacement (h) and a loading and unloading curve is typically obtained. The displacement is composed of elastic and plastic deformation. As the indenter is retracted, the deformed area A_c (plastic deformation) can be measured. The hardness of materials measured by nanoindentation is referred as indentation hardness (H_{IT}) and it is determined by equation

$$H_{IT} = F_{\max} / A_c \qquad (2.2)$$

where $F_{\max}$ is the maximum applied force and A_c is the projected (cross-sectional) area of the contact between the indenter and the test piece determined from the load-displacement curve, as shown in Figure 25. A_c cannot be measured directly but is a function of the indentation depth h_c.

$$H_c = h_{\max} - \exp(h_{\max} - h_i) \quad (2.3)$$

where $h_{\max}$ is the maximum depth and h_i is the intercept of the tangent to the load-displacement data at the maximum load on unloading with the depth axis. The correction factor ε, a function of the shape of the indenter tip, for flat punch is 1, conical punch is 0.73, Berkovich and Vickers indenter is 0.75, and for paraboloid of revolution (includes spherical) is also 0.75.

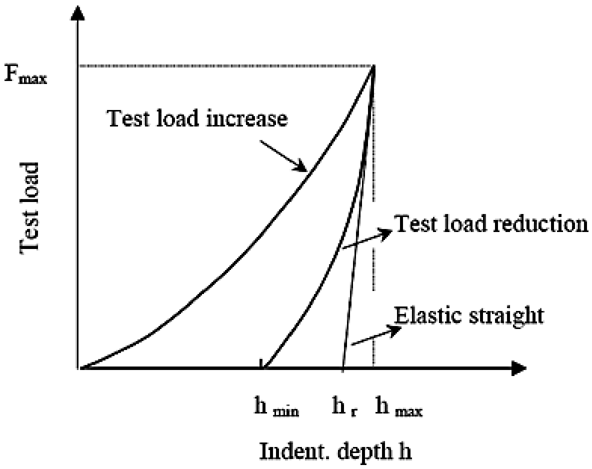

Figure 25. Schematic diagram of a loading-unloading curve during indentation

II.4.2 Measurement of thin film hardness

Indentation hardness tests for Mg/Nb multilayers were performed by using Fischerscope HM2000XYp micro/nanoindenter with a Vickers indenter tip. The hardness is determined from the area of the indenter displacement under load. The indentation depth and a constant, specific to each indenter, are used to calculate the area of the indenter displacement. The positioning devices consist of the holding device for the measuring head, and a microscope with an attached video camera. Manually adjustable XY measuring stage and programmable XY measuring stage are equipped in the tester. The coordinates of the measurement points can be stored and visited automatically in sequence. The indentation hardness and modulus of the Mg/Nb films were measured based on an average of 9 indents at different indentation depths at room temperature. The loading rate was kept at 10 mN/s and indentation depth was chosen to allow the diamond tip penetrate into at least two bilayers, ranging from 100 nm at small layer thickness to 600 nm at large h (the total thickness of these films were ~ 4 μm), whereas the maximum indentation depth is still limited to 10 – 15% of total film thickness to avoid substrate effect.

II.5 Profilometer

The tensile or compressive stress of the thin films deposited on the substrate can be measured by Dektak 150 profilometer. The curvature of a stress bar (substrate) is measured by scanning the longitudinal direction of a stress bar with rectangular shape. When a pre-stress (pre-deposition) scan data is obtained, the stress in the thin film after deposition can be calculated. Several measurements (5-10) are taken, and average values arecalculated. Then, using the Stoney equation residual stresses in the deposited films can be calculated as:

$$\sigma = \frac{1}{6}\left(\frac{1}{1/R_1 - 1/R_2}\right)\frac{E t_s^{\ 2}}{(1-\nu)t_f} \qquad (2.4)$$

where E, v, t_s , and t_f are Young’s modulus, Poisson’s ratio, substrate thickness and film thickness respectively. R_1 and R_2 are substrate radius of curvatures before and after depositions respectively. The results could be positive or negative depending on the state of the stress. A positive value implies tensile and a negative value implies compressive residual stress. A first assumption of the Stoney equation is that the substrate is thick compared to the thickness of the film, but still thin enough that it bends due to the stress in the film. A second assumption is that the film is in a state of plane stress, meaning that in the plane of the film the stress is independent of direction.

CHAPTER III

HIGH STRENGTH MG/NB NANOLAYER COMPOSITES[*]

III.1 Overview

We report on the microstructure and mechanical properties of sputter-deposited Mg/Nb multilayer films, with individual layer thickness, h, of 2.5 to 200 nm. High resolution TEM studies reveal the formation of metastable Mg with body-centered cubic structure along interface in multilayers with h of 5 nm or less. As h decreases, the hardnesses of multilayers increase and approach a maximum of ~ 2.7 GPa at a few nm layer thickness. Size dependent strengthening in Mg/Nb multilayers is compared to that in Mg with various grain sizes, and Cu/Nb and Al/Nb multilayers and strengthening mechanisms in Mg/Nb multilayers are discussed.

---

[*] This chapter reprinted with permission from “High strength Mg/Nb nanolayer composites” by B. Ham and X. Zhang, Materials Science and Engineering A, 528 (2011) 2028–2033, Copyright 2011 by Elsevier.

III.2 Introduction

Mechanical properties of magnesium and its alloys have been extensively studied as these materials could have important applications for automobile and aerospace industries, where high strength and light weight materials are desirable. The inherent strength of Mg, however, is very low. The yield strength of bulk Mg is ~ 65 MPa [159], while grain refinement down to 125 μm via equal channel angular pressing (ECAP) is able to increase the yield strength to ~ 225 MPa [159]. Inefficient grain refinement via ECAP has lead to the development of other techniques. A recent study shows that the average grain size in AZ91D Mg alloys can be reduced to ~ 40 nm via high strain rate severe plastic deformation, and the hardness of alloy increases to ~ 1.8 GPa [160]. Another approach that leads to noticeable strength increase in Mg composite is to construct multilayers, such as Mg/Al, using repetitive roll bonding [161]. But such a technique could not reduce the layer thickness of composites to nanoregime, and hence the increase in strength of Mg alloys is moderate.

Multilayered metallic materials with hundreds to a few nm layer thicknesses, prepared by sputtering or evaporation, have been studied extensively since they exhibit much greater strength comparing to their bulk counterparts [122-126]. Various mechanisms were proposed to explain the size (layer thickness) dependent enhancement of hardness of multilayers. When individual layer thickness, h, is larger than a few tens of nanometers, indentation hardness increases linearly with $1/\sqrt{h}$, and strengthening can be interpreted by the Hall-Petch model [136] where dislocations pile up against layer interfaces. When h decreases further from a few tens to several nm, hardness vs. $1/\sqrt{h}$

plot becomes non-linear. Strengthening in this regime may be explained by the confined layer slip (CLS) mechanism based on the Orowan model that considers the bowing of single dislocations within layers. CLS mechanism leads to a $hardness \propto \ln h / h$ relation [126, 131, 149, 162]. In several cases, the CLS model does not compare well to the experimental results [148], and modifications to the model have been developed for immiscible Cu/Nb multilayers to account for such a large discrepancy [123]. When h decreases to a few nm, a hardness plateau or peak hardness is typically reached. Numerous strengthening mechanisms have been considered at this length scale. When the layer constituent has a large shear modulus mismatch, Koehler stress due to the image force of dislocations plays an important role in determining the peak strength [137-139]. On the other hand, if a large lattice mismatch exists, coherency stress arises and it can change the dislocation core structure and elastic constants, and hence increases the interface barrier strength in Cu/Ni multilayers [138]. Also coherency stresses can act as retarding force against the glide of dislocations in the layers. In Cu/Nb multilayers, a dislocation spreads its core at the interface (since interface is weak in shear), making it difficult to be reemitted into the opposite layers, and hence the interface is a strong barrier to the transmission of dislocations [123, 140]. Meanwhile at such a small length scale, certain constituents of the layer could form metastable phases, such as body-centered cubic (bcc) structure of Co in Co/Cr [141], or face-centered cubic (fcc) structure of Ti in Ti/Al [141] and Ti/Ni [142], and bcc Cu in Cu/Mo [143] and Cu/Nb nanolayers [144].

In this paper, we report the microstructure and mechanical strength of a series of Mg/Nb multilayers. High strength is achieved in these multilayers with a few nm layer thickness. The size dependent strengthening mechanism in Mg/Nb multilayers is also compared to that of bulk Mg, and sputtered Cu/Nb and Al/Nb multilayers.

III.3 Experimental

Mg/Nb multilayer films with identical h of 2.5 - 200 nm were deposited by DC magnetron sputtering onto Si (100) substrates with native oxides at room temperature. The base pressure of the sputter chamber was less than 5 $\times 10^{-8}$ torr before deposition. The total film thickness was kept at ~1.5 μm for multilayers with h of 50 nm or less, and ~ 5 μm for multilayers with h of 100 nm or greater. The deposition rate for Mg and Nb were ~ 2 and ~ 0.5 nm/s respectively, under ~ 2.5 mtorr argon pressure. X-ray diffraction (XRD) experiment was performed on a Bruker-AXS D8-focus Bragg-Brentano x-ray diffractometer. Field emission scanning electron microscopy (FESEM) experiment were performed on a FE-SEM 7500 microscope operated at 5 kV. Transmission electron microscopy (TEM) and high resolution TEM (HRTEM) were performed using a JEOL 2010 microscope operated at 200kV, and JEOL 3000F at 300kV respectively. The hardness and indentation modulus of multilayers were measured by Fischerscope HM2000XYp, with Vickers indenter, at room temperature. The nanoindentation analysis method follows that proposed by Oliver and Pharr [163]. The indentation depth varies from from 100 nm to 15% of the total film thickness so that substrate effect doesn’t affect the hardness values, and at least several bilayers are probed by nanoindentor. A minimum of nine indentations were performed at each indentation depth on each sample to get an average hardness value and standard deviation. A plateau is typically observed in the hardness vs. indentation depth plot, as shown in Figure 31a.

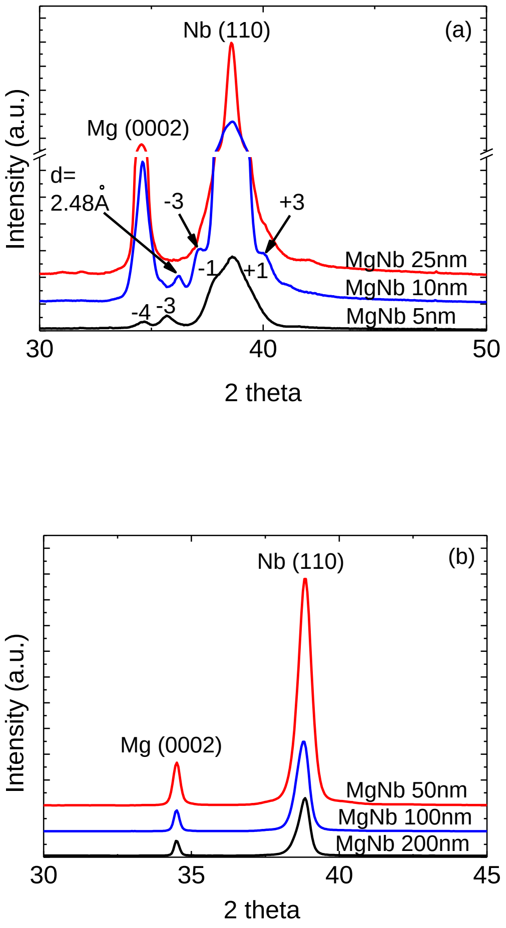

Figure 26. XRD patterns of Mg/Nb multilayer films with individual layer thickness, h, varying from 2.5 to 200 nm. (a) XRD patterns of multilayers with h = 25 – 5 nm shows Several satellite peaks due to the formation of superlattice. (b) When h decreases from 200 to 50 nm, the peak intensity of Mg (0002) and Nb (110) become stronger.

III.4 Results

Figure 26 shows XRD patterns of Mg/Nb multilayers. High intensity Mg (0002) and Nb (110) peaks are observed in Mg 20 nm / Nb 20 nm (referred to as Mg/Nb 20 nm thereafter) and Mg/Nb 10nm specimens, indicating that the multilayers are highly textured along these orientations. Superlattice peaks on each side of Nb (110) diffraction are also observed in Mg/Nb 10 nm multilayers.

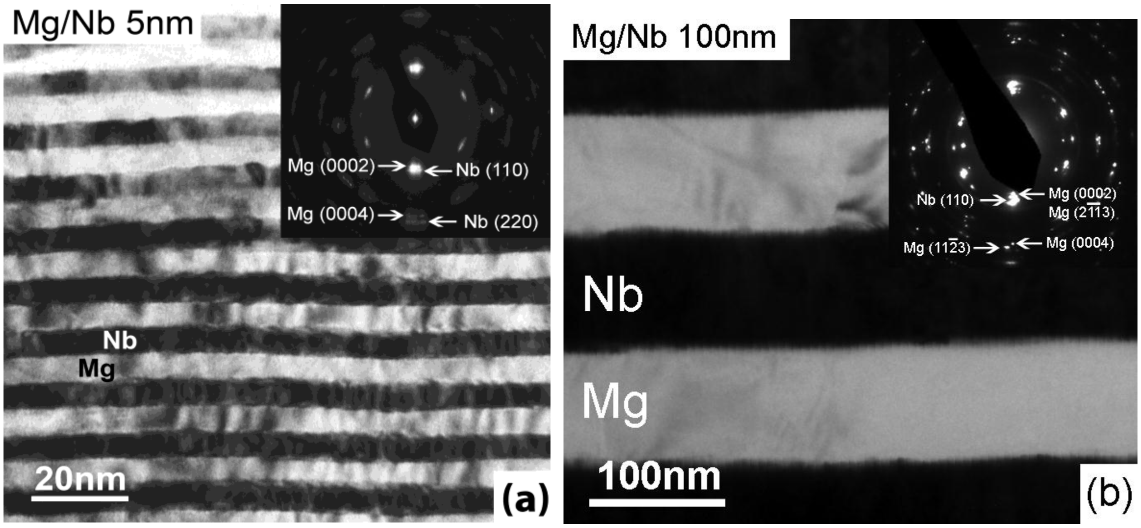

Figure 27. (a) Bright field cross-sectional TEM micrograph and inserted select area diffraction pattern of as-deposited Mg/Nb 5 nm multilayers showing orientation relationship between hcp Mg {0002} and bcc Nb {110}. (b) Cross-sectional TEM image and diffraction pattern of as-deposited Mg/Nb 100nm multilayer films showing discrete layer interface. (c) Cross-sectional FESEM micrograph of Mg/Nb 100 nm multilayers taken in backscattering mode confirms chemically sharp interface in the same specimen.

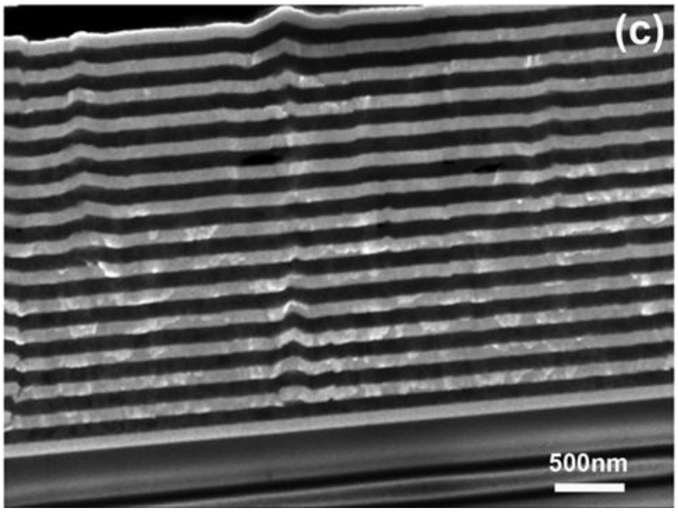

Figure 27. Continued.

Figure 27a is the bright field cross-sectional TEM image of Mg/Nb 5 nm multilayers. It reveals the discrete layer interface between Mg and Nb. The inserted selected area diffraction (SAD) pattern in Figure 27a also shows strong Mg (0002) and Nb (110) fiber textures. Cross-sectional TEM micrograph of Mg/Nb 100 nm multilayer, Figure 27b, shows weaker texture of the same orientations and clear interface. Chemically sharp interfaces are also observed in the same specimen as shown in a cross-sectional FESEM micrograph captured in the back scattering mode in Figure 27c.

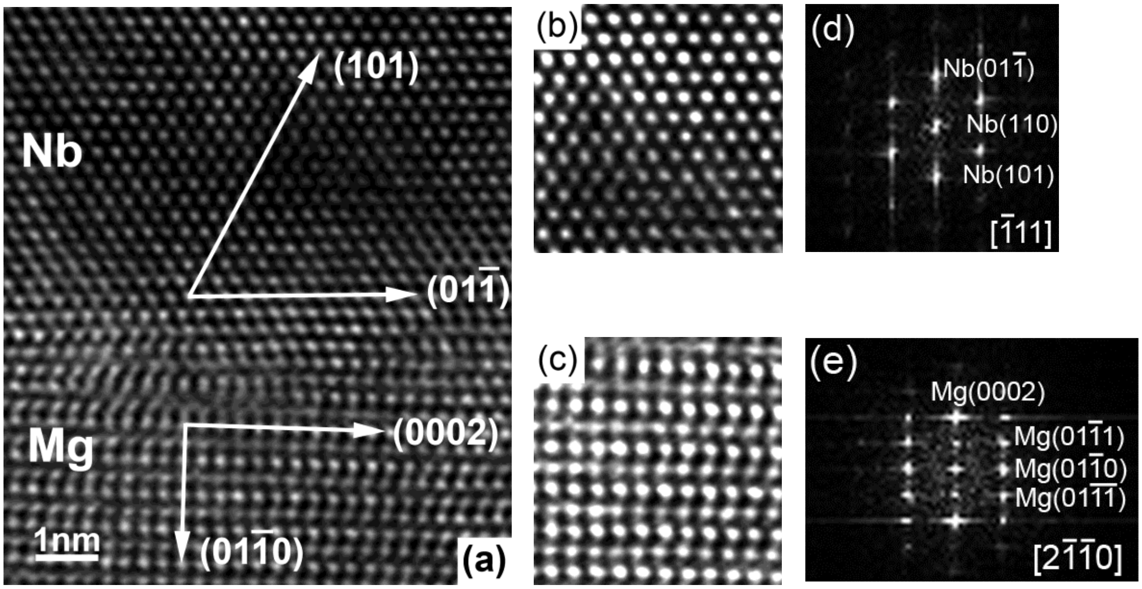

Figure 28. (a) Cross-sectional HRTEM micrograph of Mg/Nb 5 nm multilayers shows clear crystal structures of hcp Mg and bcc Nb without significant intermixing. (b) and (c) show magnified images of bcc Nb and hcp Mg, respectively. (d) and (e) shows the corresponding fast Fourier transform (FFT) of the respective micrographs. The diffraction zone axis of Nb is $[\bar{1}11]$ as shown in (d); whereas it is $[2\bar{1}\bar{1}0]$ for hcp Mg in (e).

HRTEM studies reveal two types of Mg/Nb interfaces in Mg /Nb 5nm multilayers. In the first case, as shown in Figure 28, Mg has a stable hexagonal closely packed (hcp) crystal structure. Figure 28b and c show the magnified HRTEM micrographs of bcc Nb and hcp Mg close to interface. The fast Fourier transforms (FFTs) of the images, Figure 28d and e, confirm the diffraction zone to be Nb $[\bar{1}11]$, and hcp Mg $[2\bar{1}\bar{1}0]$ respectively.

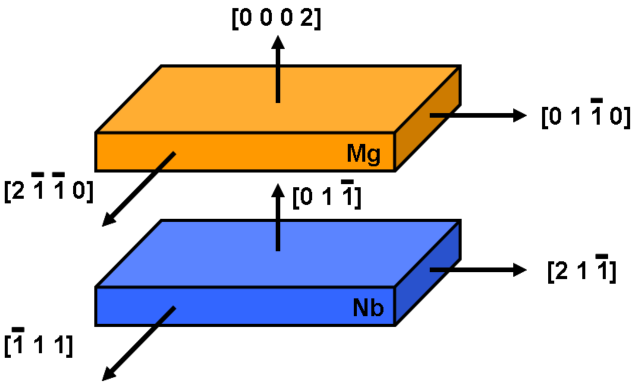

Figure 29. A schematic diagram representing the orientation relationship between Mg and Nb in multilayers: in-plane direction, $[2\bar{1}\bar{1}0]_{Mg}$ // $[\bar{1}11]_{Nb}$ and $[01\bar{1}0]_{Mg}$ // $[21\bar{1}]_{Nb}$; out-of-plane, $\{0001\}_{Mg}//\{110\}_{Nb}$.

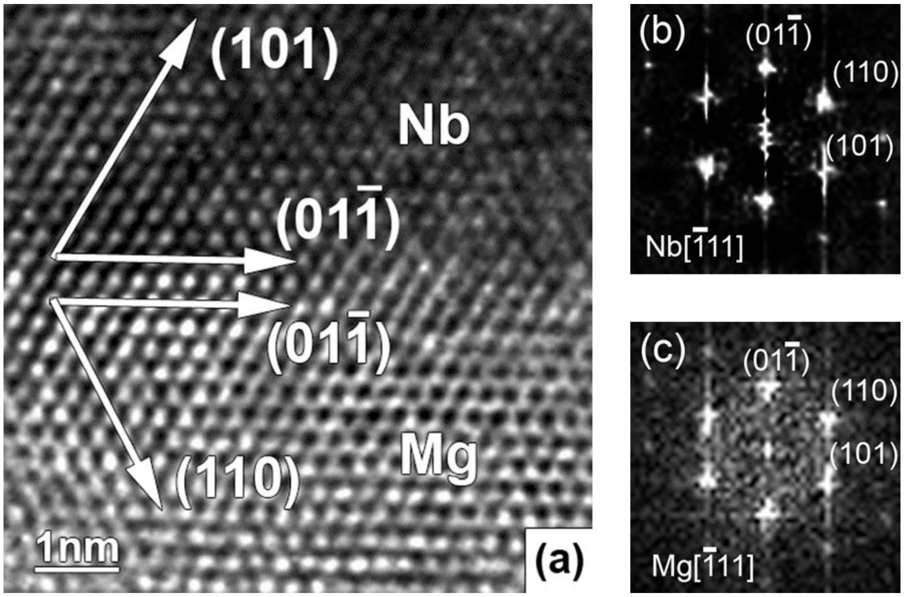

Figure 30. (a) An HRTEM image in a different region of the same Mg/Nb 5 nm multilayer shows the formation of metastable bcc Mg, which is coherent with Nb at interface. (b) and (c) are FFTs of respective Nb and Mg close to interface. Both components show $[\bar{1}11]$ zone axis.

The orientation relationship between hcp Mg and bcc Nb is illustrated schematically in Figure 29 as $[2\bar{1}\bar{1}0]_{Mg}$ // $[\bar{1}11]_{Nb}$ and $\{0001\}_{Mg}//\{110\}_{Nb}$. Although there is no clear sign of intermixing along interface, there appears to be distortions in Mg crystal structures right along interface, and the thickness of distorted zone is ~ 3 - 5 atomic layers. In the second scenarios, as shown in Figure 30a, in a different region of the same Mg/Nb 5 nm multilayer specimen, Mg appears to grow epitaxially on Nb. A bcc crystal structure is identified in Mg. FFTs of Nb and Mg close to interface are shown in Figure 30b and c. Here Nb {110} plane is parallel to the interface.

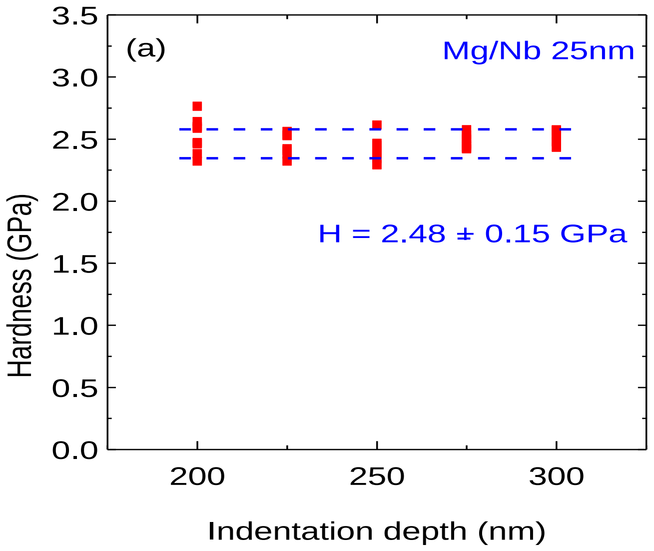

Figure 31. (a) The hardness vs. indentation depth plot of Mg/Nb 25 nm multilayers. The hardness value and error bar of specimens were measured from the plateau region of the plot. (b) Hardness of Mg/Nb, Cu/Nb and Al/Nb multilayer films as a function of $h^{-0.5}$, where h is the thickness of each individual layer The hardness of pure Mg were also plotted for comparison and magnified in the inset as a function of $d^{-0.5}$, where d is the average grain size.

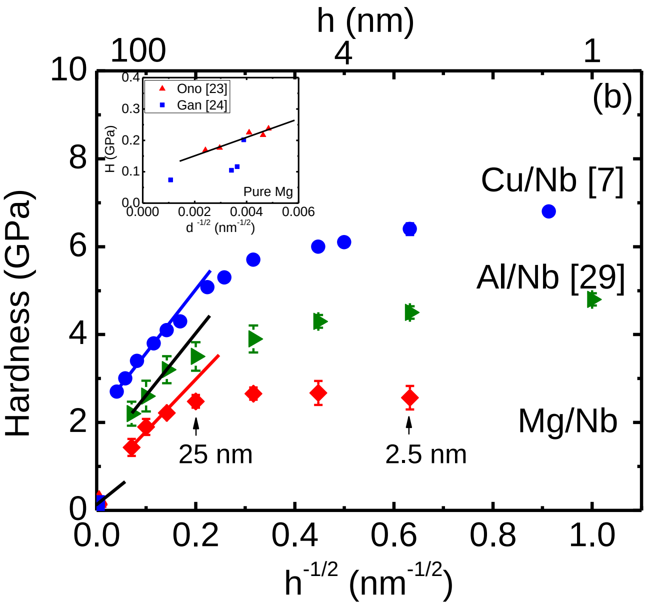

Figure 31 Continued.

Figure 31b shows the hardness of as-deposited (solid diamonds) Mg/Nb, Cu/Nb and Al/Nb multilayers as a function of $h^{-0.5}$. The hardness of Mg as a function of $d^{-0.5}$ is also shown, where d is the average grain size. Given the hardness of Mg is too low, a magnified hardness plot of Mg is shown as an insert in Figure 31b. When layer thickness is greater than ~ 50 nm, the hardnesses of all multilayers increase approximately linearly versus $h^{-0.5}$ with decreasing layer thickness. The Hall-Petch slope is the highest, ~ 18.1 $GPa \cdot \sqrt{nm}$ for Cu/Nb multilayer, followed by Al/Nb, ~ 14.1 $GPa \cdot \sqrt{nm}$, and Mg/Nb multilayers, ~ 10.8 $GPa \cdot \sqrt{nm}$. The Hall-Petch slope for Mg is 9.2 $GPa \cdot \sqrt{nm}$ [164]. The linear relation is quickly deviated at smaller layer thicknesses. Peak hardness of Mg/Nb is approached at h of ~ 5 nm and dropped slightly to ~ 2.6 GPa when h = 2.5 nm.

In contrast, for Cu/Nb and Al/Nb multilayers, peak hardnesses are approached at approximately the smallest layer thickness. The hardness of Mg/Nb is much greater than that of all pure Mg including those fabricated by ECAP [165].

III.5 Discussions

III.5.1 Microstructure

When h is greater than 10 nm, Mg/Nb multilayers possess predominantly hcp Mg and bcc Nb crystal structure with Mg (0002) and Nb (110) textures. At smaller h ($\leq$ 10 nm) several satellite peaks emerge due to the formation of superlattice structures and the intensity of Mg (0002) peak continuously decays. Furthermore small peaks other than hcp Mg or bcc Nb appear at angles between Mg (0002) and Nb (110).

The evolution of XRD patterns with layer thickness have been studied before in several systems. For instance, Schuller reported superlattices from XRD of Cu/Nb and Mo/Ni systems [166, 167], and Li et al investigated similar phenomenon in Fe/W multilayers [168]. Schuller refined the equation to calculate the XRD peak positions in fine multilayers. He considered three major characteristic length scales in superlattices: (i) the modulation wavelength Λ or bilayer thickness, and Λ = 2 h in this study, (ii) the interplanar spacing of constituents, and (iii) the structural coherency length, ξ , the distance over which the atomic positions are quantitatively correlated, and it can be estimated from the full width at half maximum of diffraction peaks using Scherrer's equation. Positions of superlattice peaks are indexed by [167]

$$\frac{2\sin\theta}{\lambda_x} = \frac{1}{\bar{d}} \pm \frac{n}{\Lambda} \tag{3.1}$$

where λ_x is the wavelength of x-ray, n is satellite order around the major peak, $\bar{d} = \Lambda/(N_A + N_B)$, N_A and N_B are the number of atomic planes of material A and B in one bilayer. $\bar{d}$ and Λ can be obtained from XRD data directly. ξ for Mg/Nb 10 nm is calculated to be ~ 94 Å, comparable to bilayer thickness. Hence two satellite peaks with n = ± 3 are identified besides the Nb (110) peak in Figure 26a. The bilayer thickness is estimated to be ~ 220 Å. The extra peak has a d spacing of 2.4776 Å, identical to the average of Mg (0002) and Nb (110) lattice spacing, indicating that coherency stress arises in Mg/Nb 10 nm multilayers. In Mg/Nb 5nm multilayers, ± 1 satellite peaks were calculated by using eq. (1.1). The negative third order satellite peaks were also identified. The bilayer thickness was computed to be ~ 91 Å based on the position of satellite peaks.

Microscopy studies reveal the formation of metastable bcc Mg along interface when h is 5 nm or less. The bcc Mg in examined regions appears to be fully coherent with Nb (Figure 30a). Hence transparent interface (refers to the interface separating two phases with identical lattice parameters, and crystal structure and orientation) forms in Mg/Nb 5 nm films in local regions. Transparent interfaces have also been observed in Cu/Ni and Ag/Al multilayers [138, 169]. Besides fully coherent Mg/Nb interface, hcp (Mg)/bcc (Nb) interface is also observed where Mg retains stable hcp phase. However a thin distorted layer, ~ 1nm, has been observed in Mg at interface. The microstructure of this distorted region separating two types of crystals shows a gradual transition from bcc to hcp structure (Figure 28a). In comparison, the interface between Cu/Nb and Al/Nb appears mostly dominated by K-S orientation relations [126, 170]. Metastable phases have been frequently observed in multilayers. Rajarshi et al. [171] reported structural transformations in Ti/Al multilayers. Nanolayers of Ti/Al show structural transition from hcp Ti to fcc Ti as the bilayer thickness decreases.

III.5.2 Strengthening mechanisms

When h is 50 nm or greater, Hall-Petch strengthening mechanism typically dominates in metallic multilayers. Hall-Petch slope is a measure of the strength of the interface boundaries to slip transmission and determines the rate of increase of strength with decreasing h. The slope is typically interpreted in terms of dislocation pile-ups in softer components against interfaces. However, the (0002) basal plane, which typically dominates dislocation activity in Mg, is parallel to the interface (based on XRD studies), hence dislocation pile-up in Mg against interface is less likely to be the major mechanism for slip transmission. Hence we consider dislocation pile-ups in Nb. Furthermore, we will show later that the opposite hypothesis considering dislocation pile-ups in Mg, if made, will lead to significant overestimation of peak strength of multilayers.

Hall-Petch slope, k, can be calculated as [172],

$$k = 0.18\,\mu\sqrt{b} \tag{3.2}$$

where μ and b is the shear modulus and Burgers vector of the stiffer components. The magnitude of Burgers vector of Nb is $a\sqrt{3}/2$, where a is lattice parameter. By using μ = 38 GPa and a = 0.286 nm for Nb, we obtain k of ~ 3.4 $GPa \cdot \sqrt{nm}$. When the Taylor factor of 3.1 is considered, we obtain a slope ~ 10.4 $GPa \cdot \sqrt{nm}$ which agrees with the experimental result, ~ 10.8 $GPa \cdot \sqrt{nm}$. For pure Mg with grain size on the order of microns, the Hall-Petch slope is measured to be 8 - 9 $GPa \cdot \sqrt{nm}$. In Table 2, we list the measured and estimated H-P slopes, as well as peak hardness. In general, the calculated slopes are in agreement with experimentally determined values.

Table 2. Comparisons of shear modulus, Hall-Petch slope (measured and calculated) and peak hardness of X/ Nb (X = Mg, Cu and Al) multilayers.

	Shear modulus (GPa)	Measured k ($GPa \cdot \sqrt{nm}$)	Calculated k ($GPa \cdot \sqrt{nm}$)	Measured peak hardness (GPa)	Calculated peak hardness* (GPa)
Mg/Nb	16/38	10.8	10.4	2.7	2.9
Cu/Nb	46/38	18.1	13.0	6.8	6.5
Al/Nb	25/38	14.1	10.4	4.8	4.6

* from measured Hall-Petch slope

We now attempt to estimate the peak hardness of multilayers by considering the interface barrier strength inferred from the measured Hall-Petch slope. The Hall-Patch slope is connected to interface barrier strength via the following relation [136]

$$k = \sqrt{\frac{\tau^* \mu b}{\pi (1-\nu)}} \tag{3.3}$$

where τ^* is the critical resolved shear stress for slip transmission of dislocation across interface (interface barrier strength). For Mg/Nb multilayers, when dislocation pile-ups in Nb raise the stress concentration at the leading dislocation to a critical value, the dislocation will transfer across interface and the composite will yield. By using the parameters of Nb, k of ~10.8 $GPa \cdot \sqrt{nm}$, and considering a Taylor factor of 3.1 and a hardness-to-flow stress transition factor of 2.7 [173], we obtain τ^* of ~ 0.34 GPa. This corresponds to a peak hardness of ~2.85 GPa, agrees well with our measured peak hardness of ~ 2.7 GPa. On the other hand, if we assume dislocation pile-up in Mg as the dominant yielding mechanism, the same analysis will lead to a peak hardness of ~ 6 GPa, significantly higher than experimental observations. Similar calculations show that for Cu/Nb and Al/Nb multilayers, peak hardnesses calculated from the measured Hall-Petch slope compare well to the experimentally determined peak hardness values, as shown in Table 2.

When h is in the range of tens of nm, dislocation pile-ups become less likely. Instead dislocations are likely to be confined within layers as described by a confined layer slip (CLS) model [123], which was developed later by Misra et al [123]. The modified CLS model considers arrays of misfit dislocations at interface, as well as interface stress. For a 60^{o} dislocation the modified CLS model describes the shear stress to propagate a dislocation across layer interface, τ_{cls}, as follows:

$$\tau_{cls} = \frac{\mu b}{8\pi h'}\left(\frac{4-\nu}{1-\nu}\right)\ln\left(\frac{\alpha h'}{b}\right) - \frac{f}{h} + \frac{C}{\lambda} \qquad (3.4)$$

where α determines the dislocation core cut-off radius, and h' is the layer thickness along the glide plane. f is the interface stress, λ is the average spacing between misfit dislocations at interface, and C is approximately $\mu b/(1-\nu)$. A good fit to the plot of hardness vs. layer thickness has been obtained for Cu/Nb multilayers. In Mg/Nb multilayers, there are numerous parameters, f and λ, that are not yet known, hence an analytical calculation based on the modified CLS model cannot be performed.

At smaller h, 10 nm or less, the hardness of multilayer approaches a plateau and slightly decreases thereafter. At this length scale, we attempt to estimate Koehler stress, τ_k, originated from large shear modulus mismatch between Mg and Nb by [137]

$$\tau_k = \frac{\mu_{Nb} - \mu_{Mg}}{\mu_{Nb} + \mu_{Mg}} \frac{b\mu_{Mg}}{4\pi h_c} \qquad (3.5)$$

where h_c is the distance of dislocation to interface and is estimated as 2b. Koehler stress in Mg/Nb system is estimated to be ~ 0.26 GPa. Hence the hardness increase due to Koehler stress is ~ 2.15 GPa by using similar factors mentioned previously. Considering the friction stress, indicated by ~ 0.6 GPa hardness intercept inFigure 31b for Mg/Nb multilayers, the peak hardness is ~ 2.8 GPa, close to experimentally determined peak hardness. This is much higher than a majority of Mg and Mg alloys reported in the literature. The peak hardness in Cu/Nb is much greater than Mg/Nb and Al/Nb since MD simulations have shown that the Cu/Nb interface is weak under shear stress. Dislocation cores can spread to a diameter of 5b, and can be trapped by the interface, hence making the transmission of dislocation difficult [140].

Slight softening may occur when h is less than 5 nm in Mg/Nb multlayers. This phenomenon, yet to be confirmed by further experiments, could be related to the formation of coherent interface as shown by HRTEM studies of bcc Mg grown epitaxially on Nb. It has been shown that coherent interface can reduce the Koehler stress in Cu/Ni epitaxial multilayers [138]. Also when layer thickness reduces to a value comparable to the dislocation core width, Koehler stress may decrease considerably [138].

III.6 Conclusions

The microstructure and mechanical behavior of sputter-deposited Mg/Nb multilayer films were investigated and the hardness of Mg/Nb was compared to those of Mg and Cu/Nb and Al/Nb multilayer systems. Metastable structure of bcc Mg at interface was revealed in Mg/Nb 5 nm multilayers. The interface barrier strength computed from Hall-Petch slope shows interphase interfaces in Mg/Nb is a strong barrier to slip transmission. Peak hardness of the multilayers, estimated from H-P model and Koehler stress, is in good agreement with experimental data, and is greater than hardness of most other Mg and Mg alloys reported to date.

CHAPTER IV

HYDROGEN SORPTION IN ORTHORHOMBIC MG HYDRIDE AT ULTRALOW TEMPERATURE[*]

IV.1 Overview

Mg can store up to ~ 7 wt.% hydrogen and has great potential as light-weight and low cost hydrogen storage materials. However hydrogen sorption in Mg typically requires ~ 573 K, whereas the target operation temperature of fuel cells in automobiles is ~ 373 K or less. Here we demonstrate that stress-induced orthorhombic Mg hydride (O-MgH_2) is thermodynamically destabilized at ~ 373K or lower. Such drastic destabilization arises from large tensile stress in single layer O-MgH_2 bonded to rigid substrate, or compressive stress due to large volume change incompatibility in Mg/Nb multilayers. H desorption occurred at room temperature in O-MgH_2 10 nm / O-NbH 10 nm multilayers. Ab inito calculations show that constraints imposed by the thin-film environment can significantly reduce hydride formation enthalpy, verifying the experimental observations. These studies provide key insight on the mechanisms that can significantly destabilize Mg hydride and other type of metal hydrides.

---

[*] This chapter reprinted with permission from “Hydrogen sorption in orthorhombic Mg hydride at ultralow temperature” by B. Ham, et.al, International Journal of Hydrogen Energy, 38 (2013) 8328–8341, Copyright 2013 by Elsevier.

IV.2 Introduction

Onboard hydrogen storage is one of the major technical barriers to the widespread use of hydrogen fuel because the properties of current hydrogen storage materials fall far from the hydrogen vehicle requirements [32, 174-176]. Mg is the third most abundant element on earth and has high hydrogen uptake capacity [1, 174]. However, hydrogen absorption occurs at ~ 573 K in bulk Mg [6, 177, 178], much higher than practical application temperatures (~ 373 K). The kinetics of absorption is considered to be controlled by chemical reaction, absorption of H, or permeation of adsorbed H through the surface [179-182]. The predominantly observed MgH_2 has tetragonal phase, and once formed, is rather stable up to 573 K. The slow kinetics and high thermal stability of tetragonal MgH_2 (T-MgH_2) are major hurdles for using Mg for transportation applications.

Several approaches have been used to improve H sorption kinetics in Mg. Compared to their bulk counterparts, nanostructured materials have larger surface area, more nucleation sites for hydrogen reactions, and shorter path for hydrogen diffusion, and hence may lower the kinetic barriers for the hydrogenation [37, 183, 184]. Nanocrystalline (nc) Mg with high-angle grain boundaries prepared by mechanical milling can expedite the kinetics [37, 185, 186], but nanograins coarsen during thermal desorption [50, 51]. To enhance the kinetics even further in Mg-based nc materials, a variety of catalyst and additives (metals and transition-metal oxides) has been incorporated [51, 53-56, 187]. Vajo et al. showed that thermodynamic destabilization in metal hydrides can be achieved by using certain additives that form new compounds during dehydrogenation [63-65]. Many supersaturated Mg solid solutions are not stable; i.e., they decompose upon hydrogenation [66]. Studies on Mg and related films are also active. In general H sorption kinetics was improved by refinement of grain size or addition of alloying element via co-sputtering [82-85]. Niessen and Notten observed enhanced kinetics in metastable crystalline single-phase $Mg_{0.8}X_{0.2}$ (X = Sc, Ti, V, Cr) compound film by e-beam co-deposition [81]. Several studies showed the effects of alloying on the hydrogen storage properties at room temperature [87, 95, 188-190]. A reduction of the Mg grain size showed improved hydrogen uptake kinetics with the segrated additives phase acting as a fast diffusion distance.

Certain Mg-based multilayer films showed improved H sorption kinetics, however the thermodynamic stability of MgH_2 was again little affected [70, 86, 106, 110-114], and significant interface intermixing frequently occurred during hydrogenation in certain multilayers [112, 115]. The formation of intermetallic compound can be prevented by insertion of a buffer layer [105]. Also clamped metal hydride thin films show modified thermodynamics and varying hydrogen solubility in metal-hydrogen systems [116-118].

Here we unveil that stress induced metastable orthorhombic MgH_2 (O-MgH_2) leads to drastic destabilization of Mg hydride. In single layer Mg films on a rigid substrate, stress arising from substrate induces O-MgH_2, which desorbs H at ~ 373 K. In immiscible Mg/Nb multilayers, the volume-expansion-incompatibility induced stress leads to O-MgH_2 that desorbs H_2 even at room temperature. Detailed microstructural studies were correlated with the hydrogen sorption experiments. *Ab initio* calculations complement the experimental studies and confirm the instability of O-MgH_2. Although a real hydrogen storage system using Mg hydride may have lower storage capacity, this study offers a solution that may pave the way for the design of advanced Mg and other light metal hydrides for various applications.

IV.3 Experimental

Mg/Nb multilayers with individual layer thickness of 10 and 100 nm were deposited by DC magnetron sputtering on oxidized Si (100) substrates with 1μm thermal oxides and glass slides at room temperature. The base pressure of the sputter chamber was better than 6.6×10^{-6} Pa prior to deposition. Mg, Nb and Pd targets, with higher than 99.99% purity, were used. A 25 nm thick Pd cap layer was deposited on top of all films to protect samples from oxidization and catalyze the dissociation of hydrogen molecules. In multilayers the top and bottom layer were Nb so that Mg would not directly contact substrate or Pd. The films were grown under ~ 0.33 Pa Argon. Mg and Nb single layer films, 1.6 μm in thickness, were deposited on Si substrates (2.5 cm × 5 cm). Glass substrates were used for the deposition of 10 μm thick Mg 100 nm / Nb 100 nm multilayers, and 30 μm thick Mg films. The deposition rates for Mg and Nb were ~2 and ~0.5 nm/s, respectively.

After deposition, samples were transported directly into a custom-made high vacuum annealing chamber for hydrogen loading and unloading studies. The base pressure of chamber was ~ 6.66×10^{-5} Pa before hydrogen loading. Unless specified, most samples were hydrided at a hydrogen pressure of 0.25 MPa at 373 K for 24 hours. Certain specimens were hydrided at 353 K for 12 hours. Hydrogen desorption were performed by thermal desorption spectroscopy (TDS) method enabled by a quadruple mass spectrometer in a residual gas analyzer (RGA). Samples were heated from room temperature up to a maximum of 623K at a constant heating rate of 4 K/min. Pressure-Composition-Isotherm (PCI) curve measurements were performed by using ASAP 2020 volumetric absorption analyzer. A high-purity grade (99.999%) of hydrogen gas was used. Before hydrogen loading, the sample was degassed at elevated temperature under the vacuum. The experiments were reproduced at three different places.

X-ray diffraction (XRD) experiment was performed on a Bruker-AXS D8-focus Bragg–Brentano X-ray diffractometer. Morphology and structure of as-deposited and hydrided films were examined by scanning electron microscopy (SEM) technique using a JEOL JSM-7500 field emission scanning electron microscope operated at 5 kV. Transmission electron microscopy (TEM) specimens were prepared by grinding, polishing followed by low energy argon ion milling. TEM studies were performed by using a JEOL 2010 microscope operated at 200 kV.

Neutron reflectivity measurements took place in the Surface Profile Analysis Reflectometer (SPEAR) beamline at the Manuel Lujan Neutron Scattering Center, Los Alamos National Laboratory. Neutron Reflectivity R(q) of a surface is defined as the intensity ratio of the number of particles (neutrons) between reflected and incident neutron beam. NR is measured as a function of the scattering vector, $q = (4\pi / \lambda) \sin \theta$, where θ is the angle of incidence and λ is the neutron wavelength [191-193]. The curve fitting was done by using the free software ‘Parratt 32’ based on recursive Parratt formalism [191].

The synchrotron XRD experiments were carried out at the 11-ID-D beam line at the Advanced Photon Source, Argonne National Laboratory, USA with a wavelength of = 0.0774901 nm. Two dimensional diffraction patterns were recorded using a Pilatus area detector. The 2D images were converted to 1D XRD plot by using "FIT2D" program.

IV.4 Results

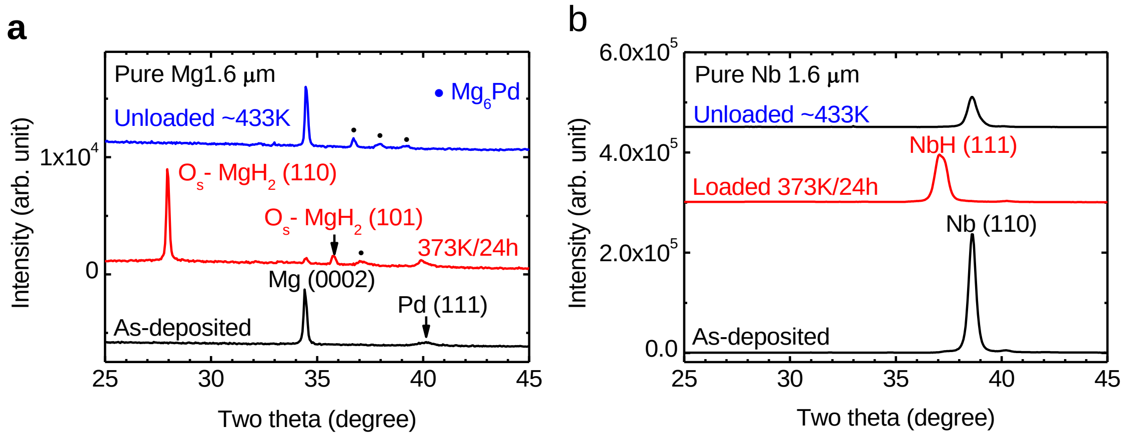

Figure 32. (a) XRD profile shows that hydrogen loading of Mg film (at 373K/ 24h) led to the formation of metastable, (110) textured orthorhombic MgH_2, labeled as O_s-MgH_2 (subscript S denotes single layer), which upon unloading at 433K, almost completely transformed back to Mg. (b) Nb has undergone reversible phase transformation when hydrided at similar condition. Hydrogenation of (c) Mg/Nb 100 nm and (d) Mg/Nb 10 nm multilayers at the same condition resulted in the formation of (200) textured O_m-MgH_2 (m denotes multilayers). (e) Thermal desorption spectroscopy (TDS) of H in various films shows multilayers had lower hydrogen desorption temperature than single layer films. Multilayers loaded at 353K/12h had lower desorption temperature than those loaded at 373 K/24 h. (f) Comparisons of TDS profiles show poor H sorption in 30 μm thick, free-standing Mg films; whereas 30 μm thick Mg films on substrate had performance similar to those of 1.6 μm Mg film on substrate. The 10 μm thick free-standing Mg/Nb 100 nm films had the best performance among three specimens.

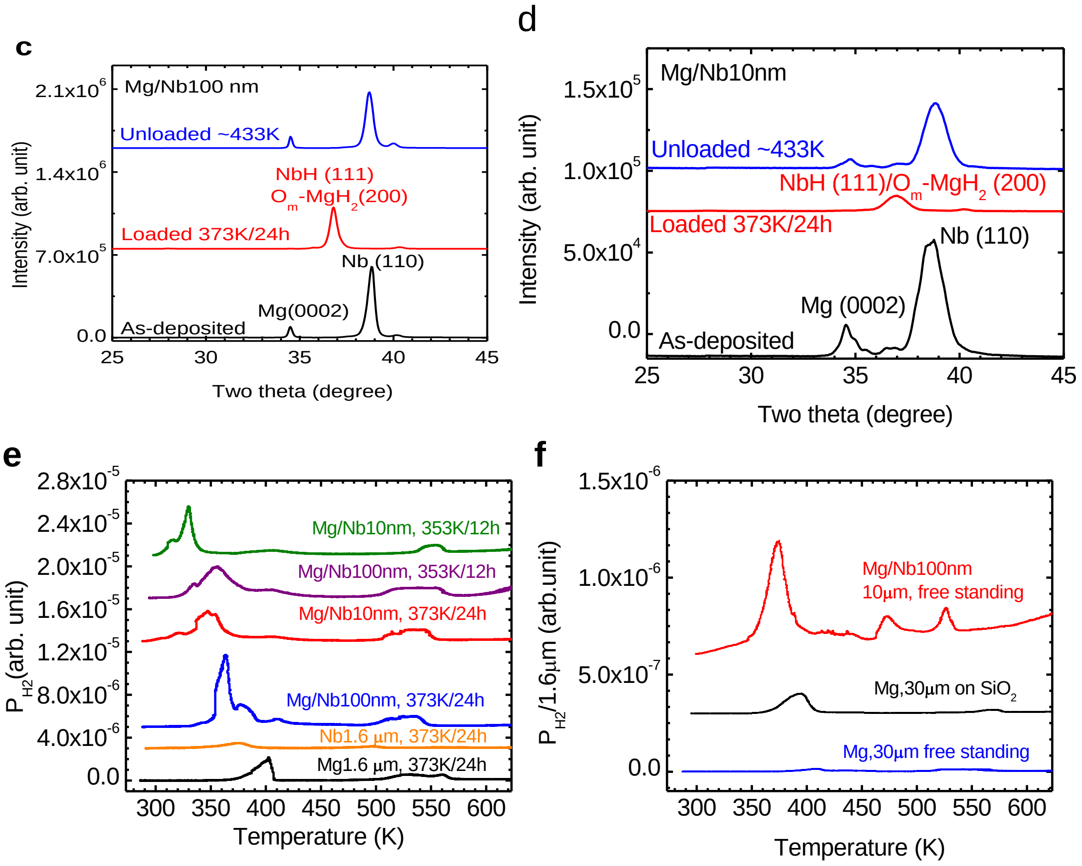

Figure 32 Continued.

X-ray diffraction experiments (XRD) (Figure 32a) show that after hydrogen loading (373K/24h), as-deposited Mg (1.6 μm on Si substrate) transformed to an orthorhombic (110) textured O_s-MgH_2 (S denotes single layer) with a prototype of $CaCl_2$. After hydrogen desorption at 433K, the Mg was recovered. During hydrogenation at the same condition, (110) textured Nb was entirely transformed to orthorhombic NbH (O-NbH) with (111) texture (Figure 32b). As-deposited Mg 100 nm / Nb 100 nm multilayer (referred to as Mg/Nb 100 nm thereafter) had texture of Mg (0002) and Nb (110) (Figure 32c). After hydrogen absorption a single peak was observed due to the overlap of O-

NbH (111) and (200) textured orthorhombic Mg hydride (O_m-MgH_2, m denotes multilayer). Mg and Nb peaks nearly completely recovered after H desorption. Similar phenomenon was observed during hydrogenation of Mg/Nb 10 nm multilayers (Figure 32d). The orthorhombic MgH_2 phases in both single layer and multilayer films had the $CaCl_2$ type of structure, but their lattice parameters and texture were quite different. The crystal structures of O_s-MgH_2 and O_m-MgH_2 were examined in detail by synchrotron XRD experiments (Figure 33 and). Figure 32e compares the evolution of H pressure with temperature for all the hydrided films (on oxidized Si substrate) during thermal desorption spectroscopy (TDS) studies. In samples containing MgH_2, TDS spectra consisted of intense peaks at 400 K or less, and much weaker peaks at ~ 523 K. In single layer MgH_2, H pressure reached a peak at ~ 400 K. NbH films showed a desorption peak at 373 K, close to that in bulk NbH (~ 361 K) [194]. Multilayers loaded at 373 K / 24 h started H desorption at lower temperatures. When multilayer were loaded at lower temperatures (353K/12h), H desorption took place at room temperatures. To understand the effect of stress on H sorption, three sets of specimens were studied (Figure 32f). 30-μm thick Mg film on substrate showed a desorption peak at ~ 393 K, similar to that of 1.6-μm thick MgH_2 films on substrate, whereas the free-standing 30-μm thick Mg film showed negligible H desorption. Meanwhile the 10-μm thick, free-standing Mg/Nb 100 nm multilayers showed a much stronger desorption peak at ~ 373 K.

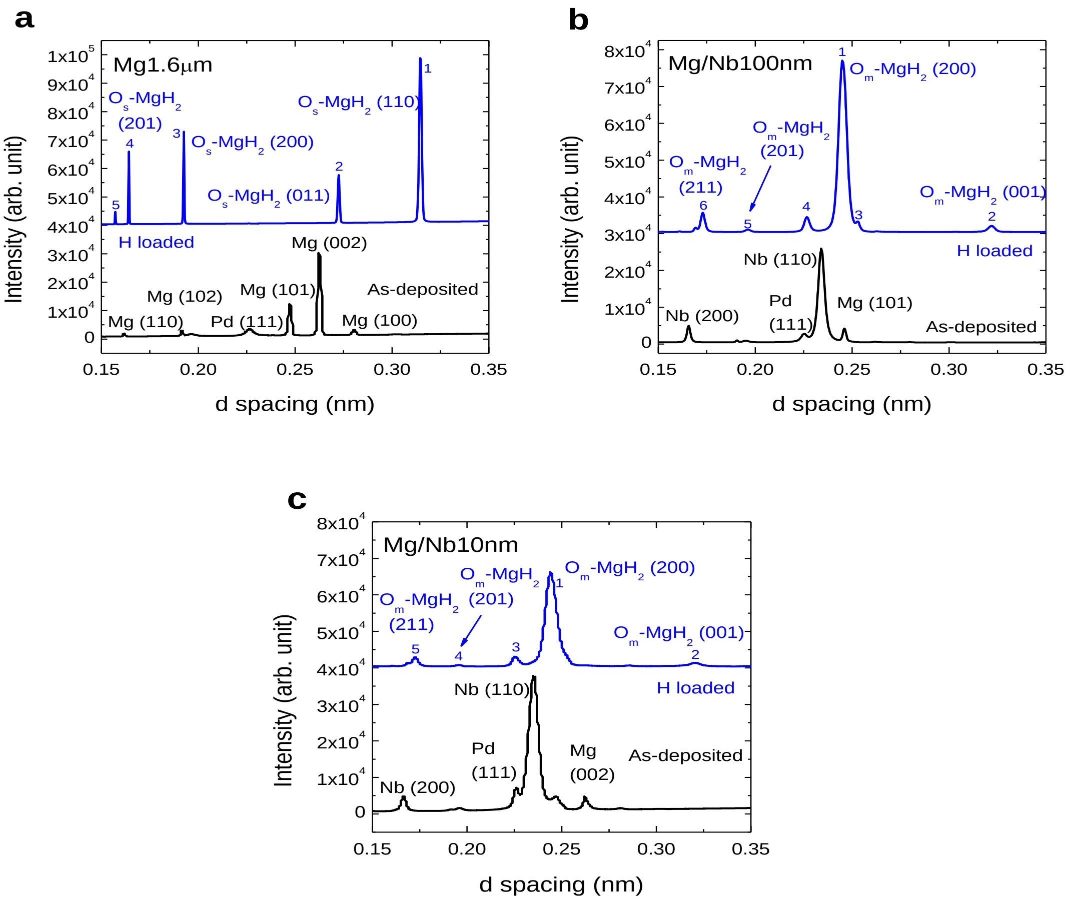

Figure 33. Synchrotron X-ray diffraction profiles of as-deposited and hydrogen loaded (a) Mg, (b) Mg/Nb 100nm and (c) Mg/Nb 10nm multilayers. After Hydrogen loading (373K / 24h), the single layer Mg films completely transformed to O_s-MgH_2 with strong (110) texture, whereas the multilayer films transformed to O_m-MgH_2 with (200) texture and O-NbH phase with (111) texture.

Figure 33 shows synchrotron X-ray diffraction profiles of as-deposited and hydrogen loaded (a) Mg, (b) Mg/Nb 100nm and (c) Mg/Nb 10nm multilayers. After Hydrogen loading (373K / 24h), the single layer Mg films completely transformed to O_s-MgH_2 with strong (110) texture, whereas the multilayer films transformed to O_m-MgH_2

with (200) texture and O-NbH phase with (111) texture. Index and d-spacings of numbered peaks are summarized in our published article.

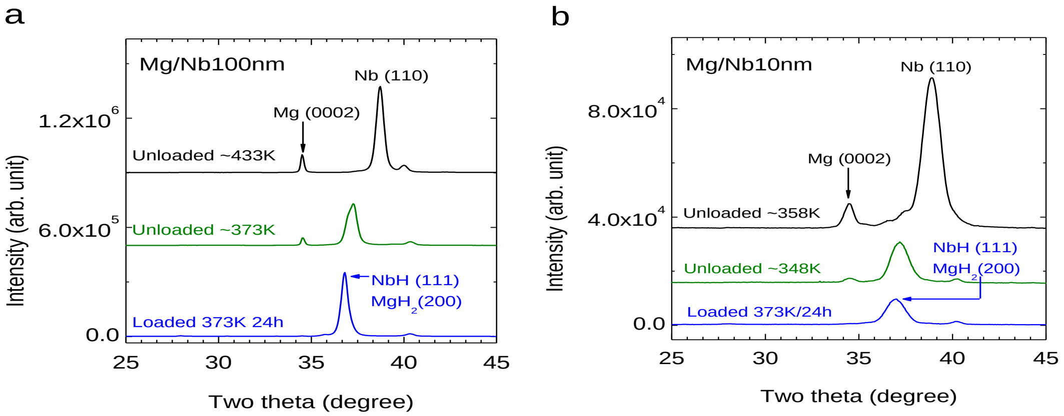

Figure 34. XRD experiments to probe phase transformations revealed from TDS experiments in Figure 32e. (a) After H desorption of hydrided Mg/Nb 100 nm at 373K, the Mg phase recovered, whereas NbH remained. Thus the first desorption peak of Mg/Nb 100 nm (373K/24h) in Figure 32e corresponds to H desorption of O_m-MgH_2. Desorption at 433 K led to complete recovery of as-deposited states. (b) Similarly in hydrided Mg/Nb 10nm multilayers, desorption occurred first from O_m-MgH_2 at 348K, followed by recovery of Nb phase.

To explore the origin of two desorption peaks (362 and 378K) in TDS spectrum of hydrided Mg/Nb 100 nm (shown in Figure 32e), XRD profiles were collected by interrupting desorption in between the two peaks. Figure 34 shows that unloading at 373 K led to the recovery of Mg, but Nb was not detectable, thus it is evident the first peak in TDS spectrum of Mg/Nb 100 nm film arose from the desorption of MgH_2. Similarly, Mg recovered proceeding Nb in hydrided Mg/Nb 10 nm multilayer as shown in Figure 34b.

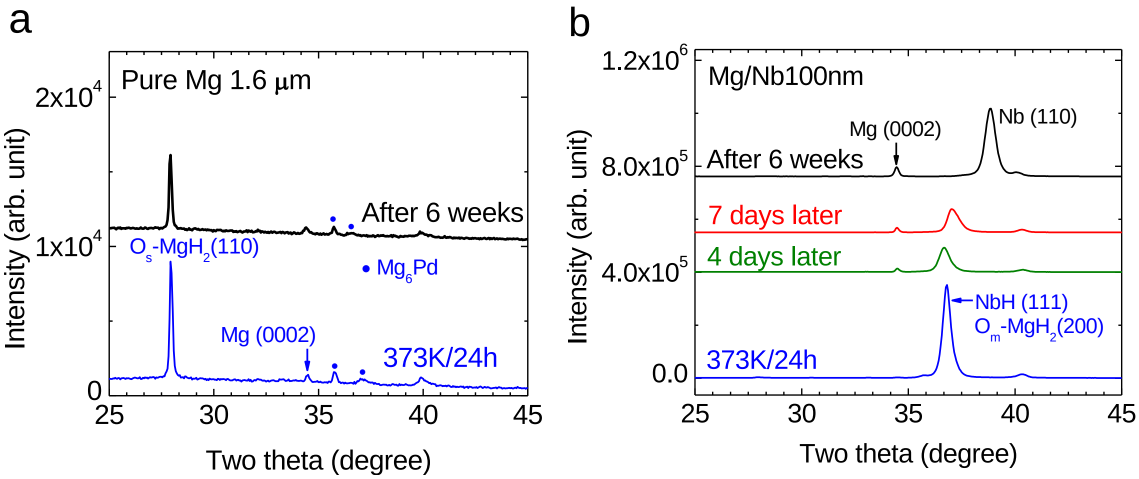

Figure 35. Stability of Mg hydride at room temperature. (a) After 6 weeks, the single layer O_s-MgH_2 remained stable. (b) In hydrided Mg/Nb 100 nm multilayers, Mg was partially recovered at room temperature in several days. By 6 weeks, Mg and Nb were fully recovered.

Figure 35 shows time dependent evolution of microstructure at room temperature. In 6 weeks, the single layer O_s-MgH_2 remained. Meanwhile in hydrided Mg/Nb 100 nm films, Mg recovered in 3-4 days, and complete recovery occurred in 6 weeks. The comparative study indicates that layer interfaces significantly enhance the desorption kinetics of MgH_2.

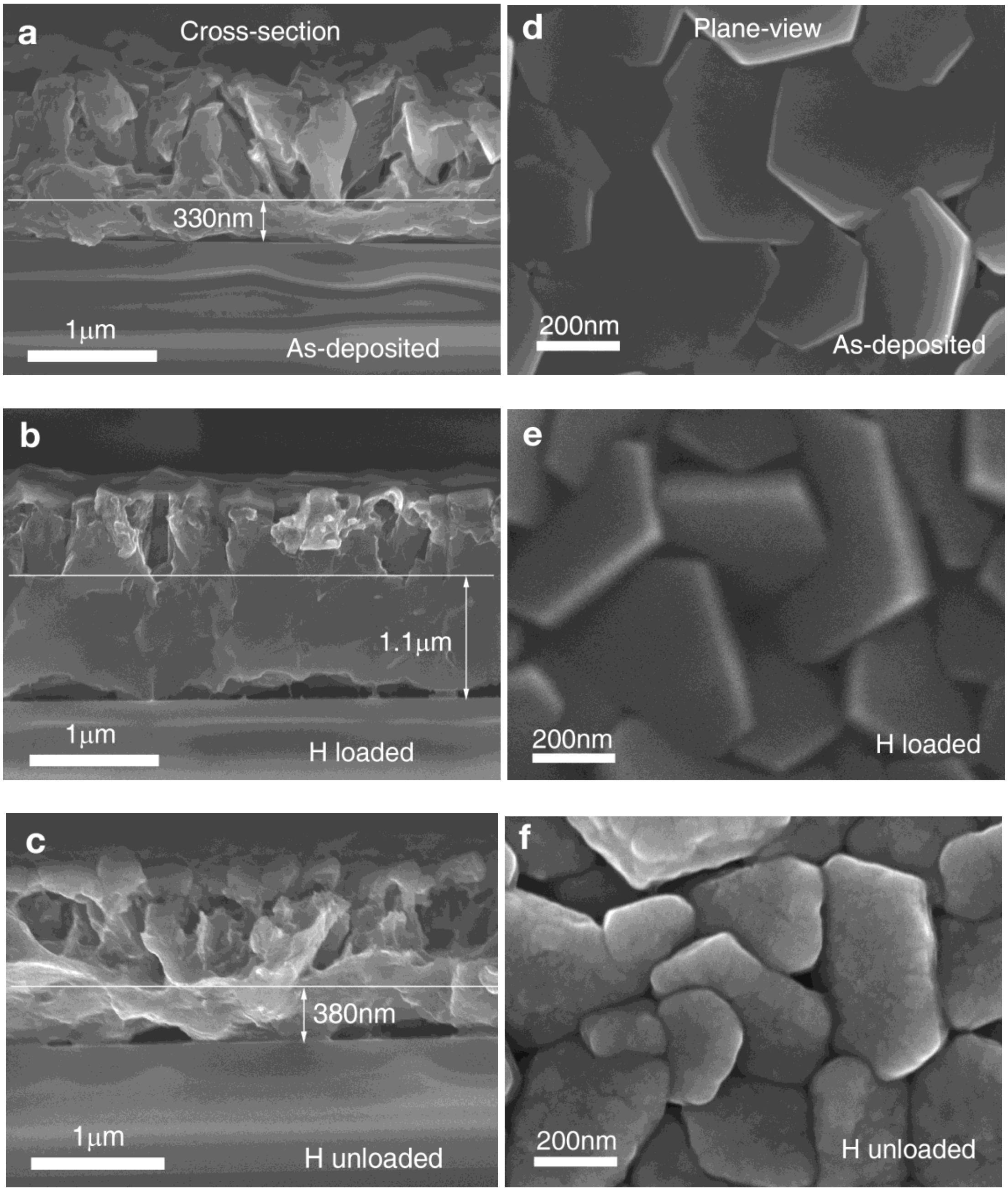

Figure 36. Cross-sectional SEM (XSEM) and Plane-view micrographs of single layer Mg during H sorption studies. (a) As-deposited Mg films had a dense layer, ~ 330 nm in thickness, and became porous thereafter. (b) After hydrogen loading (373K/24h),MgH_2 formed and had a ~ 1.1 μm thick dense layer. (c) After desorption (433K), films nearly reverted back to original morphology. (d) As-deposited Mg films had hexagon-shape, faceted platelet structure. (e) Hydrogen loaded Mg film still exhibited faceted platelet morphology. (f) After hydrogen desorption, the surface of platelets became rougher and facets appeared rounded.

Scanning electron microscopy (SEM) images (Figure 36) showed the evolution of morphology of films during H. As-deposited Mg (Figure 36a) had a dense zone, ~ 330 nm in thickness, close to substrate and became porous thereafter. After hydrogen loading, a dense layer, ~ 1.1 μm in thickness, formed due to hydrogenation induced significant volume expansion (Figure 36b). After hydrogen desorption, the Mg film regained its porous morphology (Figure 36c). Morphological changes during hydrogen sorption of single layer Mg films are shown in Figure 36d-f. As-deposited Mg films had randomly oriented hexagonal platelets and, after hydrogen loading, they still showed faceted platelet morphology. After hydrogen unloading, platelets became rougher and rounded.

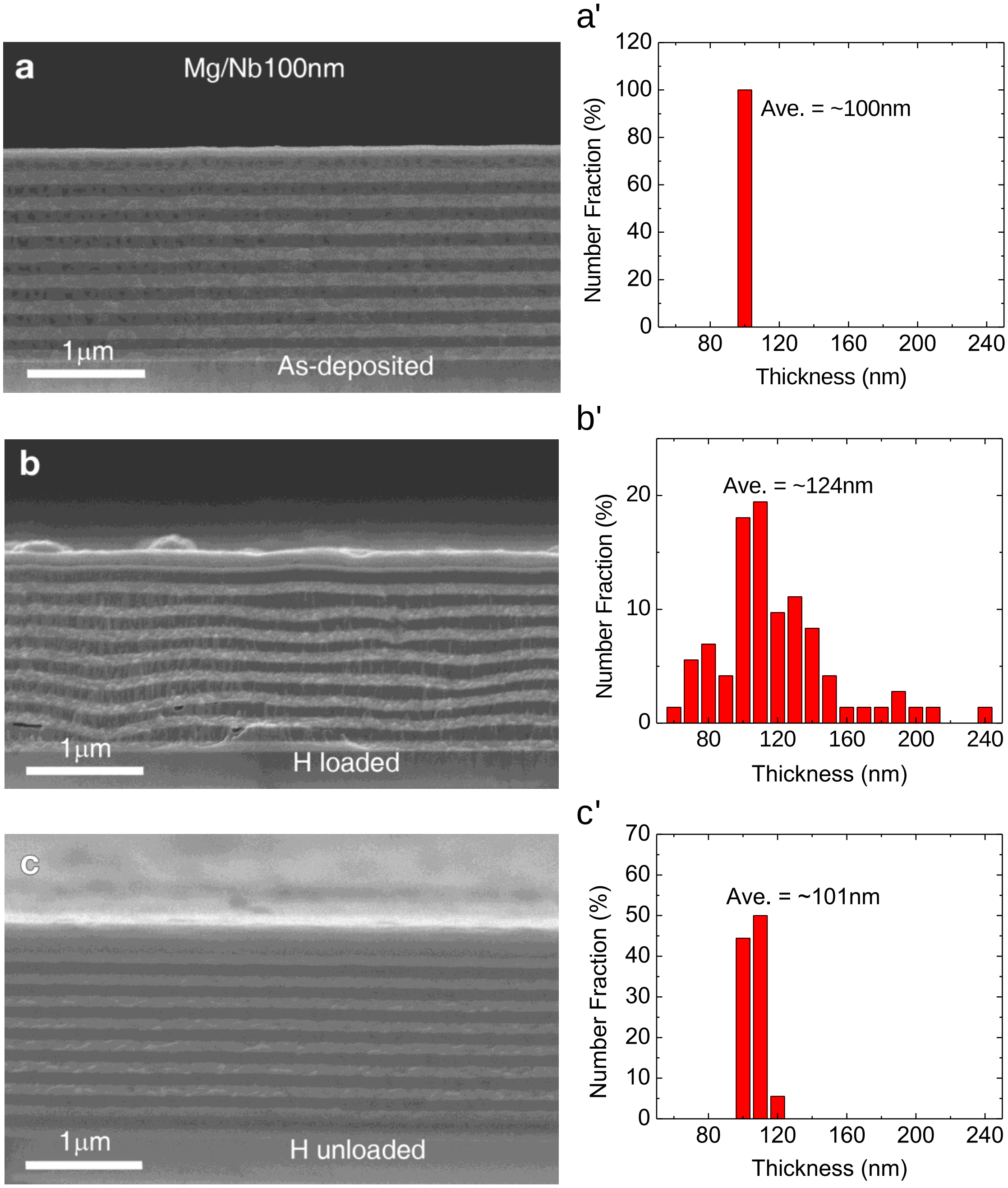

Figure 37. (a-c) Reversible H sorption was also revealed in Mg/Nb 100 nm multilayer. Interfaces became wavy after hydrogen absorption due to large volume expansion but remained stable. Statistical distribution of Mg or MgH_2 layer thickness in Mg/Nb 100 nm multilayers during H sorption studies. (a') As-deposited films have identical layer thickness. (b') H loading led to wide-spread distribution of layer thickness of MgH_2, with an average value of ~ 124 nm. (c') After H desorption, the average thickness of Mg recovered.

Figure 37a-c show that during hydrogenation of Mg/Nb 100nm multilayers, layer interfaces remained stable and phase transformation was reversible. Figure 37a’-c’ show the evolution of layer thickness during H sorption studies of Mg/Nb 100 nm films. The individual layer thickness varied from 100 nm to an average of 124 nm (spreading across 60-240nm) after H loading. After desorption, the individual layer thickness became uniform and reverted back to ~ 100 nm. Interfaces became wavy after hydrogen absorption due to large volume expansion but remained stable. Reversible morphological evolution was also identified in hydrided Mg/Nb 10 nm films (Figure 38a-c), wherein variation of layer thickness, by ~ 25%, was confirmed separately by neutron reflectivity measurement in Figure 39.

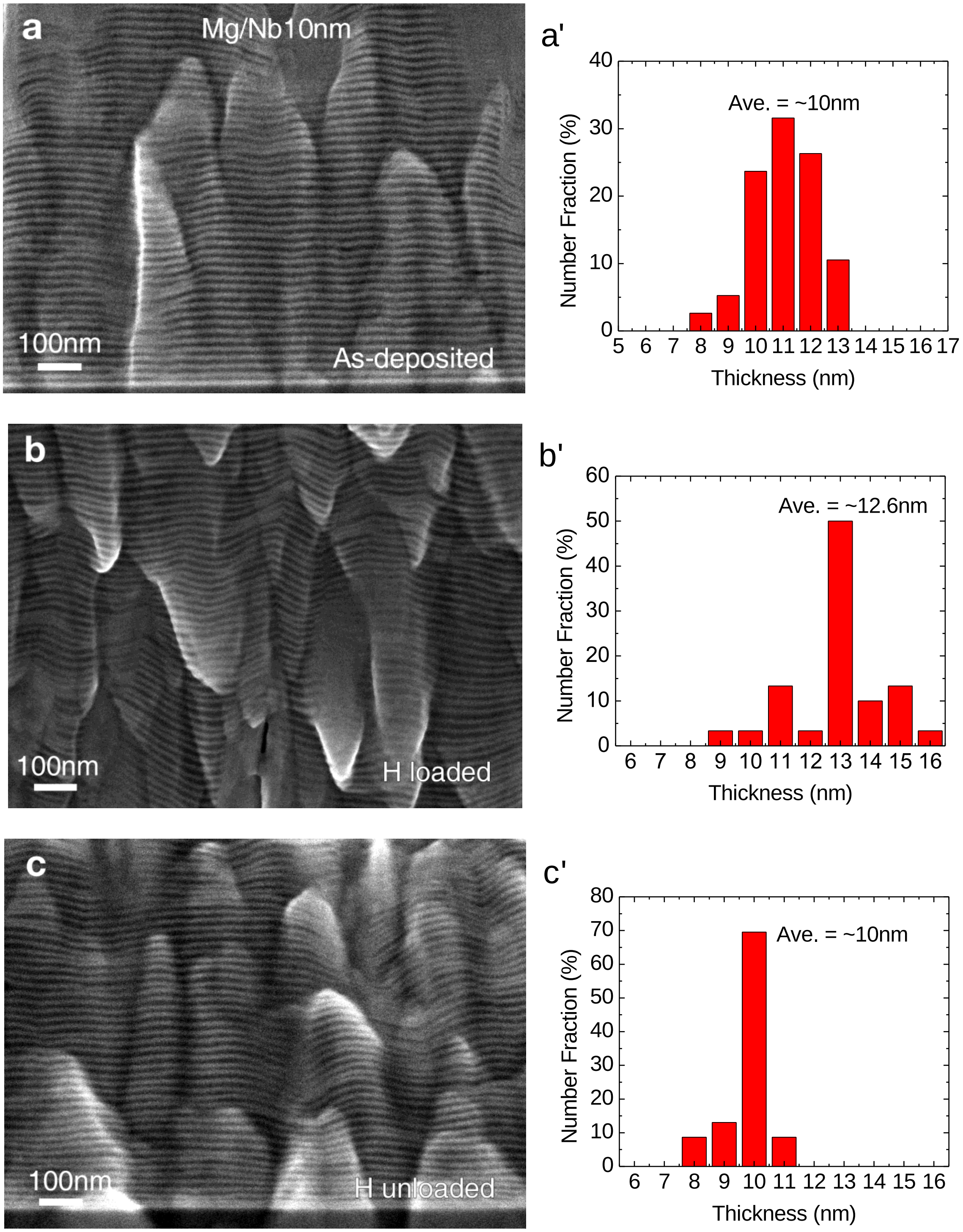

Figure 38. XSEM micrographs of Mg/Nb 10 nm multilayers in (a) as-deposited, (b) hydrided and (c) dehydrided states. Layer interface retained after hydrogen sorption studies. (a'-c') The thickness of Mg increased to 12.6 nm after H absorption, and recovered after desorption.

Figure 38a-c shows back-scattered XSEM micrographs of Mg/Nb 10 nm multilayers during H sorption studies. Similar to Mg/Nb 100 nm films, clear and discernible Mg and Nb layers are observed in all states. Layer interface remained continuous and multilayers were attached to the substrate throughout the H sorption studies. The films have undergone substantial volume change in Mg, by ~ 26%, during hydrogen sorption. Figure 39 shows the neutron reflectivity measurement for Mg/Nb 10 nm trilayers, the thickness of Mg increased by 24%, from 10.0 to 12.4 nm, consistent with XSEM investigations (Figure 38).

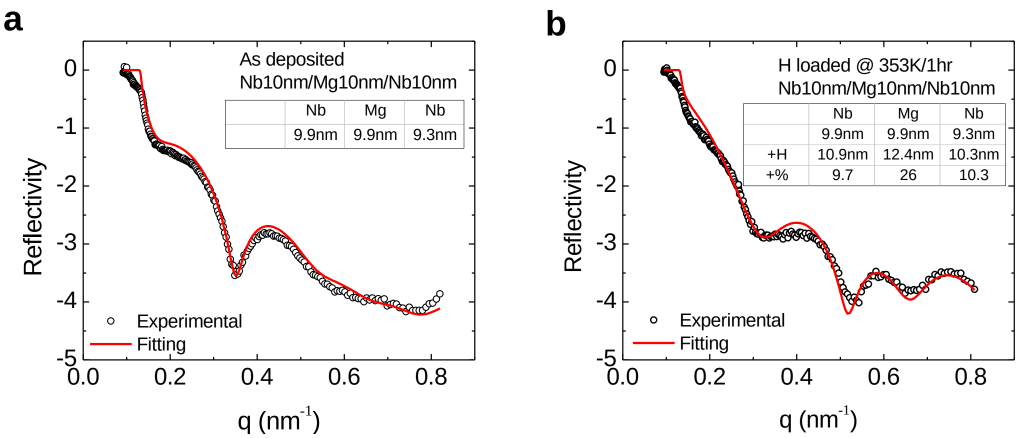

Figure 39. Neutron reflectivity profile of a Nb10nm/ Mg10nm/ Nb10nm trilayer film with Pd cap layer on oxidized Si (100) substrate in (a) as deposited and (b) hydrogen loaded (353K / 1 h) states. Open circles correspond to experimental data and solid lines correspond to curve fittings. It is evident that the thickness of Mg increased from 10 to 12.4 nm after H absorption.

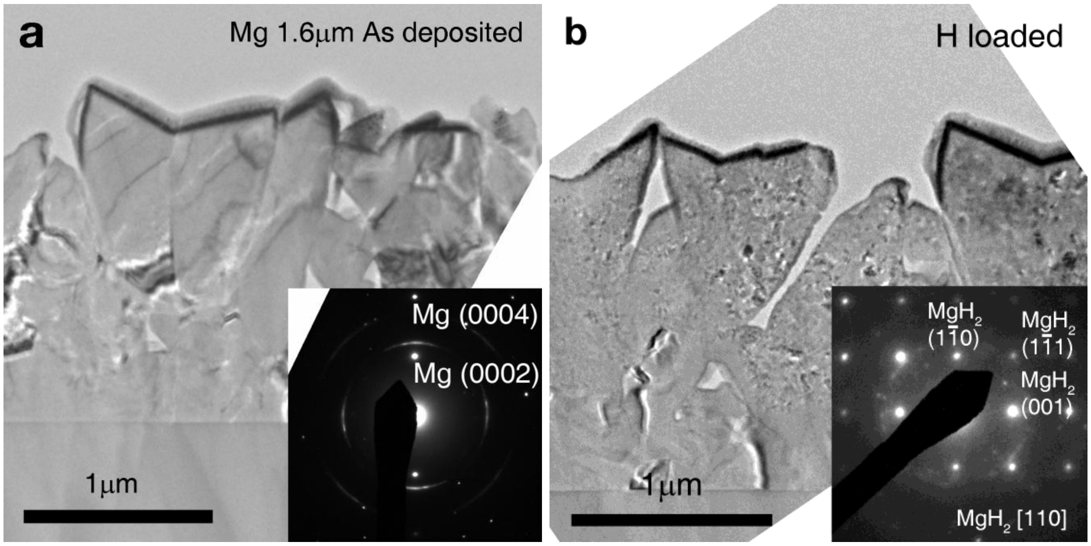

Figure 40. (a) XTEM micrographs of as-deposited Mg films showing the strong Mg (0002) texture. (b) MgH_2 films (H loaded state). The selected diffraction pattern clearly indicates the formation of O_s-MgH_2 films examined along [110] zone axis.

Cross-sectional transmission electron microscopy (XTEM) studies (Figure 40a) shows XTEM image of single layer Mg film exhibiting strong Mg (0002) texture. Top surface of the film shows porous and sharp structure similar to XSEM images shown in Figure 40. After H loading, hcp Mg transformed into O_s-MgH_2 phase, consistent with XRD studies of the same film.

XTEM micrograph shows that as-deposited Mg/Nb 10 nm film (Figure 41a) had clear layer interfaces with strong fiber texture of Mg (0002) and Nb (110). The hydrided multilayers remained highly textured with fully continuous, clear interfaces (Figure 41b). O_m-MgH_2 {200} coincided with the NbH {111} diffraction spots (Figure 41c). Compared to T-MgH_2, O_m-MgH_2 carried in-plane compression (Figure 41d), ~ 3.7%, and out-of-plane tension, ~ 6.8%, whereas O-NbH has insignificant strain variation.

Similar microstructural and phase evolution were observed in hydrided Mg/Nb 100 nm films in Figure 42.

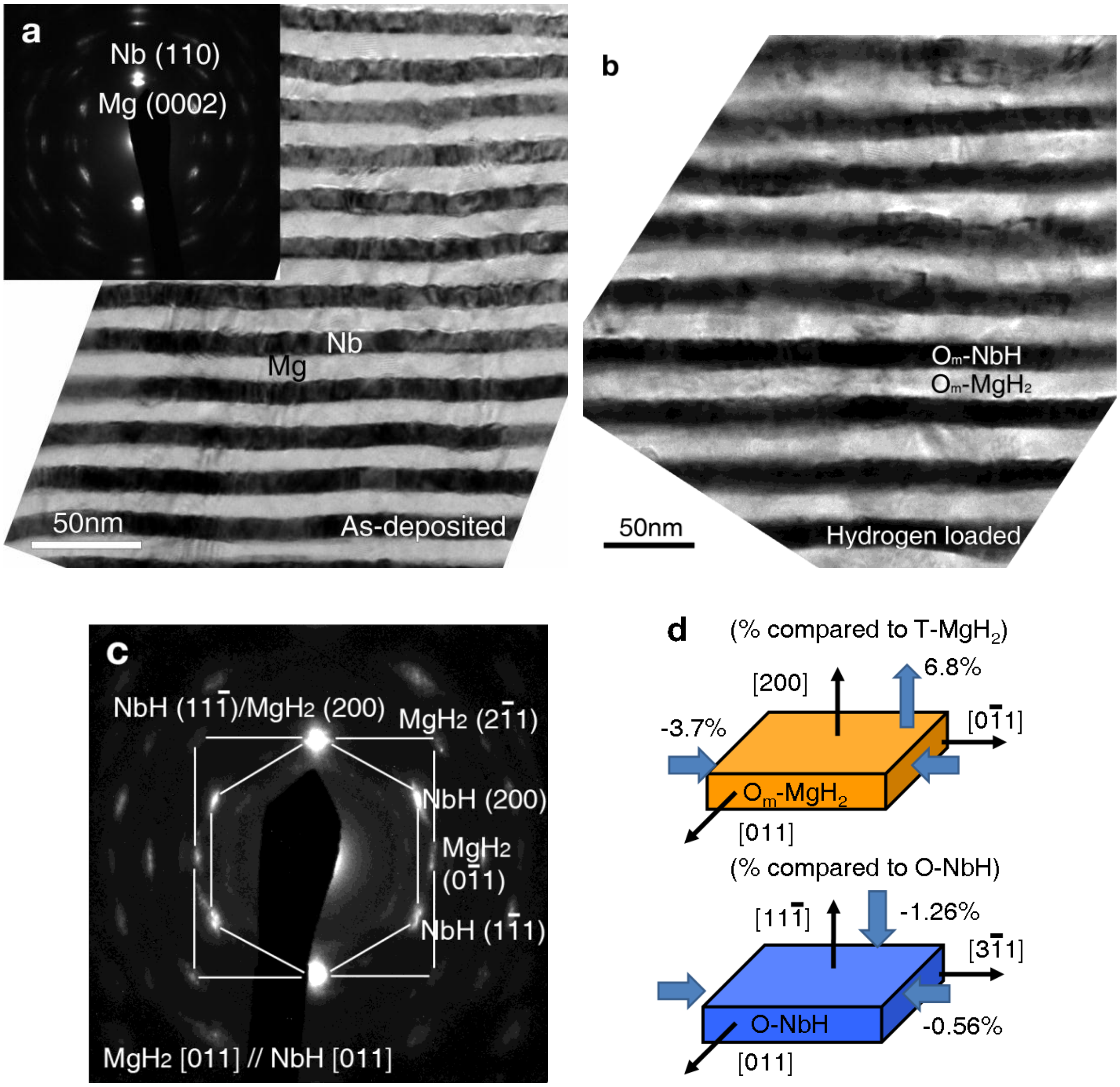

Figure 41. XTEM micrographs of Mg/Nb 10 nm multilayers. (a) As-deposited films had strong Mg (0002) and Nb (110) fiber texture with clearly discernable layer interface. After hydrogen loading, the interface remained unmixed (b) and showed strong orthorhombic MgH_2 (200) and NbH (111) fiber texture (c). (d) shows the orientation relationship between O_m-MgH_2 and O-NbH and the change of d spacing compared to stable hydrides.

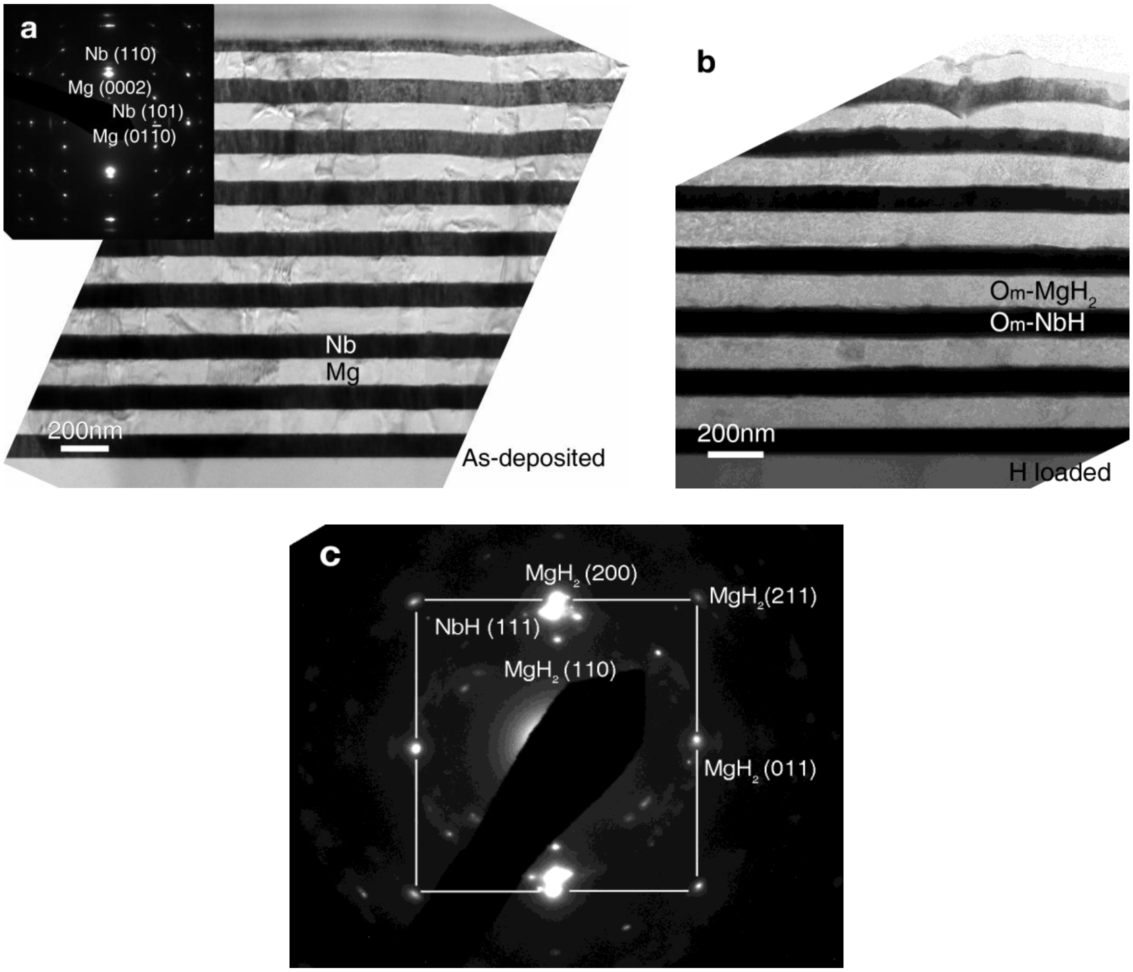

Figure 42. (a) XTEM micrograph of as-deposited Mg/Nb 100 nm multilayers showing highly textured films in which Mg (0002) // Nb (110). (b) After hydrogen absorption, interface remains chemically abrupt, but the diffraction pattern of multilayers has completely changed, and shows that Om-MgH$_2$ (200) // O-NbH (111).

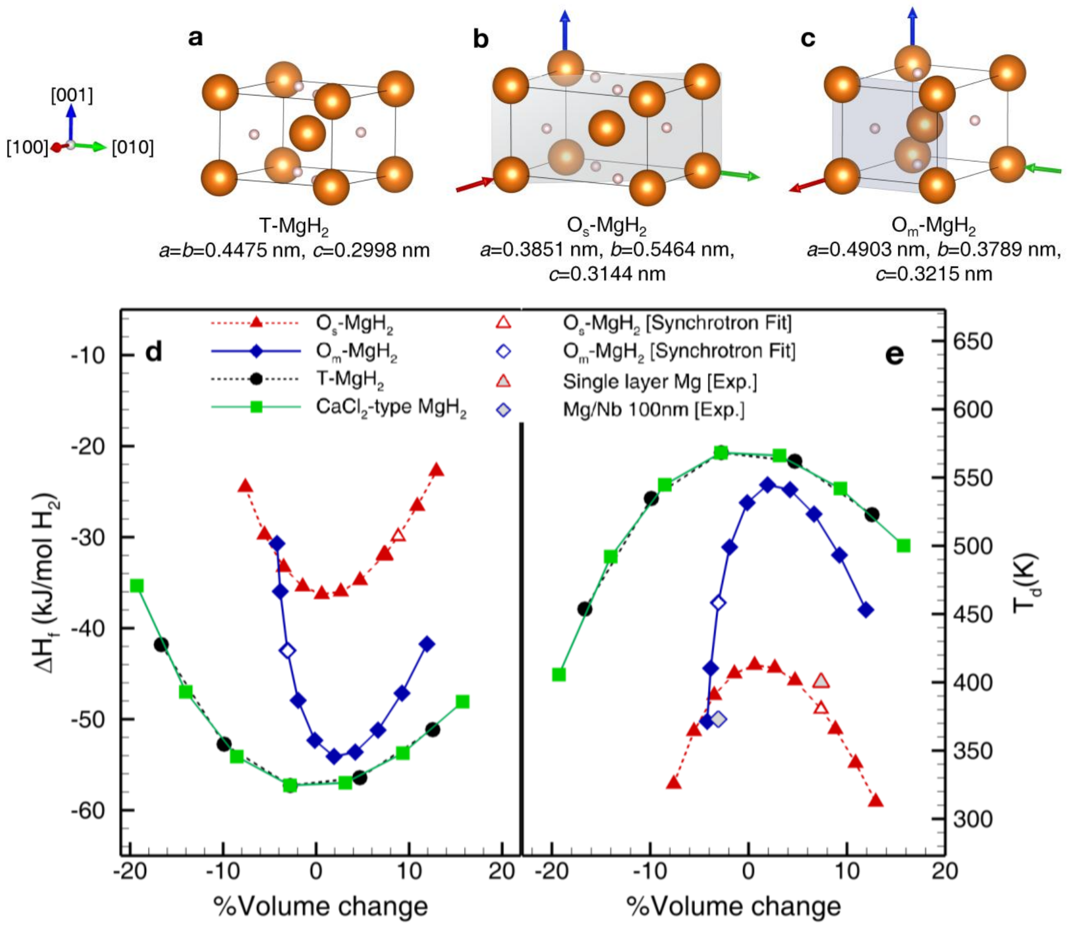

Figure 43. Crystal structures of three types of Mg hydride. (a) The rutile-type tetragonal MgH_2 (T- MgH_2) with $a = b = 0.4475$ nm and $c = 0.2998$ nm. (b) The O_s-MgH_2 structure with $a = 0.3851$ nm, $b = 0.5464$ nm and $c = 0.3144$ nm, which is consistent with the synchrotron XRD data for single layer O-MgH_2. (c) The O_m-MgH_2 structure with $a = 0.4903$ nm, $b = 0.3789$ nm, $c = 0.3215$ nm, consistent with the synchrotron XRD data. Arrows indicate the direction of distortion compared to T- MgH_2. Comparison of (d) calculated ΔH_f and (e) estimated T_d as a function of volume change in O_s-MgH_2, O_m-MgH_2, and T-MgH_2 and $CaCl_2$-type of O-MgH_2 (both systems were subjected to isotropic volume change). Experimental values of T_d are shown as open symbols. Volume changes lead to significant destabilization of MgH_2.

Density function theory (DFT) calculations were performed at 0 K for three types of Mg hydride (Figure 43a-c): T-MgH_2, O_s-MgH_2, and O_m-MgH_2. The bulk T-MgH_2 has lattice parameters of a = b = 0.4475 nm and c = 0.2998 nm (V = 0.0600 nm^3), and space group of P_{42}/mnm. The O_s-MgH_2 has the $CaCl_2$-type structure: a = 0.3851 nm, b = 0.5464 nm and c = 0.3144 nm (V = 0.0331 nm^3/f.u.) and space group of Pnnm. In comparison, the O_m-MgH_2 also has the $CaCl_2$-type of structure but with different lattice parameters: a = 0.4903 nm, b = 0.3789 nm and c = 0.3215 nm (V = 0.0299 nm^3/f.u.). The arrows in Figure 43b-c indicate the direction of distortion comparing to bulk T-MgH_2. To match with experimentally determined d-spacing, a volume expansion of ~ 7% must be imposed on O_s-MgH_2, and similarly a volume contraction by ~ 3% is necessary for O_m-MgH_2. Details of calculation can be found in our published article. In Figure 43d-e, the dependence of the enthalpies of formation, $\Delta H_{f,}$ and H desorption temperature, T_d, on volume change (with respect to T-MgH_2) were compared. The T-MgH_2 and standard $CaCl_2$-type MgH_2 were subjected to isotropic volume change.

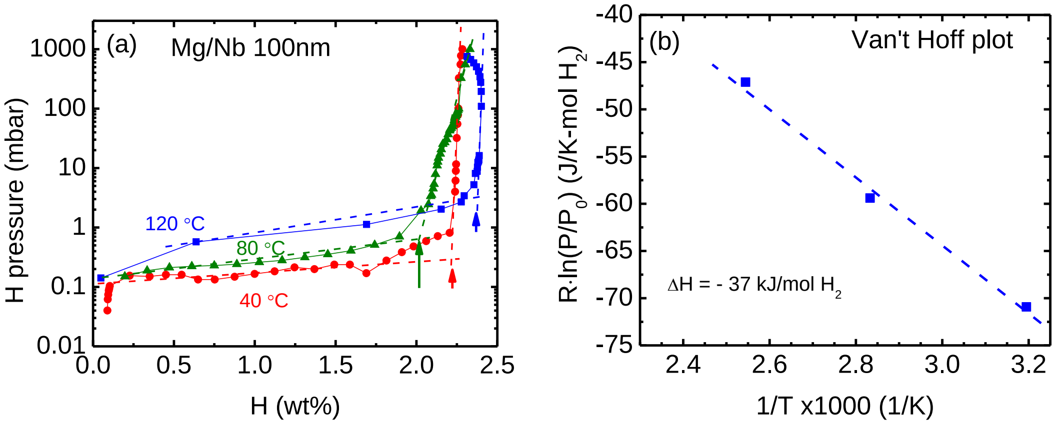

Figure 44. (a) Hydrogen absorption pressure composition isotherms of Mg/Nb 100 nm free-standing multilayer films measured at 40, 80, and 120 °C. The total film thickness is ~ 10 µm. The arrows indicate the pressured used for Van't Hoff's plot. (b) The Van't Hoff plot based on PCI plots shown in Fig. S2(a). The enthalpy is determined to be -37 kJ/mol H_2, whereas the entropy is ~ -45 J/K-mol H_2.

Figure 44a shows the hydrogen absorption measurement through pressure-composition isotherms (PCI) curves for Mg/Nb 100nm freestanding film with 10 µm total film thickness. The isotherms were measured for the first hydrogenation at 40, 80, and 120 °C. The equilibrium pressures at these three different temperatures are 0.2, 0.8, and 3.5 mbar respectively. The Van't Hoff plot is calculated in Figure 44b. The enthalpy of hydride formation is -37 kJ/mol H_2 for Mg/Nb 100nm films. This is much lower than the enthalpy for bulk Mg hydride (-77 kJ/mol H_2), implying significant destabilization of orthorhombic MgH_2. The measured value also compared well to the DFT calculated ΔH_f value (~ -30 kJ/mol H_2).

Several observations are noteworthy. (1) Volume variation (either expansion or contraction) can lead to significant reduction of T_d. (2) Under isotropic volume change, T-MgH_2 and $CaCl_2$-type MgH_2 have nearly identical temperature dependent variations of ΔH_f and T_d. (3) In O_m-MgH_2, volume contraction has significant impact on the reduction of T_d due to its most skewed volume dependence. (4) In O_s-MgH_2 subjected to ~ 7% of volume expansion, T_d is ~ 380 K, very close to that observed experimentally. (5) The calculated ΔH_f value (~ -30 kJ/mol H_2) is in good agreement with experimental measurement ΔH_f (-37 kJ/mol H_2) shown in Figure 44. The Mg/Nb multilayers show substantial thermodynamic destabilization compared to the enthalpy for bulk Mg hydride (-77 kJ/mol H_2).

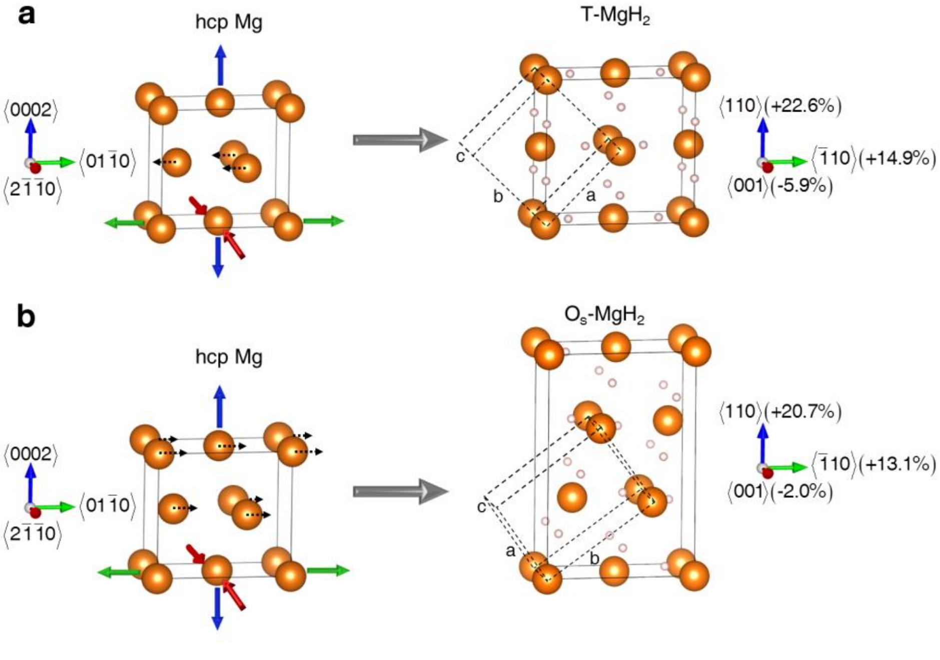

Figure 45. Three dimensional structures show the transformation of (a) hcp Mg to T-MgH_2 and (b) hcp Mg to O_s-MgH2$_2$. The orientation relationships between hcp Mg and magnesium hydrides and the magnitude of lattice distortion are also shown. The conventional unit cells with a, b and c parameters of T-MgH_2 and O_s-MgH_2 are shown as transparent boxes connected by dash lines.

Figure 45 shows three-dimensional view of the structure transformation from hcp Mg to T-MgH_2 and O_s-MgH_2, respectively. The distortion of unit cell distortion and shuffling of Mg atoms can be observed when hydrogenation occurs. The orientation relationships between hcp Mg and MgH_2 are illustrated in the same figure as well. The conventional unit cells with lattice parameters of T-MgH_2 and O_s-MgH_2 are shown as the transparent boxes. Movement of atoms was elucidated by using the centered atom on the basal plane as a reference. The illustrated transformation mechanism from hcp Mg to T-MgH_2 is similar to that proposed by B. Paik et al. [195]. It is evident that the magnitude of lattice distortion, illustrated in the same figure, is greater in T-MgH_2 than in O_s-MgH_2.

IV.5 Discussion

IV.5.1 The determination of crystal structure and lattice parameters of orthorhombic MgH_2

As mentioned earlier, extensive analyses of the interplanar spacings (from TEM and synchrotron x-ray diffraction) suggest that the symmetry of the magnesium hydride is orthorhombic in both single layer and multilayer case. Among possible magnesium hydride structures suggested in literatures [196], the distorted $CaCl_2$-type MgH_2 structure provides the closest match to experimental *d*-spacings. The comparison of predicted *d*-spacing values (by using Powder Cell [197]) with the experimental data are given in our published article (the case of O_s-MgH_2 and O_m-MgH_2).

In the case of O_s-MgH_2 in single layer films, the distorted $CaCl_2$-type MgH_2 structure with ~7% volume expansion (with respect to the volume of T-MgH_2) matched exactly with the x-ray diffraction data. The volume change compared to the T-MgH_2 was achieved by varying *c* lattice parameter only, because the lattice parameter of *a* and *b* are pre-determined by interplanar spacing of (110) and (200) planes of MgH_2 obtained from synchrotron x-ray data. The contraction of *a* and expansion of *b* and *c* compared to T-MgH_2 structure can be observed. In the case of O_m-MgH_2 in multilayers, *a* can be attained directly from the observed interplanar spacing of (200) planes. By varying volume fraction from -4.2 to 11.9% of $CaCl_2$-type MgH_2, the distorted orthorhombic structure with ~ 3% volume contraction from the T-MgH_2 has the closest match to the diffraction data. The lattice parameters of b and c for O_m-MgH_2 are determined correspondingly.

IV.5.2 Stress induced formation of metastable orthorhombic MgH_2 and its significant destabilization

The formation O-MgH_2 was induced by stress. The drastic difference in H desorption between free-standing Mg films and those on substrate highlights the significance of stress. During H loading of bulk Mg, the lattice uniformly and linearly expands with hydrogen concentration [198]. However, rigid substrate induced in-plane expansion of Mg films in an anisotropic way. This study shows (from XRD, neutron reflectivity and microscopy) that during H sorption, Mg lattice expands by ~ 25% out-of-plane. And it was postulated that there will be 6% expansion along each in-plane direction [70, 199, 200]. Our analysis shows however that the formation of T-MgH_2 with <110> texture will involve significant anisotropic in-plane distortion (Figure 45), ~ 15% in-plane expansion from Mg $<01\bar{1}0>$ to T-MgH_2 $<\bar{1}10>$, and 6% contraction from Mg $<2\bar{1}\bar{1}0>$ to T-MgH_2 <001>. Such significant in-plane distortions make it less likely to form T-MgH_2 especially when Mg films are attached to rigid substrates. The formation of O_s-MgH_2 is preferred because the magnitude of in-plane lattice distortion is much less, ~ 13% expansion and 2% contraction in each corresponding direction (Figure 45).

Stress also exists in free-standing Mg/Nb multilayers without the use of a rigid substrate. The rationale is as follows: hydrogenation leads to a 32.8% volume expansion in (from 0.0233 nm^3 for a Mg atom to 0.0308 nm^3 for MgH_2), but only 13.8% volume expansion in Nb (from 0.0180 nm^3 for Nb to 0.0205 nm^3 for NbH). As Mg and Nb remain rigidly bonded through layer interfaces (as evidenced by retention of layer integrity), such a large difference in volume expansion (~ 19%) must be accounted for by introducing significant compression in MgH_2, and thus lead to the formation of O_m-MgH_2. There were speculations that stress at the Mg-Pd interface might assist H sorption [86, 199, 200]. However Mg and Pd form several intermetallics, making it difficult to interpret the influence of stress on H sorption, and the interface is thermodynamically unstable and significantly degrades during cyclic studies. Also the usage of Pd as a major constituent in multilayers is economically prohibitive for H storage applications.

Vajeeston *et al.* [196] showed theoretically that high pressure can induce phase transformation from stable T-MgH_2 to O-MgH_2 with $CaCl_2$ prototype. Though metastable in nature, the total energy of the $CaCl_2$-type O-MgH_2 is only a few meV greater than that of T-MgH_2 as suggested by calculations and thus it is energetically feasible that the $CaCl_2$–type structure can be stabilized in thin films by stresses.

The calculated ΔH_f and estimated T_d values as a function of value change compared to the T-MgH_2 are given in supplementary Table S4. As a result of the significant distortion induced by substrate, ΔH_f for O_s-MgH_2 increased by ~ 26 kJ/mol·H_2 and T_d is reduced by ~200K compared to T- MgH_2. The desorption temperature of O_s-MgH_2 is in good agreement with the experimental observations. For O_m-MgH_2, the calculation overestimate the desorption as the role of interfacial energy on the thermodynamic stability of MgH_2 has not been considered.

IV.5.3 Implications on destabilization of MgH_2

Important implications derived from these stress analyses and DFT calculations are summarized briefly as follows. First, DFT simulations indicate that either volume expansion or contraction will lead to destabilization of MgH_2. But volume expansion and contraction may have asymmetrical impact on destabilization of MgH_2. For instance, contraction appears more effective to reduce desorption temperature of O_m-MgH_2. Volume change can presumably change the local bonding strength between Mg and H ions and thus affect the stability of MgH_2. Second, to destabilize MgH_2, stress can be introduced by selection of a second phase which has large volume expansion incompatibility compared to Mg. The magnitude of stress shall scale with the degree of mismatch between volume expansion of Mg and the second phase. A large number of candidates are available to tailor the sign and magnitude of stress in MgH_2. Third, immiscibility between Mg and the second phase may be critical to achieve structural integrity of the multilayers. Interfaces in miscible systems are typically unstable during hydrogen sorption at elevated temperatures. Immiscible interfaces are preferred to achieve high temperature thermal stability and mechanical stability against multiple cyclic loadings.

The significance of layer interface on kinetics is revealed by rapid desorption of H at room temperature in multilayers. Most of our multilayers have shown H sorption at ~ 373 K. Some of which, such as Mg/Nb 10 nm multilayers showed a desorption peak at 325 K. Layer interfaces act as high diffusivity pathways for rapid transport of H. Meanwhile, the interface may also play certain roles on destabilization of MgH_2 since a lower H desorption temperature can be achieved in Mg/Nb multilayers with smaller individual layer thickness. This phenomenon can be examined in detail with DFT calculations by considering the energetic contributions from interface and the diffusion of H in close proximity to layer interfaces.

IV.6 Conclusion

In conclusion, the drastic destabilization of Mg hydride induced by orthorhombic phase opens up abundant opportunity for the selection of appropriate second phases to design and manufacturing Mg nanocomposite with advanced H storage performance. The destabilization was triggered by the formation of distorted metastable O-MgH_2 phases induced by stresses. Stresses arise from either substrate constraint or volume expansion incompatibility. O-MgH_2 is preferred over T-MgH_2 as it induces less lattice distortion crystallographically during phase transformation. DFT calculations agree qualitatively well with experimental observations. Size effect and layer interface also play an important role to expedite the H sorption kinetics in MgH_2. These studies provide important design criteria for selection of appropriate second phase to destabilize Mg hydride. The concept of stress-assisted H-sorption developed here also has general implications for the design of other metal hydrides and chemical hydrides.

CHAPTER V

SIZE AND STRESS DEPENDENT HYDROGEN DESORPTION IN METASTABLE MG HYDRIDE FILMS

V.1 Overview

Mg is a promising light-weight material that has superior hydrogen storage capacity. However H storage in Mg typically requires high temperature, ~ 500-600K. Furthermore it has been shown that there is a peculiar film thickness effect on H sorption in Mg films, that is thinner Mg films desorb H_2 at higher temperature [70]. In this study we show that the morphology of DC magnetron sputtered Mg thin films on rigid SiO_2 substrate varied from a continuous dense morphology to porous columnar structure when they grew thicker. Sputtered Mg films absorbed H_2 at 373K and evolved into a metastable orthorhombic Mg hydride phase. Thermal desorption spectroscopy studies show that thinner dense MgH_2 films desorb H_2 at lower temperature than thicker porous MgH_2 films. Meanwhile MgH_2 pillars with greater porosity have degraded hydrogen sorption performance contradictory to our general wisdom. The influences of stress on formation of metastable MgH_2 phase and consequent reduction of H sorption temperature are discussed.

V.2 Introduction

Hydrogen is a promising alternative fuel for renewable energy applications due to its abundance, high efficiency and zero carbon emission when used in proton exchange membrane (PEM) fuel cells [1, 6]. In order to economically apply hydrogen fuels for automobile applications, light-weight hydrogen storage materials with high uptake capacity and low desorption temperature are necessary. In addition, hydrogen recycling should be performed reversibly under PEM fuel cell operating temperatures. Compared to the 700 bar gas cylinders currently used by most hydrogen vehicle manufacturers, hydrogen stored in metal hydrides offers the advantage of a much higher volumetric density [201, 202]. Among numerous hydrogen storage candidates, magnesium hydride is an attractive material because of its high H_2 storage capacity (7.6 wt. %) and economical availability as the third most abundant element on earth.

Bulk Mg hydride, however, has tetragonal phase (referred to as T-MgH_2 hereafter) that is thought to be unsuitable for automotive application because of its high formation enthalpy (ΔH = -75 kJ/mol H_2 [203]). Due to the high thermodynamic stability of Mg hydride, hydrogen absorption/desorption typically occurs at ~ 673 K in bulk Mg, much higher than practical applications (333 K–353 K) [6, 177, 178]. In order to release hydrogen at moderate temperature for PEM fuel cell applications, Mg hydride must be destabilized. Additionally hydrogen sorption kinetics must be improved to achieve practical refueling time for vehicle applications. Nanostructured materials have a large surface to volume ratio, provide more nucleation sites for hydrogen sorption, promote rapid hydrogen diffusion, and hence may lower the kinetic barriers for hydrogenation [37, 53, 184]. Recent reports showed that ball-milled nanocrystalline Mg powders can expedite hydrogen desorption process [50, 51, 204]. However, nanograins in these materials coarsen over succeeding thermal cycles and are highly susceptible to oxidation. Numerous attempts, via ball milling method, have been made to improve the kinetics of hydrogen sorption in pure Mg and Mg mixed with transition metals, with limited reduction on hydrogen sorption temperatures [53, 54, 205]. Vajo et al reported thermodynamic destabilization in more complex hydrides of Mg alloys. [63-65, 206].

Besides bulk nanostructured Mg and its alloys, Mg based thin films are also actively studied as model systems to understand hydrogen sorption kinetics [69-73]. Among these studies, Mg-Pd is a notable thin film system with peculiar H_2 sorption properties. Pd is a noble metallic catalyst that dissociates H_2 molecules to H atoms at room temperature. It has been shown that sputtered Mg thin film with a Pd cap layer can absorb and desorb under conditions suitable for PEM fuel cells (373 K, 0.1 MPa) [70]. The authors used a “cooperative phenomenon” to explain low temperature H_2 sorption in Mg/Pd multilayer films. Basically the absorption of H_2 in Pd (catalyst) leads to tensile stress in Mg and thus facilitates the hydrogenation of Mg film. During desorption, the opposite process occurs, that is desorption of H_2 from Pd leads to compressive stress that enables rapid removal of H_2 from Mg hydride [70]. If interfacial stress indeed plays a critical role on H sorption as stated in the “cooperative phenomenon”, then one would anticipate that thinner films desorb H_2 at a lower temperature as such a mechanism implies lower H_2 sorption temperature in thinner films. However it was reported that thicker Mg films desorbed H_2 at lower temperature. Pd-decorated Mg blades prepared by oblique angle thermal deposition also have shown a low H desorption temperature, ~ 373 K [91].

Other than noble metal catalyst (such as Pd), transition metal catalysts were added to Mg films to expedite H_2 sorption kinetics in T-MgH_2 [75-81]. Furthermore certain transition metal catalysts incorporated by co-sputtering with Mg have led to reduction of the hydrogen formation energy [82-85]. Co-sputtered Mg-Ti thin film showed cyclic capability, but hydrogen formation energy is unknown [84-86]. Mg-Ni-Ti ternary thin film exhibited hydride formation energy of -40 kJ/mol H_2 [88, 89]. Co-sputtered Mg-25 at.% Nb thin film showed the formation of a meta-stable bcc alloy with the hydride formation enthalpy of -52 kJ/mole H_2 [87]. However, the hydrided Mg-Nb film desorbed hydrogen only at 448 K and deterioration of the Mg and Nb (a gradual segregation) was observed after extended cycling studies. We have recently reported that H_2 sorption in 1.6 µm Mg film grown on rigid SiO_2 substrate and free standing Mg/Nb multilayers led to the formation of a metastable orthorhombic MgH_2 (O-MgH_2) phase, which has an ultra-low hydride formation energy, - 37 kJ/mol H_2 [207], compared to -75 kJ/mol H_2 of stable T-MgH_2. Thus O-MgH_2 desorbs H_2 at ~ 373K or lower. These experimental results compared well with those obtained by first principle calculations [207]. In parallel TEM studies have shown that bcc metastable Mg formed on top of Nb [208] and DFT calculations were performed to gain insight on the stabilization of such a metastable bcc Mg phase [209]. The potential tie between bcc Mg and the formation of O-MgH_2 requires further investigations.

In this paper we show that thinner Mg films indeed desorb H_2 at lower temperature than thicker films. Film thickness has a direct influence on porosity of Mg films, namely thinner film (~ 200 nm) formed a continuous dense layer, beyond which it evolved into a porous columnar structure. Mg pillars with different porosity also have drastically different H_2 sorption performance. Contradictory to our intuitive anticipation, greater porosity degrade H_2 sorption performance of Mg pillars. The evolution of stress during H_2 sorption and stress-induced formation of O-MgH_2 play major roles on hydrogen sorption properties of Mg films. This study provides an important step forward towards in-depth understanding of destabilization of Mg hydride via stress-driven formation of metastable phases.

V.3 Experimental

Mg films with layer thickness *t* varying from 200 to 1600 nm were deposited by DC magnetron sputtering on oxidized Si (100) substrates with 1 μm thermal oxide layer at room temperature. All Mg films were protected by 25 nm Pd cap layer, which catalyzes the dissociation of hydrogen molecules and protect Mg films from oxidation. Mg and Pd targets with 99.99% purity were used for magnetron sputtering. The base pressure of the chamber was better than 6.6×10^{-6} Pa prior to deposition. The films were grown under ~ 0.8 mTorr Argon pressure with 99.999% purity. The deposition rates for Mg and Pd were ~2 and 0.3 nm/s, respectively. To fabricate Mg nanopillars, Si wafers were mounted on a custom-designed substrate holder at an angles of 5^o relative to the direction of the sputtering source (i.e. using a configuration of glancing angle deposition). During glancing angle deposition, the substrate was not rotated. In parallel, inclined deposition at 45^o was also performed without substrate rotation. After deposition, samples were transported directly into an attached high vacuum chamber for hydrogen absorption and desorption studies. The base pressure of hydrogen chamber was ~ 5×10^{-7} Torr before hydrogen loading. All Mg films were hydrided at a pressure of 0.25 MPa with ultra high purity gas mixture (96%Ar + 4% H_2) at 373 K for 24 hours. Hydrogen desorption studies were performed by thermal desorption spectroscopy (TDS) technique enabled by a quadruple mass spectrometer in a residual gas analyzer (RGA). During desorption studies, Mg specimens were heated from room temperature up to a maximum of 623 K at a constant heating rate of 4 K/min. X-ray diffraction (XRD) experiment was performed on a Bruker-AXS D8 Bragg–Brentano X-ray diffractometer. Morphology and structure of as-deposited and hydrided films were examined by scanning electron microscopy (SEM) using a JEOL JSM-7500 field emission scanning electron microscope operated at 5 kV.

V.4 Results

The XRD plots of Mg films in Figure 46a show that all Mg films exhibit (0002) texture and the peak intensity increases proportionally as the layer thickness increases. Figure 46b shows XRD profiles of Mg films on rigid Si substrate after hydrogen loading (373 K/ 24 h). Most of the as-deposited Mg films transformed to orthorhombic Mg hydride (referred to as the "O-MgH_2" thereafter) similar to $CaCl_2$ with a (110) texture. Detailed crystal structure analysis for O-MgH_2 can be found elsewhere [207].

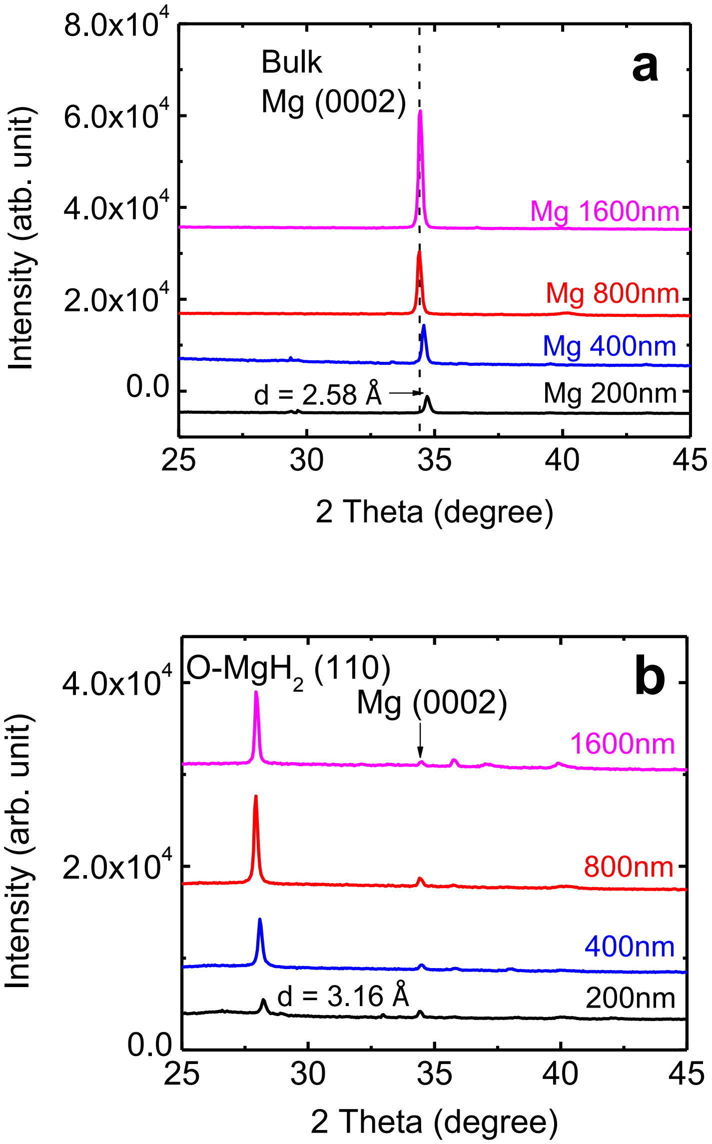

Figure 46. X-ray diffraction (XRD) patterns of Mg films of different thickness (t = 200 - 1600 nm with a 25 nm thick Pd cap layer) before and after hydrogen loading at 373 K for 24 hours. (a) All as-deposited Mg films had (0002) texture and its peak intensity increased with increasing t. A slightly reduced d-spacing of Mg (0002) was observed in thinner Mg film (t = 200 nm) compared to that of bulk Mg. (b) After hydrogen loading the intensity of Mg hcp (0002) peaks diminished significantly. Meanwhile orthorhombic MgH_2 (O-MgH_2) (110) peak emerged with stronger texture in thicker MgH_2 films.

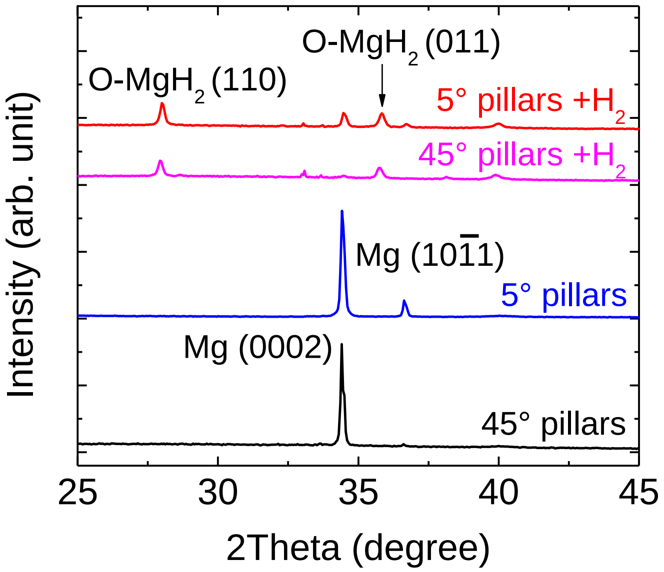

Figure 47. XRD pattern of 5 µm thick Mg pillars obtained with different inclined deposition angle (5°, 45°) before and after hydrogen loading. Both as-deposited Mg pillars showed highly (0002) textured Mg peak and Mg pillars deposited with 5° glancing angle (referred to as Mg 5° pillars) showed Mg $(10\bar{1}1)$ position. After hydrogen loading at 373K / 24h, Mg 45° pillars were fully hydrided by forming O-MgH$_2$ structure. Mg 5° pillars showed both Mg hydride peaks and hcp-Mg peak, implying incomplete hydrogen loading in the pillars.

Figure 47 shows XRD patterns of 5µm tall Mg pillars (morphology will be shown later) deposited at different angles (5°, 45°) before and after hydrogen loading. Both as-deposited Mg pillars showed highly textured (0002) orientation, while Mg pillars with 5° deposition angle (referred to as “5° pillar film” hereafter) also had a $(10\bar{1}1)$ secondary peak. After hydrogen loading (373 K/24 h), the 45° pillar film was fully hydrided and transformed to O-MgH$_2$, while the 5° pillar film had both Mg hydride peaks and hcp- Mg (0002) peak.

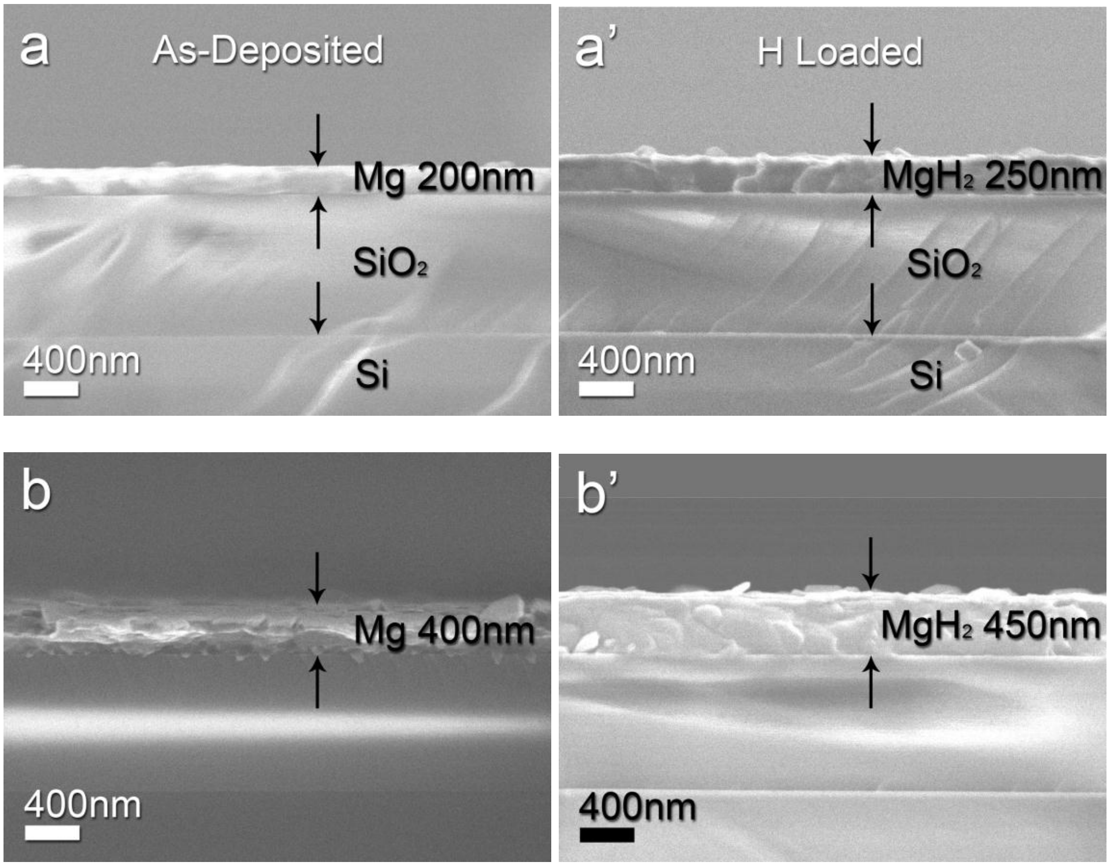

Figure 48. Cross-sectional SEM micrographs of Mg pillars before (a-e) and after hydrogen loading (a'-e'). (a) Mg 200 nm film had dense structure with continuous and smooth surface. (b) Mg 400 nm film started to show a porous structure as films grew thicker. (c) Mg 800 nm showed porous columnar structure with a dense 200 nm thick layer on the substrate. (d-e) show Mg pillars produced by glancing angle deposition. 45° pillars film shows columns grown toward to the sputter plasma. 5° pillars film shows extremely porous structure. After hydrogen loading, all MgH$_2$ films (a'-c') showed substantial thickness increase and pores were filled up due to volume expansion. (d') After hydrogen loading Mg 45° pillars film reveals dense structure. (e') Mg 5° pillars films remain in pillar morphology after H loading.

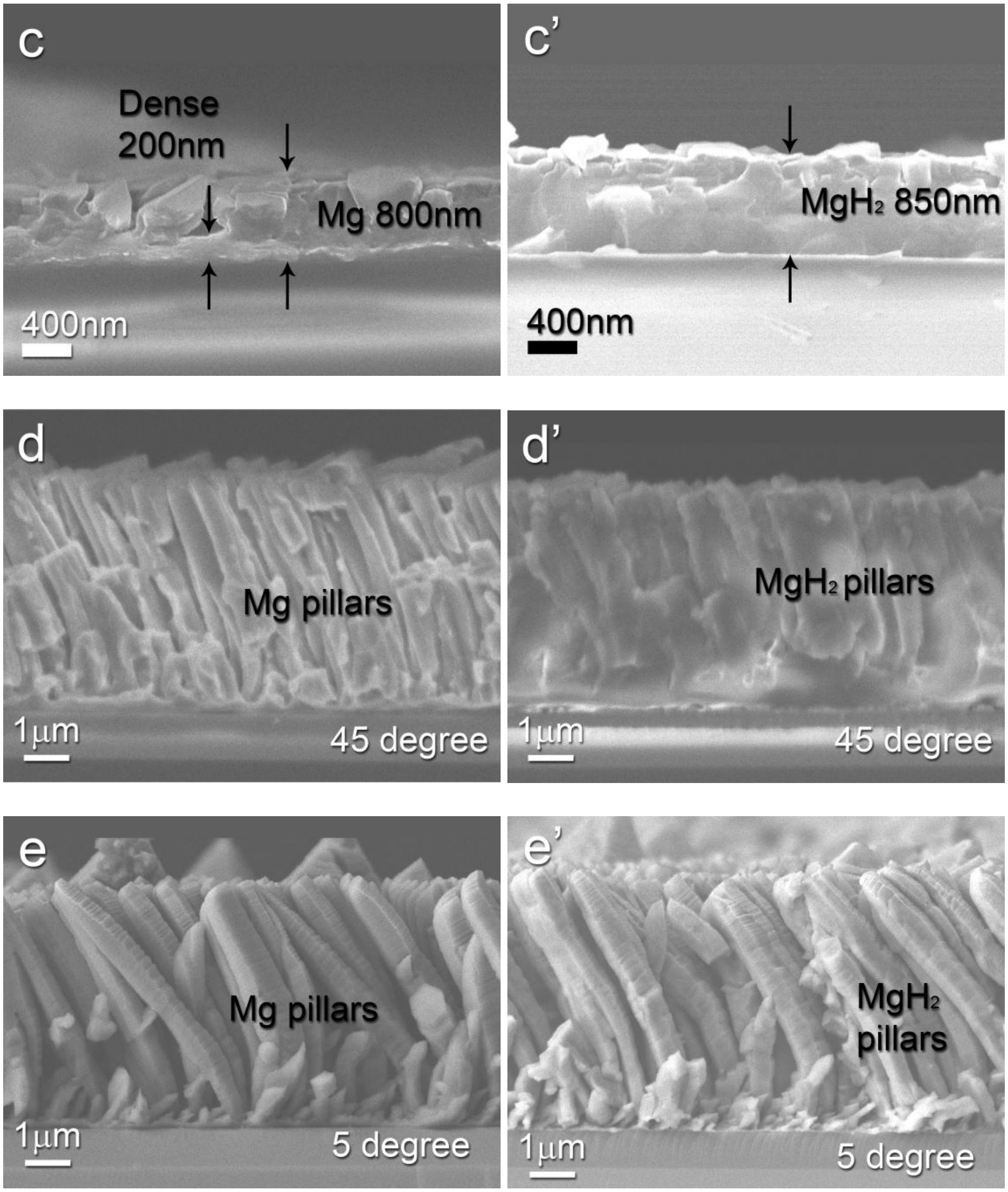

Figure 48. Continued.

Cross-section scanning electron microscopy (XSEM) micrographs in Figure 48a-e show the evolution of film morphology of various Mg films. All films were sputtered on Si substrates with thermally grown Si oxide layers. 200 nm thick Mg film (Figure 48a) had fully dense, continuous structure and the plan-view SEM micrograph of the film (not shown here) shows a featureless, shiny surface. However, when film thickness (*t*) is greater than 200 nm, surface roughness and porosity appeared (Figure 48b). Figure 48c reveals an initial ~ 200 nm dense layer on substrate followed by porous structure thereafter in thick Mg film (*t* = 800 nm). Figure 48d shows that the 45° and 5° Mg pillar films were both porous and the 5° pillar film had extremely high porosity and dispersed columnar structures. The columnar diameters are similar in both pillar films.

XSEM micrographs of all corresponding hydrogen-loaded Mg samples are shown in Figure 48a’-e’. Mg hydride films were substantially thicker than as-deposited parent films. For instance the hydride film thickness increased to 250 and 450 nm (Figure 48a’ and b') compared to 200 and 400 nm thick parent films (Figure 48a and b). The porous 800 nm thick Mg films became nearly fully dense (Figure 48c’), but the thickness increased moderately to merely 850 nm. Compared to the as-deposited 45° pillar film, the hydrided pillar film in Figure 48d’ appeared much denser. On the other hand, the morphology of hydrided 5° pillars film (Figure 48e’) had little variation in porosity compared to the as-deposited films.

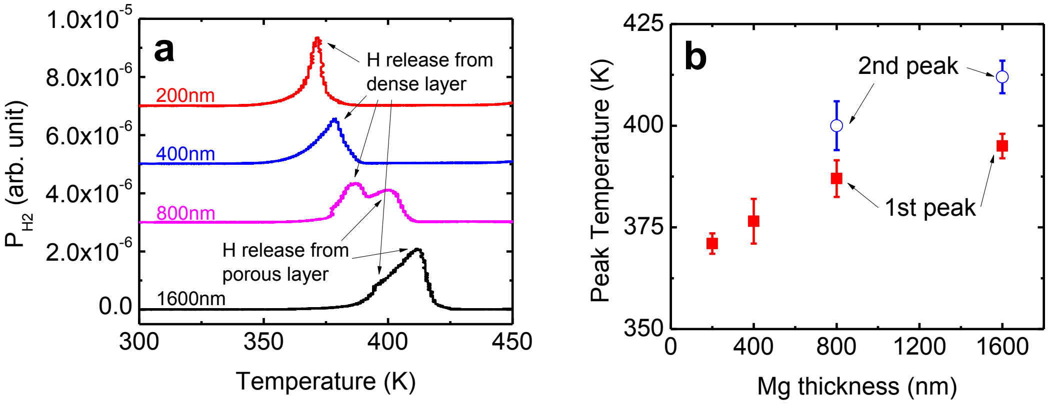

Figure 49. (a) Thermal desorption spectra (TDS) of Mg hydride films show the evolution of hydrogen pressure during desorption of hydride films with different film thickness. A thinner (200 nm for Mg, and 250 nm after hydrogen loading) Mg hydride film desorbed hydrogen at 373 K and showed only one prominent desorption peak, while thicker specimen desorbed hydrogen at higher temperature with two detectable peaks. (b) The H desorption temperature for the first peak decreased with decreasing Mg film thickness.

Figure 49a compares the TDS spectra of hydrogen for hydrogenated Mg films with various film thicknesses. In the 800 and 1600 nm Mg hydride films, the TDS spectra appear to be consisted of two peaks. The lower temperature peak shows comparable intensity to the high temperature peak in the TDS spectrum of hydrided Mg 800 nm film. In the 1600nm Mg film, however, the high temperature peak, ~ 410K, has much greater peak intensity than the low temperature peak, ~ 395 K. At smaller layer thickness, *t* = 200 and 400 nm, only one H_2 desorption peak was observed. The hydrogen desorption peak temperature gradually shifted to lower temperatures as *t* decreased. For instance, the hydrided Mg 200 nm film reached a peak temperature at ~ 370 K. Peak desorption temperatures of all Mg films are summarized in Figure 49b. Evidently the hydrogen desorption peak temperature decreased rapidly with decreasing Mg layer thickness.

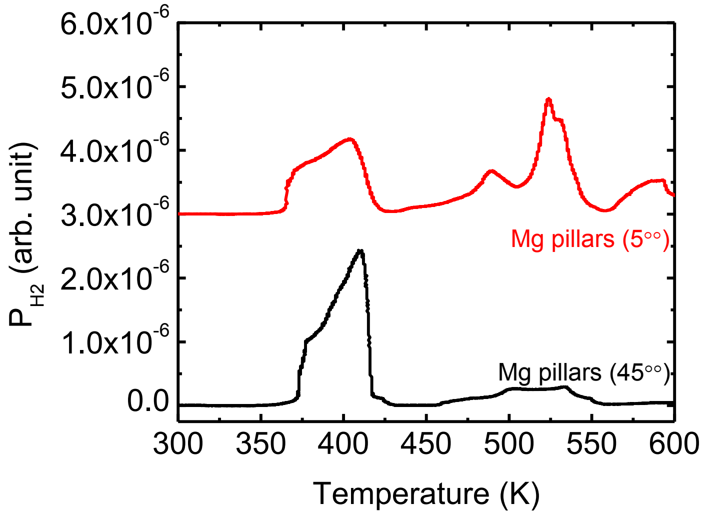

Figure 50. TDS of hydrided (373K/24h) Mg 5° and 45° pillars films. In Mg 45° pillar films, most hydrogen was desorbed during the first intense peak. Mg 5° pillars film shows several additional desorption peaks at higher temperatures.

Figure 50 compares TDS spectra for H_2 loaded 45° and 5° pillar films. Both specimens have two groups of desorption peaks. The low temperature group in both specimens started hydrogen desorption at ~363 K and exhibited peak desorption at ~ 410 K. In the 45° pillar films, the intensity of the first (low temperature) group of peaks is much greater than that of the second (higher temperature) group. Whereas in the hydrided 5° pillar film, the intensity of the second group of peaks (consisting of multiple peaks) is at least comparable to that of the first group of peaks.

V.5 Discussion

V.5.1 The formation of O-MgH_2 as a consequence of stress

We recently reported the formation of orthorhombic Mg hydride (O-MgH_2) in hydrided Mg films on rigid substrate and in Mg/Nb multilayers [207]. This is surprising as bulk O-MgH_2 has been observed only under high pressure, several GPa [40, 196]. The formation of O-MgH_2 in single layer Mg deposited on rigid substrate is a consequence of stress induced by substrate constraint. The Mg lattice in the film expands during hydrogen loading. However, it is forced to expand in primarily the out-of-plane direction since in-plane lattice expansion is largely prohibited by the rigid Si substrate (which barely absorbs H_2). Thus the large stress arising from rigid substrate leads to the formation of O-MgH_2 [207].

In Figure 51, the structure transformations from hexagonal close packed (hcp) Mg to Mg hydrides are compared from three- and two dimensional view. Mg with hcp structure is shown in Figure 51a. Figure 51b presents the conventional unit cell of stable T-MgH_2 with $a = b = 4.475$ Å and $c = 2.998$ Å. Figure 51c is the unit cell of O-MgH_2 observed in this study with $a = 3.851$ Å, $b = 5.464$ Å and $c = 3.144$ Å. Details on measurement of lattice parameters via *in situ* x-ray diffraction technique at advanced photon source – Argonne National Laboratory can be found elsewhere [207]. Comparison of Mg and its hydrides has been illustrated in two dimensional projected view in Figure 51d-f. The blue plane in Figure 51d corresponds to a $\{2\bar{1}\bar{1}0\}$ plane shown in Figure 51a. Lattice distortion and atomic shuffling occurs when hcp Mg absorbs hydrogen to form Mg hydrides. During the formation of T-MgH_2 (Figure 51e), the <0002> and $<01\bar{1}0>$ directions of hcp Mg expand and transform to <110> and $<\bar{1}10>$ of T-MgH_2 respectively. While contraction occurs in $<2\bar{1}\bar{1}0>$ direction in Mg, and this direction transforms to <001> direction of T-MgH_2 after hydrogen loading. In contrast during the formation of O-MgH_2 in this study, the <0002>, $<01\bar{1}0>$, and $<2\bar{1}\bar{1}0>$ directions of hcp Mg evolve to <210>, $<\bar{2}10>$ and <001> of O-MgH_2, respectively as shown in Figure 51f. The difference in magnitude of distortion along certain characteristic orientations during the formation of both types of hydrides has been labeled in Figure 51e and f.

In Mg/Nb multilayers, a different type of O-MgH_2 (a = 4,903 Å, b = 3,789 Å and c = 3.215 Å) was identified [207]. In absence of rigid substrate (free standing multilayers), a large stress arises in multilayers due to volume expansion incompatibility between Mg hydride and Nb hydride. During the formation of Mg hydride there is a volume expansion of 32.8%. In contrast only 13.8% of volume expansion occurs during the formation of NbH.

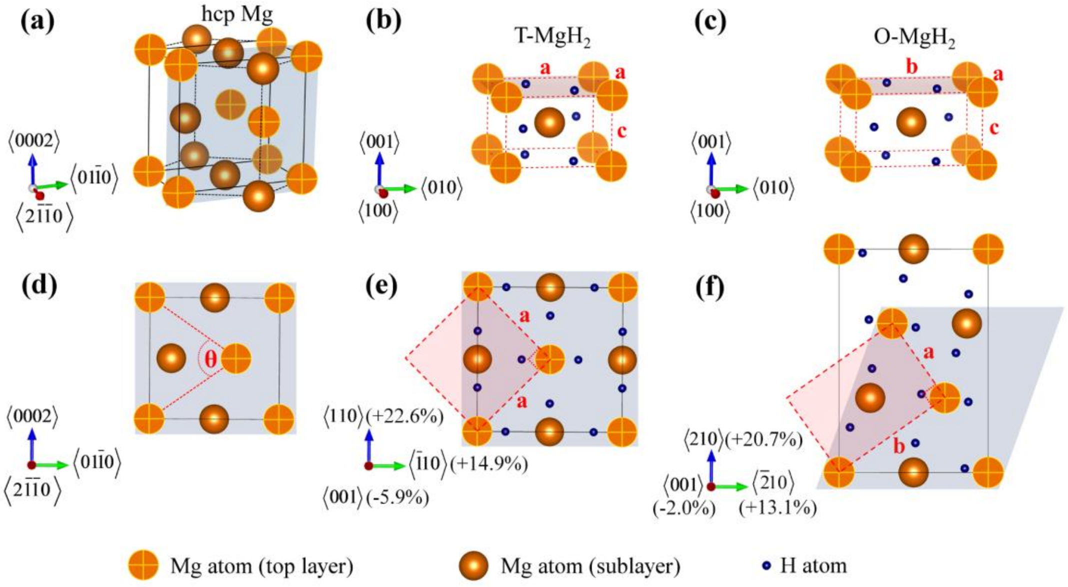

Figure 51. Three dimensional structures of (a) hcp Mg, (b) T-MgH_2 and (c) O-MgH_2. Comparison of two dimensional views projected on (d) a $(2\bar{1}\bar{1}0)$ plane of hcp Mg (e) a (001) plane of T-MgH_2 and (f) a (001) plane of O-MgH_2. The transparent blue planes are represented the corresponding plane projected on a $(2\bar{1}\bar{1}0)$ plane of hcp Mg. The transparent red planes are represented the projected (001) plane in the conventional unit cells of T-MgH_2 and O-MgH_2. The angle θ changes from 70.2º to 90º when hcp Mg transforms to Mg hydrides.

Since Mg, Nb and their hydrides are rigidly bonded through layer interfaces (as reflected from reversible microstructure change and retention of layer interfaces during hydrogenation [207]), such a large volume expansion disparity during hydrogenation of Mg and Nb in multilayers results in large stress, and consequently the formation of O-MgH_2. Synchrotron XRD experiments confirmed the formation of this metastable phase. It shall be noted that stress arising from phase transformation is different from residual growth stress. The evolution of residual growth stress with film thickness is shown in

Figure 52. Tensile residual stress (with a maximum of 50 MPa) decreases rapidly with increasing film thickness. Hydrided films have a similar thickness dependent variation of residual growth stress at slightly greater magnitude. The stress induced O-MgH_2 is very unstable and can desorb hydrogen at low temperature (< 373K) as confirmed by first principle calculations [207].

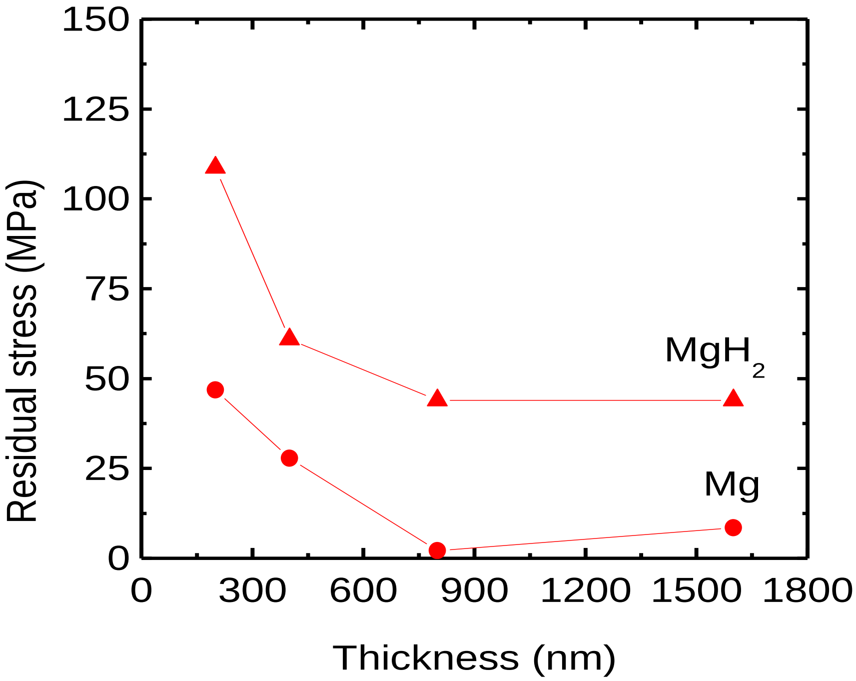

Figure 52. Residual stress of Mg and MgH_2 films as a function of layer thickness. Both Mg and MgH_2 films show high tensile stress at smaller layer thickness and lower values when films grew thicker.

V.5.2 Thickness dependent evolution of film morphology

Figure 53 shows the evolution of percentage of thickness increase *Δt/t* (after hydrogenation) with the initial thickness (t_o) of Mg films. The horizontal dash line indicates the expected thickness increase after hydrogen loading, ~ 21% due to variation of lattice parameters (shown in Figure 51f) from Mg to O-MgH_2. After hydrogen loading, Mg 200 nm expanded by 25% along the plane normal direction, slightly exceeding the predicted value. However, the value of $\Delta t/t_o$ decreased rapidly, with increasing Mg film thickness, down to ~ 5% in Mg 1600 nm films. This somewhat surprising result (large deviation from expected values) is reconciled when examining the evolution of microstructure during hydrogenation.

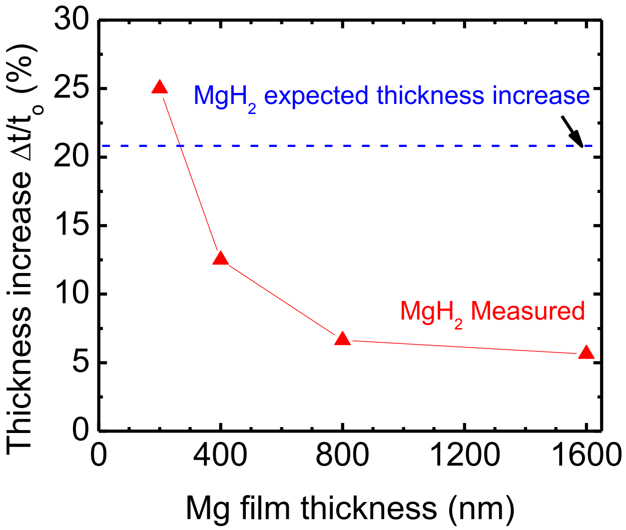

Figure 53. The film thickness of Mg films before and after hydrogen loading. Mg 200nm film shows 25 % expansion in out-of-plane direction. As film thickness increases, MgH_2 film thickness expansion decreases. The estimated values were calculated assuming fully dense Mg films.

XSEM studies show that the morphology of Mg films evolves with their thickness, namely thinner films (when $t \leq 200$ nm) are fully dense, whereas porosity increases significantly in thicker films. As shown schematically in Figure 54, hydrogenation of fully dense films ($t = 200$ nm) leads to significant increase of film thickness to accommodate the volume expansion during formation of Mg hydrides. However, during hydriding of thicker porous Mg films, there is sufficient free space to accommodate volume expansion by filling up porous films. Hence the evolution of film thickness in porous Mg is much less dramatic than that in dense thin Mg films.

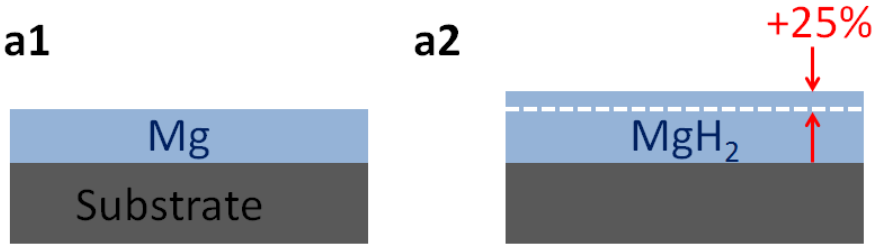

Figure 54. Schematics illustrating the impact of stress and porosity on destabilization of Mg hydride. (a) Mg 200 nm film exhibits dense structure in both as-deposited and hydrogen loaded states and film expanded 25% along the out-of-plane direction. (b) Porous thick Mg film (800 nm) had columnar structures with a thin initial dense layer. After hydrogen loading, pores in the film were filled up and the film shows only 6-7% thickness increase.

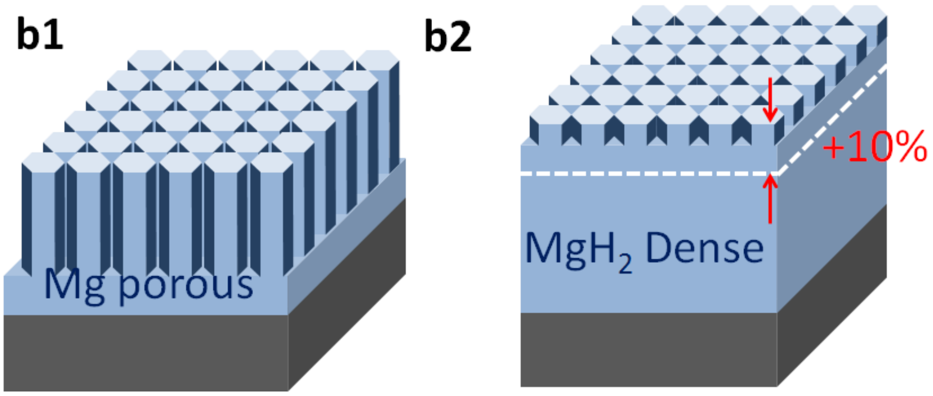

Figure 54. Continued.

V.5.3 Size dependent variation of desorption temperature

The TDS spectra revealed size (film thickness) dependence on the hydrogen desorption temperature, that is, thinner Mg films desorb hydrogen at lower temperature than thicker films. In addition, double desorption peaks were observed in thicker (porous) Mg films (t > 400 nm). In Mg 800 nm films, the first peak at ~386 K may arise from the underlying dense Mg layer. The other desorption peak at higher temperature, ~ 400K, could be due to the formation of porous upper layer. More specifically, the lattice expansion of Mg during hydrogenation is more confined in the dense section of films close to the substrate. A large stress during hydrogenation should lead to the formation of O-MgH_2, which desorbs hydrogen first due to its metastable characteristics. The magnitude of lattice distortion of O-MgH_2 is less significant in thicker Mg films as porosity provides fertile open volume to accommodate hydrogenation induced lattice expansion. Correspondingly the magnitude of stress during hydrogen loading is much lower, and consequently the thermal stability of distorted Mg hydride improves. The clear reduction of $\Delta t/t_o$ with Mg film thickness in Figure 53suggests the same conclusion: that is thicker porous films desorb hydrogen at higher temperature due to the lack of lattice constraint. Our previous pressure-composition isothermal (PCI) measurement shows that the formation enthalpy of O-MgH_2 is ~ -37 kJ/mol. H_2 [207], much less than ~ -75 kJ/mol. H_2 for T-MgH_2, and hence hydrogen desorption in O-MgH_2 occurs at a much lower temperature, ~ 400K or less, than that in stable T-MgH_2, ~ 673K. The drastic destabilization of Mg hydride due to stress induced O-MgH_2 is thus an appealing approach to achieve low operation temperature in this light weight metal hydride for vehicle applications.

V.5.4 The discrepancy on size effect with previous study on Mg/Pd system.

Our results are notably different from the work reported by Fujii et al. who performed study on a similar Mg/Pd system [70]. In the previous study, Fujii et al showed that for a Pd50nm/Mg/Pd50nm trilayer system, the hydrogen desorption peak temperature decreases with increasing Mg film thickness from 385 K (t_{Mg} = 200nm) to 350K (t_{Mg} = 800nm). Although cooperative phenomenon has been proposed to explain remarkable hydrogen sorption performance in Mg/Pd system, this model does not explain their reverse size dependent variation of desorption temperature. The differences between these two studies could be understood from several perspectives. First, we notice that their Mg films were sandwiched between two Pd layers, a cap and a buffer layer right on top of substrate. While having Pd on both ends might accelerate H_2 desorption, the usage of Pd as a buffer layer could also bring some challenge. The poor adhesion between Pd and glass substrate could lead to delamination of hydrided trilayer films (or a stress-free Mg film) [70], and thus lose the advantage of constraint (stress) from rigid substrate. Second, Pd has lower elastic modulus, ~ 117 GPa [210], compared to an biaxial elastic modulus of 180 GPa [210] for Si (100) substrate. Hence there is consistently greater influence (constraint) arising from Si substrate in our study. Third, there is difference in morphology of as-deposited Mg films. Fujii et al. obtained dense and continuous films prepared by RF assisted deposition, while we generated a porous structure when $t > 200$ nm.

V.5.5 Proof of stress concept by using Mg nanopillars

The general perception is that Mg films with larger surface areas should have better H_2 sorption behavior. Hence porous Mg pillars may have improved performance over continuous Mg films. However our studies revealed the opposite phenomenon. Hydrogen sorption performance of the Mg pillars can also be explained by porosity and stress effect. The XRD studies in Figure 47 show that the 45° pillar film was fully hydrided to O-MgH_2 phase while the 5° pillar film was not, as indicated by the residual hcp-Mg peak. The highly porous and dispersed columnar structure in the 5° pillar film prevents the introduction of large stress from rigid substrate. The TDS spectrum in Figure 50 illustrates how porosity in pillars may impact hydrogen desorption kinetics. The 45° pillars film has a prominent low temperature desorption peak at ~408 K, and a weak, broad high temperature peak, spreading from 474 to 573 K. The low temperature desorption peak arises from dense Mg hydride layer adjacent to substrate, whereas the high temperature peak arises from H desorption from less dense Mg hydride (subjected to less stress effect). Most hydrogen was however desorbed by ~425 K in the 45° pillar films. In contrast, in the 5° pillar film, the high temperature H_2 sorption peak ranging from 490 to 540 K dominated the desorption process, as the impact of stress is significantly reduced due to a much greater porosity in these highly porously pillar films. Thus the pillar studies confirm the idea that constraint (stress) from rigid substrate is critical to achieve O-MgH_2 with superior H_2 sorption performance in Mg.

V.6 Conclusions

We explored the hydrogen storage performance of porous and dense Mg films prepared by magnetron sputtering under various conditions. Thinner dense Mg films (t = 200 nm) have lower hydrogen desorption temperature than their thicker porous counterparts film (t > 200 nm). Mg 45° pillar film also shows improved hydrogen sorption performance than the more porous 5° pillar films. Stress arising from rigid substrate during hydrogenation of Mg films plays a critical role to induce metastable orthorhombic Mg hydride that can easily desorb H_2 at low temperatures. The stress concept validated via numerous experiments could have general implications on destabilization of other types of metal hydrides for H_2 storage application.

CHAPTER VI

FABRICATION OF POROUS AND PILLAR-SHAPED MG BY MAGNETRON SPUTTERING

VI.1 Overview

We report on the synthesis of nanostructured Mg platelets with nanopores and Mg pillars by magnetron sputtering techniques under different deposition conditions. By varying deposition parameters, the morphology of Mg may vary from fully dense epitaxial film to polycrystalline nanoporous structures comprised of hexagonal plates. The influence of layer thickness, deposition rate, incidence angle and mode of deposition (DC vs. RF sputtering) on morphology of Mg was interrogated. Additionally forest of Mg nanopillars formed via glancing angle deposition technique.

VI.2 Introduction

Mg is a promising material for solid-state hydrogen storage as it absorbs a high weight percentage of hydrogen (exceeding 7 wt.%) in form of Mg hydride. Furthermore porous and nanopillar Mg may have enlarged surface areas and hence promote the kinetics of H sorption in Mg. Nanoporous Mg and Mg nanopillars may also have potential applications as biological implant to enhance the healing of bones. In the following section, we will briefly summarize the Mg nanostructures that have been fabricated to date.

Mg nanoblades have been synthesized by glancing angle deposition technique [211]. Meanwhile thermal evaporation has produced Mg nanowires [212] and nanoprism [213].

The formation mechanisms for these nanofeatures are not clear, and the diameter of Mg nanowires spans across tens to hundreds of nanometers with a large diversity in length and morphology of wires.

Nanoporous Mg has not been successfully fabricated to date. A popular technique to fabricate nanoporous precious metal films, such as Au, is chemical dissolution of (leaching) less noble elements, such as Ag from Au-Ag alloys [214-221]. The size of nanopores can approach tens of nm with good uniformity. This technique, however, is not applicable for the synthesis of nanoporous Mg, due to its significant chemical reactivity.

Magnetron sputtering is known to be a versatile technique to produce high quality films. At higher deposition rate, the density of sputtered films is typically higher than evaporated films, and a more compressive stress often develops [222]. Factors such as deposition rate, kinetic energy of incoming adatoms and the incident angle may dramatically alter the microstructure of sputtered films. For instance studies comparing RF and DC magnetron sputtering on ZnO:Al [223], alumina [224], SiCN [225], and Al-doped ZnO [226] show that RF and pulsed magnetron sputtering led to much higher hardness than DC sputtered coatings due to continuous and dense surface with small grains.

In this work, a systematic study has been conducted to explore the effects of numerous parameters, including layer thickness, DC and RF sputtering, deposition rate, texture of single crystal substrates, and varying deposition angles, on morphology of Mg films. By altering these deposition parameters, the film morphology varied from epitaxial dense films to films of varying porosity, and nanoscale pillars. Detailed microstructural characterizations and film stress measurements were conducted to examine the surface morphology and film growth mechanism. DFT calculations were performed to understand the drastic difference between morphology of DC and RF sputtered Mg films.

VI.3 Experimental

Mg single layer films were deposited by DC and RF magnetron sputtering from high purity (99.99%) Mg targets. Mg films with layer thickness varying from 100-800 nm were deposited onto oxidized Si substrates with 1μm thick amorphous SiO_2. Single crystal Si (111) substrates etched with hydrofluoric acid were also used for deposition. The chamber was evacuated to a base pressure of at least 6.6×10^{-6} Pa prior to deposition. For DC sputtering the deposition rate varied from 0.6 to 2.4 nm/s and Ar pressures of 0.08, 0.33, and 0.57 Pa were used. RF sputtering rate was ~1.6 nm/s under ~0.33 Pa Ar pressure. To fabricate Mg pillars, the substrate was tilted at 5° with respect to the central axis of sputtering gun (i.e. nearly parallel to the direction of deposition flux, see Figure 55). X-ray diffraction (XRD) experiments were performed on a Bruker-AXS D8-focus Bragg–Brentano X-ray diffractometer (Cu kα radiation). Scanning electron microscopy (SEM) was performed using JEOL JSM-7500F microscope operated at 5kV. Transmission electron microscopy (TEM) studies were carried out on a JEOL 2010 microscope operated at 200 kV. Substrate curvature was measured before and after deposition using a Dektak-150 profilometer to calculate film stress.

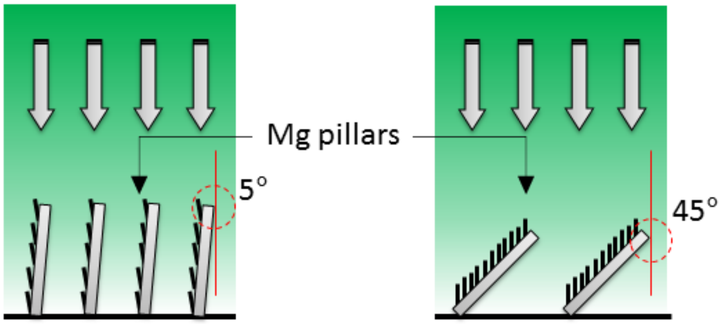

Figure 55. Schematic diagram of the inclined deposition setup. Si substrates are placed at 5° (left) and 45° (right) with respect to the incoming flux. Films deposited using this technique will be referred to as Mg 45^o and Mg 5^o thereafter.

VI.4 Results

VI.4.1 Films of varying thickness

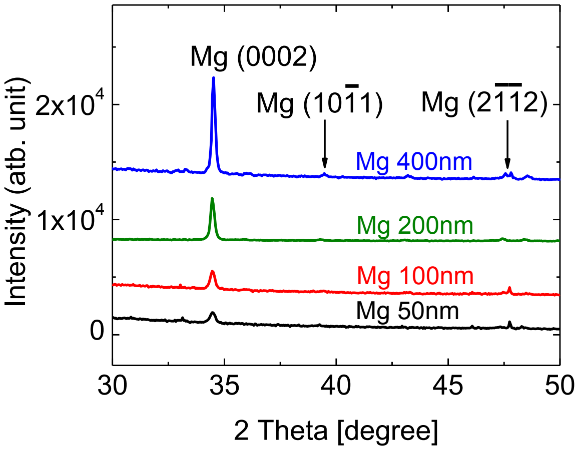

Figure 56. XRD profiles of Mg films of various thickness, 50 - 400 nm, with (0002) texture on SiO$_2$ substrate. The peak intensity increased with increasing film thickness.

Figure 56 shows XRD profiles of Mg films deposited at a rate of 2.4 nm/s under 0.33 Pa Ar pressure (referred to as the “standard condition” thereafter) with different layer thickness on oxidized Si substrates. All films are polycrystalline with (0002) texture, and the (0002) peak intensity is proportional to film thickness. Furthermore these films do not have a shiny surface, indicating the formation of rough surfaces.

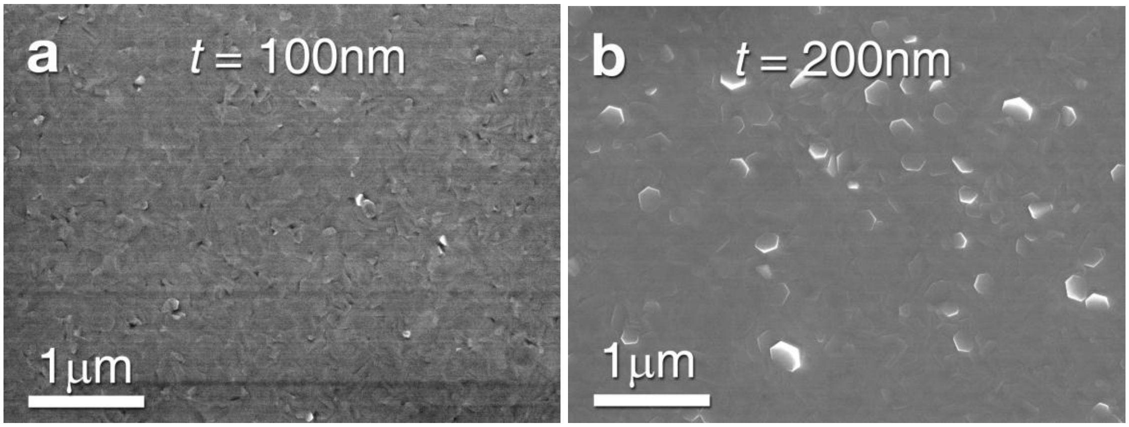

Figure 57. Plan-view SEM micrographs of DC sputtered Mg films (*t* = 100, 200, 400, 800 nm). (a) 100 nm thick specimen showed predominantly smooth surface decorated with few half hexagonal plates. (b-d) show complete hexagonal plates with greater diameters when films grew thicker (200-800nm). Mg 800 nm film showed abundant nanopores. (e) Cross-sectional SEM micrograph of Mg 800 nm film reveals the porous columnar structure. A 200 nm thick dense layer adjacent to substrate was identified. (f-h) Grain size distributions of various Mg films show that the grain (platelet) size increased from 184 to 363 nm when t increased from 200 to 800 nm. All films were deposited at a constant rate of 2.4 nm/s.

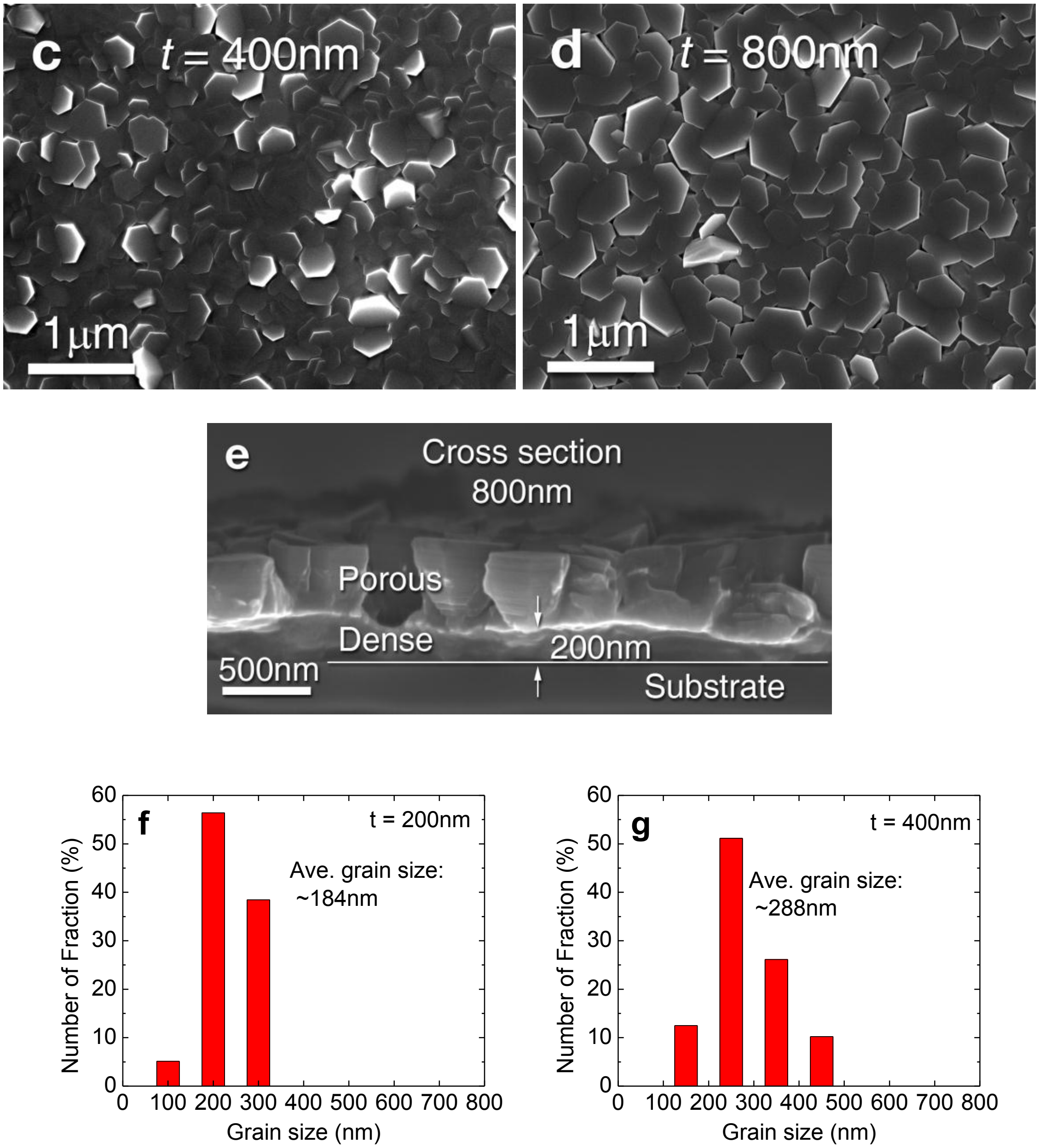

Figure 57. Continued.

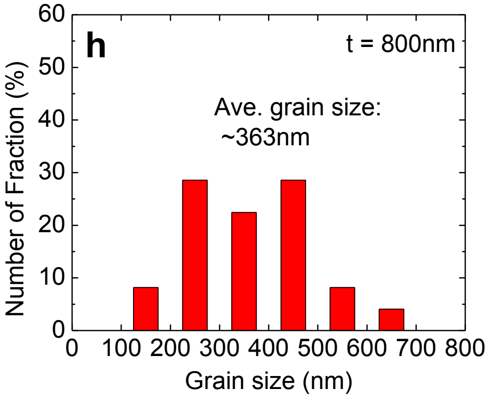

Figure 57. Continued.

Figure 57 shows plan-view SEM (PVSEM) micrographs of Mg films with different layer thickness. All films were DC sputtered on SiO_2 substrates using the standard condition. When t = 50 nm, the film surface was shiny and featureless (not shown here). But when t = 100 nm (Figure 57a) some surface roughness and porosity appeared, and tiny hexagonal plates began to form. When t = 200 nm (Figure 57b) the film surface was still relatively smooth and dense, however the number of hexagonal plates increased rapidly. When t = 400-800 nm (Figure 57c-d), we observed an apparent transition from a mostly dense film to nanoporous films with abundant porosity adjacent to a large number of hexagonal shaped disks (platelets). Cross-section SEM (CSSEM) micrographs for 800 nm thick samples (Figure 57e) revealed an initial ~ 200 nm dense layer followed by porous structure thereafter. The size distributions of these platelets in these DC sputtered films are shown in Figure 57f-h. The hexagonal crystallites size doubled from 184 to 363 nm when t increased from 200 to 800 nm.

VI.4.2 Morphology of Mg films at various deposition rate

PVSEM micrograph from DC sputtered 400 nm thick Mg films fabricated at a deposition rate of 0.6 nm/s is shown in Figure 58a. The image shows randomly distributed hexagonal plates with a large number of nanopores. The average hexagonal plate size was ~ 353 nm (Figure 58b), greater than films deposited by DC sputtering at 2.4 nm/s, ~ 288 nm. Additionally, the lower deposition rate (0.6 nm/s) appeared to result in a less dense structure than films deposited at greater rate (2.4 nm/s).

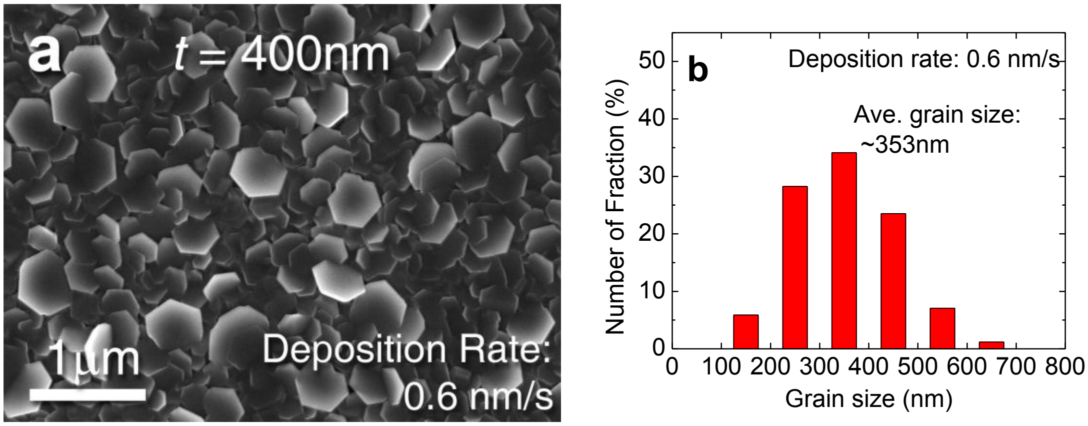

Figure 58. (a) Plane-view SEM micrographs of DC sputtered 400 nm thick Mg films at a deposition rate of 0.6 nm/s. (b) The average grain size is ~ 353 nm, indicating that a lower deposition rate resulted in greater average grain size (compared to Figure 57f). SEM micrographs of (c) DC and (d) RF sputtered Mg (at a rate of 1.6 nm/s) with identical film thickness. RF sputtered Mg shows smooth surface with few hexagonal disks.

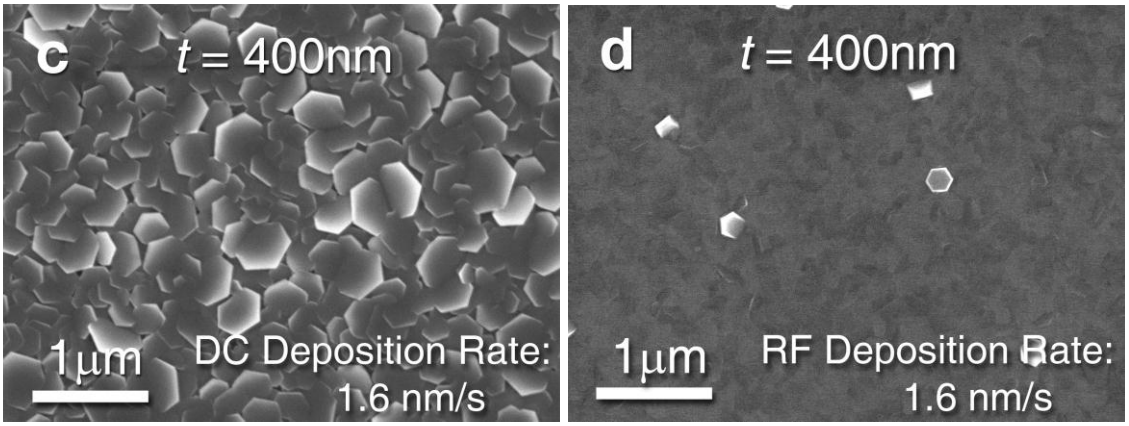

Figure 58. Continued.

VI.4.3 Morphology of DC versus RF sputtered films

Both DC and RF deposition rates were kept the same, 1.6 nm/s. The surface of the RF sputtered film was mirror-like, in drastic contrast to the cloudy surface DC sputtered films shown in Figure 58c. Figure 58d shows PVSEM micrograph of 400 nm thick Mg films prepared by RF sputtering. In contrast to nanoporous films prepared by DC sputtering, the RF-sputtered film exhibited primarily a dense surface decorated by few small hexagonal plates.

VI.4.4 Effects of the substrate type

Figure 59a compares the XRD profiles from 400 nm thick Mg films on SiO_2 and Si (111) substrates. While Mg on SiO_2 exhibits weak (0002) diffraction peak due to its porous structure, Mg on Si (111) showed a strong (0002) fiber texture resulting from the epitaxial growth of Mg. We could not detect any hexagonal plates in SEM micrographs of epitaxial Mg specimens. Figure 59b shows a high resolution TEM (HRTEM) micrograph of Mg deposited on Si (111) substrate examined along $[2\bar{1}\bar{1}0]$ zone axis. Single crystal Mg with (0002) planes parallel to substrate surface was observed. Selected area diffraction (SAD) pattern (Figure 59c) confirms the formation of single crystal Mg films.

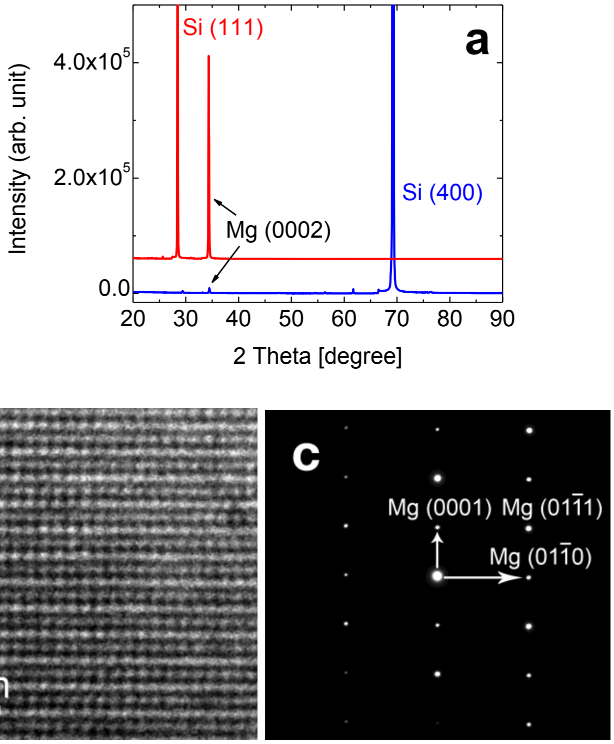

Figure 59. (a) XRD plot of Mg 400 nm film grown on SiO_2 and Si (111) substrates. (0002) Mg grew epitaxially on Si (111) substrate. (b) Cross-section HRTEM micrograph of Mg 400 nm on Si (111) examined along Mg $[2\bar{1}\bar{1}0]$ zone axis confirms the epitaxial growth of (0002) Mg films. (c) SAD pattern of Mg on Si (111) substrate shows single crystal hcp structure along Mg $[2\bar{1}\bar{1}0]$ zone axis.

VI.4.5 Mg pillars on inclined substrates

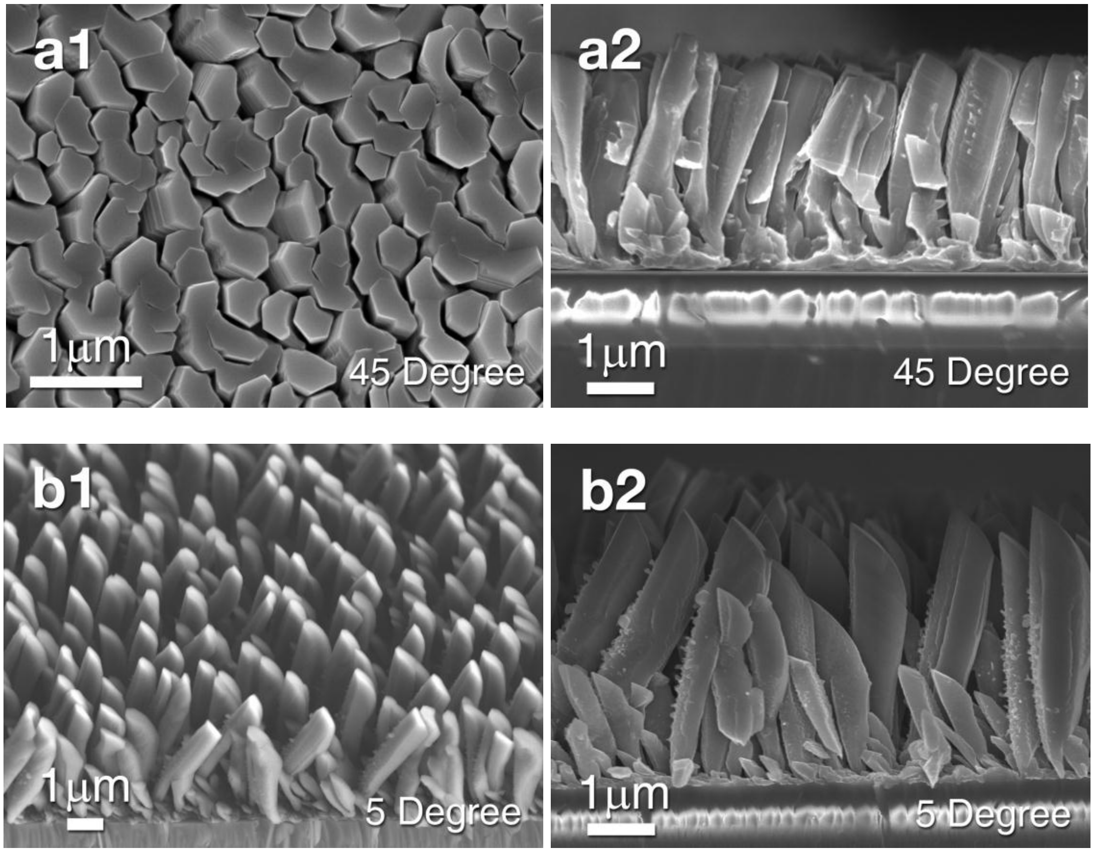

Figure 60. SEM micrographs of Mg pillars prepared by inclined deposition technique. (a1 and a2) A plan-view and cross-section SEM micrograph of Mg pillars grown on Si substrate oriented at 45° during deposition. (b1 and b2) Top-down and cross-section view of Mg pillars deposited on substrate with 5° tilting angle. Compared with Mg 45^{o} pillars, more dispersed sub-micron Mg pillars formed in Mg 5° films.

SiO_2 substrates were placed at 5° and 45° angles with respect to the direction of deposition flux (or central axis of sputter gun, see Figure 55). Figure 60a1 and b1 show the plan (top-down) view SEM images of the resulting Mg pillars. Pillars in the 45° inclined film, shown in Figure 60a1, exhibited hexagonal shapes ranging from 700 to 800 nm in diameter. The flat tops of the columns faced the deposition flux direction (shown in Figure 60a1). The measured angle between the edges of facets was ~ 120° suggesting that most columns have hcp (0002) texture. Figure 60b1 shows Mg film with an inclined deposition angle of 5° and the film formed extremely porous and dispersed nanopillar structures. The CSSEM views (Figure 60a2 and b2) show that the diameter of 45° pillars is relatively uniform from bottom to top of the pillars and the caps of pillars appear mostly flat. However the 5° pillars clearly have greater porosity, much narrower roots and fatter tops, and tops of pillars are significantly tapered.

VI.5 Discussion

VI.5.1 Effects of film thickness, platelet size and deposition rate on morphological evolution of Mg

Films deposited under the standard condition (DC sputtering at a constant rate of 2.4 nm/s) were mostly dense up to approximately 200 nm. Tiny platelets, indications of crystallite irregularity, were occasionally observed when films thickness t = 100 nm. By 200 nm more hexagonal plates formed on surface, although the majority of films appeared dense (featureless) and the platelets grew in size afterward in thicker films. Thicker films have larger platelets and appeared more porous. Mg has an hcp structure and hence the growth of close packed hexagonal (0002) planes is preferred. However, the perfect arrangement of hexagonal facets in one plane (parallel to substrate surface) is increasingly difficult when films grow thicker. Crystallographic error (hexagonal nuclei grows on a plane not parallel to substrate surface) occurred during deposition could be manifested by continuous addition of atoms to the nuclei. Hence one anticipates that larger Mg platelets (occurred in thicker films) may lead to more irregularity of film morphology, or porous Mg films. This is consistent with our experimental observation.

Increasing the deposition power typically results in smaller islands whereas at low deposition power, large crystallites prevail in the film. For films with identical thickness (t = 400 nm), a lower deposition rate (0.6 nm/s in Figure 58b) led to an average platelet size of 353 nm, compared to 288 nm platelets (Figure 57g) deposited at 2.4 nm/s. Such a difference in platelet dimension also led morphology difference. The films deposited at a higher deposition rate appeared to have lower porosity due to the dependence of morphology on platelet size as discussed in forging section.

VI.5.2 Effects of substrate orientation on film morphology and epitaxy.

The cross-section SAD pattern in Figure 59c indicates that Mg (t = 400 nm) on Si (111) substrate retained the single-crystal-like epitaxial structure with (0002) texture. The epitaxial film also has smooth surface. The six fold symmetry of substrate clearly promoted the epitaxial growth and elimination of growth defects (porosity).

The SAD patterns showed the interplanar distance for Mg ($11\bar{2}0$) plane is 3.224 Å, whereas for Si, d_{110} = 3.84 Å. The lattice mismatch strain, ε_m, can be calculated by using [227]:

$$\varepsilon_m = \frac{a_s - a_f}{a_f} \tag{6.1}$$

where a_s and a_f are respective lattice parameter of substrate and film. ε_m is calculated to be ~ 19%. Based on such a large mismatch strain, lattice matching epitaxy appears impossible. However, epitaxial growth can be achieved by domain matching epitaxy [228]. The domain mismatch strain ε_{dme} is estimated by [155]

$$\varepsilon_{dme} = \frac{n a_s - m a_f}{m a_f} \tag{6.2}$$

where n and m as the number of respective substrate and film planes involved in the matching. With a 5Si-to-6Mg domain match, ε_{dme}, is merely 0.7 %, which is small enough to allow domain matching epitaxial growth.

VI.5.3 Drastic morphological difference in films prepared by DC versus RF sputtering

Figure 58c and d show that the RF sputtered film had drastically smoother surface (an indication of lower porosity) than that of DC sputtered films with identical film thickness (t = 400 nm) deposited at the same deposition rate (1.6 nm/s). Our first hypothesis is that there is a large difference in residual stress between DC and RF sputtered films. To investigate the influence of stresses on surface morphology, we performed substrate curvature measurements before and after deposition with a Dektak profilometer. Film stress was calculated by using the Stoney equation [229],

$$\sigma = \frac{E h_{sub}^{2}}{6h}\left(\frac{1}{R_1} - \frac{1}{R_0}\right) \tag{6.3}$$

where σ is film stress, E is biaxial elastic modulus of the substrate, h_{sub} and h are the respective substrate and film thickness, and R_0 and R_1 are the radii of curved substrate before and after deposition. Figure 61 shows that tensile residual stress (solid squares) decreased rapidly with increasing film thickness in DC sputtered films, and reached a plateau when $t \geq 200$ nm. When t is very thin, ~ 100 nm, the development of tensile stress is typically ascribed to nanopores along grain boundaries. At greater film thickness, either grain growth [154, 227] or surface diffusion of atoms to grain boundaries can lead to alleviation of tensile stress [154, 227]. There is of course anomaly when stress-thickness evolution follow different trend as revealed by *in situ* stress measurement during film growth process [212, 230-232]. The occurrence stress plateau at 200 nm may be related to the fact that film stress is drastically reduced by formation of porous Mg when $t > 200$nm. The difference in residual stress between DC and RF sputtered films was insignificant (Figure 61). Thus it is less likely that residual stress plays any significant roles on the drastic different morphology in DC and RF sputtered Mg films.

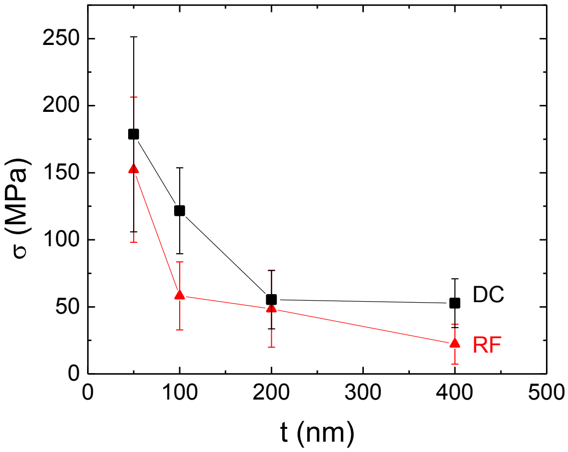

Figure 61. Evolution of residual stress of Mg film prepared by DC and RF sputtering as a function of the film thickness. The magnitude of stresses in both systems was similar and tensile stress decayed continuously to ~ 50 MPa or less when films grew thicker.

The second hypothesis is that the surface morphology difference between DC and RF sputtered films could be related to diffusivity of adatoms during deposition. The rationale behind such a hypothesis is as follows. During RF sputtering, the pulse frequency is 13.56 MHz, corresponding to a pulse width of ~ 0.037 μs. As atoms are only deposited during negative cycle, there could be a maximum of 0.037 μs, during which the adatoms deposited on the surface of substrate (or Mg) can diffuse. If the diffusion distance of adatoms is significant during such a short relaxation time, the probability of crystallographic errors occurred during growth can be significantly reduced, and hence a denser films may be obtained. A key parameter necessary for such an analysis is the surface diffusivity of Mg adatoms. Unfortunately such a parameter which can be obtained either experimentally or theoretically is not yet available to date.

Thus we investigate the diffusivity of Mg adatom on (0001) Mg surface by using first principle calculations based on density functional theory (DFT).

The diffusion coefficient (*D*) can be obtained by the Arrhenius equation:

$$D = D_0 \, \mathrm{e}^{-E_a / k_B T} \tag{6.4}$$

where D_0 is a pre-exponential factor, E_a is the activation energy for diffusion, k_B is the Boltzmann constant, and T is absolute temperature. From the harmonic approximation and within transition state theory, the diffusivity is given by [233, 234]

$$D = \frac{n \nu l^2}{2\alpha} \mathrm{e}^{-(E_{sad} - E_{\min})/k_B T} \tag{6.5}$$

where the activation energy E_a is the difference between the energy of adatom at saddle point (E_{sad}) and at the minimum (stable) point (E_{min}) along the diffusion path (Figure 62), *n* is the number of jump directions available to the adatom, ν is attempt frequency. *l* denotes the jump distance to an adjacent site, and *α* is the dimensionality of the diffusion space. In this study ν is estimated by calculating the vibration frequency of the structure located at the minimum energy point.

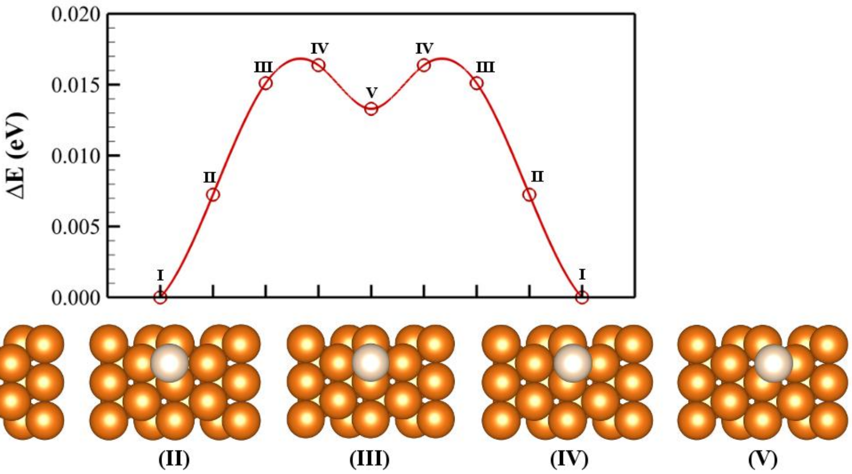

Figure 62. The relative energy profile (ΔE) calculated by using the Nudge elastic band (NEB) method for self-diffusion of a Mg atom (white sphere) on the Mg(0001) surface (orange sphere). The adatom migrates from the fcc-site (I) to the nearest hcp-site (V). Several intermediate steps during diffusion are also shown.

Detailed calculations (methods and results) are summarized in our submitted article. The activation energy E_a along this surface diffusion channel is calculated to be ~ 0.017 eV. This calculated E_a is reasonable comparing to activation energy for self-diffusion on the close packed planes in other metals, in the range of 0.01-0.08 eV [234]. By using v = ~ 3.2×10^{12} s^{-1}, $\alpha = 2$ (for typical surface diffusion), $n = 3$ and $l = 1.8$ Å, D_0 is calculated to be 7.80×10^{10} nm^2/s. Therefore, D is ~ 4.04×10^{10} nm^2/s at 300 K. In bulk diffusion, the total activation energy (including the migration barrier and the formation energy of vacancies) is about two orders of magnitude larger. Consequently, at this temperature, the surface diffusion of Mg is about 18 orders of magnitude faster than self-diffusion in bulk Mg (D = ~ 1×10^{-8} nm^2/s) [235, 236].

During RF sputtering, as there is a maximum of 0.037 μs during which the adatoms deposited on the surface of substrate (or Mg) can diffuse. The diffusion distance, estimated by $x = 2\ (Dt)^{1/2}$, is ~ 106 nm. This is an upper bound estimation since the kinetic energy of sputtered atoms and their arrival time to substrate may have a broad distribution. Consequently the time interval (or deposition gap) that allows atoms to diffuse before the arrival of next batch of atoms is much shorter. Assuming that the deposition gap is merely 1-2% of 0.037 μs, the surface diffusion distance for Mg atoms is 1-2 nm, which may be still substantial to allow Mg adatoms to identify crystallographically correct lattice positions. Consequently RF sputtered Mg films have very smooth surface and much lower porosity. Of course a more comprehensive analytical model considering the dynamics of sputtered atoms and plasmas may be necessary to accurately probe the nature of RF sputtering and its impact on morphology of sputtered Mg films.

VI.5.4 The influence of inclination angle on morphology of Mg nanopillars

Foregoing studies focused on the impact of various parameters on porosity of Mg films. Extremely porous Mg films in form of nanopillars were formed by glancing angle deposition. This setup often results in the growth of nanowires or rods [237-245]. In this study the spacing among Mg pillars was greater when deposition angle was reduced from 45 to 5^{o}. During glancing angle deposition, inclined substrate will have a prominent ballistic shadowing effect [241, 246]. The majority of new atoms will be deposited on the existing nuclei leaving shadowed area uncovered. Continuous addition of adatoms to nuclei led to the formation of Mg pillars, which were tilted toward the incident flux. When substrate was oriented at 45^{o}, the disparity between flux at root and on top of pillar is insignificant, and thus the diameter of pillar is relatively uniform from base to top (Figure 60a2). In contrast glancing angle deposition of pillars at 5^{o} showed a much narrower root than top of Mg pillars, implying a significant shadowing effect. Due to the low melting point of Mg (T_m = 600 °C), diameter of pillars varies from 700 to 800 nm, which is larger than that in Cr pillars, ~ 100 nm, deposited at room temperature (T_m = 1900 °C) [238]. The wide columns imply that the diffusion length of adatoms in Mg is greater than that in metals with higher melting temperature.

VI.6 Conclusions

Mg films were deposited by magnetron sputtering under various conditions. Thinner Mg films with smaller grains showed uniform and nearly fully dense microstructure, while thicker films (t > 200 nm) with larger grains developed porous surfaces with randomly oriented hexagonal platelets. Mg films (t = 400 nm) deposited by RF sputtering showed mirror like surfaces and dense structure. First principle calculations showed that the diffusion distance during relaxation in RF sputtering process is sufficiently large to remove growth defects and reduce film porosity. Single crystal Mg films grew epitaxially on Si (111) substrate by domain matching epitaxy and had no porosity. Glancing angle deposition led to the formation Mg nanopillars.

CHAPTER VII

CONCLUSION

The microstructure and mechanical behavior of sputter-deposited Mg/Nb multilayer films were investigated and the hardness of Mg/Nb was compared to those of Mg and Cu/Nb and Al/Nb multilayer systems. A metastable structure of bcc Mg at the interface was revealed in Mg/Nb 5 nm multilayers. The interface barrier strength computed from the Hall-Petch slope shows interphase interfaces in Mg/Nb provide a strong barrier to slip transmission. The peak hardness of the multilayers, estimated from H-P model and Koehler stress, is in good agreement with experimental data, and is greater than the hardness of most other Mg and Mg alloys reported to date.

The drastic destabilization of Mg hydride induced by an orthorhombic phase opens up abundant opportunity for the selection of appropriate second phases to design and manufacturing Mg nanocomposites with advanced H storage performance. The destabilization is triggered by the formation of distorted metastable O-MgH_2 phases induced by stress. Stresses arise from either substrate constraint or volume expansion incompatibility. O-MgH_2 is preferred over T-MgH_2 because it induces less lattice distortion crystallographically during phase transformation. Density functional theory (DFT) calculations agree qualitatively with experimental observations. Size effect and layer interface also play an important role to expedite the H sorption kinetics in MgH_2. These studies provide important design criteria for selection of an appropriate second phase to destabilize Mg hydride. The concept of stress-assisted H-sorption developed here also has general implications for the design of other metal hydrides and chemical hydrides.

We explored the hydrogen storage performance of porous and dense Mg films prepared by magnetron sputtering under various conditions. Thinner dense Mg films (t = 200 nm) have a lower hydrogen desorption temperature than their thicker porous counterparts film (t > 200 nm). Mg 45° pillar films also show improved hydrogen sorption performance compared to the more porous 5° pillar films. Stress arising from a rigid substrate during hydrogenation of Mg films plays a critical role to induce metastable orthorhombic Mg hydride that can easily desorb H_2 at low temperatures. The stress concept validated via numerous experiments could have general implications on destabilization of other types of metal hydrides for H_2 storage application.

Mg films were deposited by magnetron sputtering under various conditions. Thinner Mg films with smaller grains showed uniform and nearly fully dense microstructures, while thicker films (t > 200 nm) with larger grains developed porous surfaces with randomly oriented hexagonal platelets. Mg films (t = 400 nm) deposited by RF sputtering showed mirror like surfaces and dense structure. First principle calculations show that the diffusion distance during relaxation in the RF sputtering process is sufficiently large to remove growth defects and reduce film porosity. Single crystal Mg films grew epitaxially on Si (111) substrate by domain matching epitaxy and had no porosity. Glancing angle deposition led to the formation Mg nanopillars.

REFERENCES

[1] L. Schlapbach, A. Zuttel, Hydrogen-storage materials for mobile applications, Nature, 414 (2001) 353-358.

[2] A. Züttel, Materials for hydrogen storage, Materials Today, 6 (2003) 24-33.

[3] C. Weidenthaler, M. Felderhoff, Solid-state hydrogen storage for mobile applications: Quo Vadis?, Energy & Environmental Science, 4 (2011) 2495-2502.

[4] R. Bardhan, A.M. Ruminski, A. Brand, J.J. Urban, Magnesium nanocrystal-polymer composites: A new platform for designer hydrogen storage materials, Energy & Environmental Science, 4 (2011) 4882-4895.

[5] R. von Helmolt, U. Eberle, Fuel cell vehicles: Status 2007, Journal of Power Sources, 165 (2007) 833-843.

[6] U. Eberle, M. Felderhoff, F. Schüth, Chemical and Physical Solutions for Hydrogen Storage, Angewandte Chemie International Edition, 48 (2009) 6608-6630.

[7] Bruce Gain, Road testing BMW's hydrogen 7, www.wired.com, 2006 [cited 2013 Nov], Available from: http://www.wired.com/cars/energy/news/2006/11/72100?currentPage=1.

[8] J.S. Zhang, T.S. Fisher, R. P.V., G. J.P., M. I., A review of heat transfer issues in hydrogen storage technologies, ASME J. Heat Transfer, 127 (2005) 1391-1399.

[9] M. Felderhoff, C. Weidenthaler, R. von Helmolt, U. Eberle, Hydrogen storage: the remaining scientific and technological challenges, Physical Chemistry Chemical Physics, 9 (2007) 2643-2653.

[10] D.S. Lee, D.H. Shin, D.U. Lee, J.C. Kim, H.S. Cheigh, The use of physical carbon dioxide absorbents to control pressure buildup and volume expansion of kimchi packages, Journal of Food Engineering, 48 (2001) 183-188.

[11] J. Weitkamp, M. Fritz, S. Ernst, Zeolites as media for hydrogen storage, International Journal of Hydrogen Energy, 20 (1995) 967-970.

[12] S.H. Jhung, J.W. Yoon, J.S. Lee, J.-S. Chang, Low-Temperature Adsorption/Storage of Hydrogen on FAU, MFI, and MOR Zeolites with Various Si/Al Ratios: Effect of Electrostatic Fields and Pore Structures, Chemistry – A European Journal, 13 (2007) 6502-6507.

[13] H.W. Langmi, A. Walton, M.M. Al-Mamouri, S.R. Johnson, D. Book, J.D. Speight, P.P. Edwards, I. Gameson, P.A. Anderson, I.R. Harris, Hydrogen adsorption in zeolites A, X, Y and RHO, Journal of Alloys and Compounds, 356–357 (2003) 710-715.

[14] A. Corma, M.J. Diaz-Cabanas, J.L. Jorda, C. Martinez, M. Moliner, High-throughput synthesis and catalytic properties of a molecular sieve with 18- and 10-member rings, Nature, 443 (2006) 842-845.

[15] A. Chambers, C. Park, R.T.K. Baker, N.M. Rodriguez, Hydrogen Storage in Graphite Nanofibers, The Journal of Physical Chemistry B, 102 (1998) 4253-4256.

[16] L.J. Murray, M. Dinca, J.R. Long, Hydrogen storage in metal-organic frameworks, Chemical Society Reviews, 38 (2009) 1294-1314.

[17] Tony Boehle, Large pore of MOF-5 with yellow ball, Wikimedia, 2010 [cited 2013 Nov], Available from: http://en.wikipedia.org/wiki/Metal-organic_framework.

[18] N.L. Rosi, J. Eckert, M. Eddaoudi, D.T. Vodak, J. Kim, M. O'Keeffe, O.M. Yaghi, Hydrogen Storage in Microporous Metal-Organic Frameworks, Science, 300 (2003) 1127-1129.

[19] O.M. Yaghi, M. O'Keeffe, N.W. Ockwig, H.K. Chae, M. Eddaoudi, J. Kim, Reticular synthesis and the design of new materials, Nature, 423 (2003) 705-714.

[20] H. Li, M. Eddaoudi, M. O'Keeffe, O.M. Yaghi, Design and synthesis of an exceptionally stable and highly porous metal-organic framework, Nature, 402 (1999) 276-279.

[21] S.S.-Y. Chui, S.M.-F. Lo, J.P.H. Charmant, A.G. Orpen, I.D. Williams, A Chemically Functionalizable Nanoporous Material [Cu3(TMA)2(H2O)3]n, Science, 283 (1999) 1148-1150.

[22] A.U. Czaja, N. Trukhan, U. Muller, Industrial applications of metal-organic frameworks, Chemical Society Reviews, 38 (2009) 1284-1293.

[23] B.C. Hauback, H.W. Brinks, C.M. Jensen, K. Murphy, A.J. Maeland, Neutron diffraction structure determination of NaAlD4, Journal of Alloys and Compounds, 358 (2003) 142-145.

[24] B. Bogdanović, R.A. Brand, A. Marjanović, M. Schwickardi, J. Tölle, Metal-doped sodium aluminium hydrides as potential new hydrogen storage materials, Journal of Alloys and Compounds, 302 (2000) 36-58.

[25] B. Bogdanović, M. Schwickardi, Ti-doped alkali metal aluminium hydrides as potential novel reversible hydrogen storage materials, Journal of Alloys and Compounds, 253–254 (1997) 1-9.

[26] L. Zaluski, A. Zaluska, J.O. Ström-Olsen, Hydrogenation properties of complex alkali metal hydrides fabricated by mechano-chemical synthesis, Journal of Alloys and Compounds, 290 (1999) 71-78.

[27] J. Huot, G. Liang, R. Schulz, Mechanically alloyed metal hydride systems, Applied Physics A, 72 (2001) 187-195.

[28] C.M. Jensen, R. Zidan, N. Mariels, A. Hee, C. Hagen, Advanced titanium doping of sodium aluminum hydride: - segue to a practical hydrogen storage material?, International Journal of Hydrogen Energy, 24 (1999) 461-465.

[29] B. Bogdanović, M. Felderhoff, A. Pommerin, F. Schüth, N. Spielkamp, Advanced Hydrogen-Storage Materials Based on Sc-, Ce-, and Pr-Doped NaAlH4, Advanced Materials, 18 (2006) 1198-1201.

[30] M. Fichtner, O. Fuhr, O. Kircher, Magnesium alanate—a material for reversible hydrogen storage?, Journal of Alloys and Compounds, 356–357 (2003) 418-422.

[31] M. Fichtner, J. Engel, O. Fuhr, A. Glöss, O. Rubner, R. Ahlrichs, The Structure of Magnesium Alanate, Inorganic Chemistry, 42 (2003) 7060-7066.

[32] S.-i. Orimo, Y. Nakamori, J.R. Eliseo, A. Zuettel, C.M. Jensen, Complex Hydrides for Hydrogen Storage, Chemical Reviews, 107 (2007) 4111-4132.

[33] J.H.N. van Vucht, F.A. Kuijpers, H.C.A.M. Bruning, Reversible room-temperature absorption of large quantities of hydrogen by intermetallic compounds, Philips Research Reports, 25(1970) 133-140.

[34] B. Sakintuna, F. Lamari-Darkrim, M. Hirscher, Metal hydride materials for solid hydrogen storage: A review, International Journal of Hydrogen Energy, 32 (2007) 1121-1140.

[35] F. Cuevas, J.M. Joubert, M. Latroche, A. Percheron-Guégan, Intermetallic compounds as negative electrodes of Ni/MH batteries, Applied Physics A, 72 (2001) 225-238.

[36] T. Yamamoto, H. Inui, M. Yamaguchi, Deformation of LaNi5 by uniaxial compression and hydrogenation, Intermetallics, 9 (2001) 987-991.

[37] K.-F. Aguey-Zinsou, J.-R. Ares-Fernandez, Hydrogen in magnesium: new perspectives toward functional stores, Energy & Environmental Science, 3 (2010) 526-543.

[38] G. Barkhordarian, T. Klassen, R. Bormann, Effect of Nb2O5 content on hydrogen reaction kinetics of Mg, Journal of Alloys and Compounds, 364 (2004) 242-246.

[39] Ben Mills, Magnesium Hydride, Wikimedia, 2008 [cited 2013 Nov], Magnesium hydride schematic, Available from: http://en.wikipedia.org/wiki/File:Magnesium-hydride-unit-cell-3D-balls.png.

[40] T. Moriwaki, Y. Akahama, H. Kawamura, S. Nakano, K. Takemura, Structural Phase Transition of Rutile-Type MgH_2 at High Pressures, Journal of the Physical Society of Japan, 75 (2006) 074603.

[41] J.S. Han, M. Pezat, L. Jai-Young, A study of the decomposition of magnesium hydride by thermal analysis, Journal of the Less Common Metals, 130 (1987) 395-402.

[42] M. Stioui, A. Grayevsky, A. Resnik, D. Shaltiel, N. Kaplan, Macroscopic and microscopic kinetics of hydrogen in magnesium-rich compounds, Journal of the Less Common Metals, 123 (1986) 9-24.

[43] M. Dornheim, S. Doppiu, G. Barkhordarian, U. Boesenberg, T. Klassen, O. Gutfleisch, R. Bormann, Hydrogen storage in magnesium-based hydrides and hydride composites, Scripta Materialia, 56 (2007) 841-846.

[44] R.W.P. Wagemans, J.H. van Lenthe, P.E. de Jongh, A.J. van Dillen, K.P. de Jong, Hydrogen Storage in Magnesium Clusters: Quantum Chemical Study, Journal of the American Chemical Society, 127 (2005) 16675-16680.

[45] M. Khrussanova, M. Terzieva, P. Peshev, I. Konstanchuk, E. Ivanov, Hydriding Kinetics of Mixtures Containing Some 3d-Transition Metal Oxides and Magnesium*, Zeitschrift für Physikalische Chemie, 164 (1989) 1261-1266.

[46] B. Bogdanović, K. Bohmhammel, B. Christ, A. Reiser, K. Schlichte, R. Vehlen, U. Wolf, Thermodynamic investigation of the magnesium–hydrogen system, Journal of Alloys and Compounds, 282 (1999) 84-92.

[47] K. Bohmhammel, U. Wolf, G. Wolf, E. Königsberger, Thermodynamic optimization of the system magnesium–hydrogen, Thermochimica Acta, 337 (1999) 195-199.

[48] L. Berlouis, E. Cabrera, E. Hall-Barientos, P. Hall, S. Dodd, S. Morris, M. Imam, Thermal analysis investigation of hydriding properties of nanocrystalline Mg–Ni-and

Mg–Fe-based alloys prepared by high-energy ball milling, J. Mater. Res, 16 (2001) 45-57.

[49] J. Huot, G. Liang, S. Boily, A. Van Neste, R. Schulz, Structural study and hydrogen sorption kinetics of ball-milled magnesium hydride, Journal of Alloys and Compounds, 293–295 (1999) 495-500.

[50] J. Huot, G. Liang, R. Schulz, Mechanically alloyed metal hydride systems, Applied Physics A: Materials Science & Processing, 72 (2001) 187-195.

[51] R. Schwarz, Hydrogen Storage in Magnesium-Based Alloys, MRS Bulletin, 24 (1999) 40-44.

[52] J. Huot, E. Akiba, T. Takada, Mechanical alloying of Mg・Ni compounds under hydrogen and inert atmosphere, Journal of Alloys and Compounds, 231 (1995) 815-819.

[53] M. Fichtner, Nanotechnological Aspects in Materials for Hydrogen Storage, Advanced Engineering Materials, 7 (2005) 443-455.

[54] N. Hanada, T. Ichikawa, H. Fujii, Catalytic effect of Ni nano-particle and Nb oxide on H-desorption properties in MgH_2 prepared by ball milling, Journal of Alloys and Compounds, 404-406 (2005) 716-719.

[55] C.X. Shang, M. Bououdina, Y. Song, Z.X. Guo, Mechanical alloying and electronic simulations of (MgH_2+M) systems (M=Al, Ti, Fe, Ni, Cu and Nb) for hydrogen storage, International Journal of Hydrogen Energy, 29 (2004) 73-80.

[56] B. Bogdanović, T.H. Hartwig, B. Spliethoff, The development, testing and optimization of energy storage materials based on the MgH_2-Mg system, International Journal of Hydrogen Energy, 18 (1993) 575-589.

[57] J.J. Reilly, R.H. Wiswall, Reaction of hydrogen with alloys of magnesium and nickel and the formation of Mg2NiH4, Inorganic Chemistry, 7 (1968) 2254-2256.

[58] R.L. Holtz, M.A. Imam, Hydrogen storage characteristics of ball-milled magnesium-nickel and magnesium-iron alloys, Journal of Materials Science, 34 (1999) 2655-2663.

[59] I.P. Jain, C. Lal, A. Jain, Hydrogen storage in Mg: A most promising material, International Journal of Hydrogen Energy, 35 (2010) 5133-5144.

[60] A. Andreasen, Hydrogenation properties of Mg–Al alloys, International Journal of Hydrogen Energy, 33 (2008) 7489-7497.

[61] J. Huot, J.F. Pelletier, L.B. Lurio, M. Sutton, R. Schulz, Investigation of dehydrogenation mechanism of MgH2–Nb nanocomposites, Journal of Alloys and Compounds, 348 (2003) 319-324.

[62] Y. Zhang, Y. Tsushio, H. Enoki, E. Akiba, The study on binary Mg-Co hydrogen storage alloys with BCC phase, J Alloys Compd, 393 (2005) 7-7.

[63] J.J. Vajo, W. Li, P. Liu, ChemInform Abstract: Thermodynamic and Kinetic Destabilization in $LiBH_4/Mg_2NiH_4$: Promise for Borohydride-Based Hydrogen Storage, Chemical Communications, 46 (2010) 6687-6689.

[64] W. Li, J.J. Vajo, R.W. Cumberland, P. Liu, S.-J. Hwang, C. Kim, R.C. Bowman, Hydrogenation of Magnesium Nickel Boride for Reversible Hydrogen Storage, The Journal of Physical Chemistry Letters, 1 (2009) 69-72.

[65] J.J. Vajo, G.L. Olson, Hydrogen storage in destabilized chemical systems, Scripta Materialia, 56 (2007) 829-834.

[66] G. Liang, Synthesis and hydrogen storage properties of Mg-based alloys, Journal of Alloys and Compounds, 370 (2004) 123-128.

[67] V.V. Bhat, A. Rougier, L. Aymard, G.A. Nazri, J.M. Tarascon, High surface area niobium oxides as catalysts for improved hydrogen sorption properties of ball milled MgH2, Journal of Alloys and Compounds, 460 (2008) 507-512.

[68] Z. Dehouche, T. Klassen, W. Oelerich, J. Goyette, T.K. Bose, R. Schulz, Cycling and thermal stability of nanostructured MgH2–Cr2O3 composite for hydrogen storage, Journal of Alloys and Compounds, 347 (2002) 319-323.

[69] J. Qu, Y. Wang, L. Xie, J. Zheng, Y. Liu, X. Li, Hydrogen absorption–desorption, optical transmission properties and annealing effect of Mg thin films prepared by magnetron sputtering, International Journal of Hydrogen Energy, 34 (2009) 1910-1915.

[70] H. Fujii, K. Higuchi, K. Yamamoto, H. Kajioka, S. Orimo, K. Toiyama, Remarkable hydrogen storage, structural and optical properties in multi-layered Pd/Mg thin films, Materials Transactions, 43 (2002) 2721-2727.

[71] S. Bouhtiyya, L. Roué, Pd/Mg/Pd thin films prepared by pulsed laser deposition under different helium pressures: Structure and electrochemical hydriding properties, International Journal of Hydrogen Energy, 34 (2009) 5778-5784.

[72] J. Qu, Y. Wang, L. Xie, J. Zheng, Y. Liu, X. Li, Superior hydrogen absorption and desorption behavior of Mg thin films, Journal of Power Sources, 186 (2009) 515-520.

[73] A. Remhof, A. Borgschulte, Thin-Film Metal Hydrides, ChemPhysChem, 9 (2008) 2440-2455.

[74] C.J. Chung, S.-C. Lee, J.R. Groves, E.N. Brower, R. Sinclair, B.M. Clemens, Interfacial Alloy Hydride Destabilization in Mg/Pd Thin Films, Physical Review Letters, 108 (2012) 106102.

[75] N. Hanada, T. Ichikawa, H. Fujii, Catalytic Effect of Nanoparticle 3d-Transition Metals on Hydrogen Storage Properties in Magnesium Hydride MgH2 Prepared by Mechanical Milling, The Journal of Physical Chemistry B, 109 (2005) 7188-7194.

[76] G. Liang, J. Huot, S. Boily, A. Van Neste, R. Schulz, Catalytic effect of transition metals on hydrogen sorption in nanocrystalline ball milled MgH2–Tm (Tm=Ti, V, Mn, Fe and Ni) systems, Journal of Alloys and Compounds, 292 (1999) 247-252.

[77] M. Pozzo, D. Alfè, Hydrogen dissociation and diffusion on transition metal (=Ti, Zr, V, Fe, Ru, Co, Rh, Ni, Pd, Cu, Ag)-doped Mg(0001) surfaces, International Journal of Hydrogen Energy, 34 (2009) 1922-1930.

[78] M. Pasturel, M. Slaman, H. Schreuders, J.H. Rector, D.M. Borsa, B. Dam, R. Griessen, Hydrogen absorption kinetics and optical properties of Pd-doped Mg thin films, Journal of Applied Physics, 100 (2006) 023515-023515-023518.

[79] R. Gremaud, A. Borgschulte, C. Chacon, J.L.M. van Mechelen, H. Schreuders, A. Züttel, B. Hjörvarsson, B. Dam, R. Griessen, Structural and optical properties of MgxAl1-xHy gradient thin films: a combinatorial approach, Applied Physics A, 84 (2006) 77-85.

[80] T.J. Richardson, J.L. Slack, R.D. Armitage, R. Kostecki, B. Farangis, M.D. Rubin, Switchable mirrors based on nickel--magnesium films, Applied Physics Letters, 78 (2001) 3047-3049.

[81] R.A.H. Niessen, P.H.L. Notten, Electrochemical Hydrogen Storage Characteristics of Thin Film MgX (X = Sc , Ti , V , Cr) Compounds, Electrochemical and Solid-State Letters, 8 (2005) A534-A538.

[82] Á.S. Ingason, A.K. Eriksson, S. Ólafsson, Hydrogen uptake in Mg:C thin films, Journal of Alloys and Compounds, 446-447 (2007) 530-533.

[83] B. Zahiri, B.S. Amirkhiz, D. Mitlin, Hydrogen storage cycling of MgH_2 thin film nanocomposites catalyzed by bimetallic Cr Ti, Applied Physics Letters, 97 (2010) 083106-083103.

[84] A. Baldi, R. Gremaud, D.M. Borsa, C.P. Baldé, A.M.J. van der Eerden, G.L. Kruijtzer, P.E. de Jongh, B. Dam, R. Griessen, Nanoscale composition modulations in MgyTi$_{1-y}$H$_x$ thin film alloys for hydrogen storage, International Journal of Hydrogen Energy, 34 (2009) 1450-1457.

[85] D.M. Borsa, R. Gremaud, A. Baldi, H. Schreuders, J.H. Rector, B. Kooi, P. Vermeulen, P.H.L. Notten, B. Dam, R. Griessen, Structural, optical, and electrical properties of $Mg_yTi_{1-y}H_x$ thin films, Physical Review B, 75 (2007) 205408.

[86] A. Baldi, M. Gonzalez-Silveira, V. Palmisano, B. Dam, R. Griessen, Destabilization of the Mg-H System through Elastic Constraints, Physical Review Letters, 102 (2009) 226102.

[87] X. Tan, L. Wang, C.M.B. Holt, B. Zahiri, M.H. Eikerling, D. Mitlin, Body centered cubic magnesium niobium hydride with facile room temperature absorption and four weight percent reversible capacity, Physical Chemistry Chemical Physics, 14 (2012) 10904-10909.

[88] R. Gremaud, C.P. Broedersz, D.M. Borsa, A. Borgschulte, P. Mauron, H. Schreuders, J.H. Rector, B. Dam, R. Griessen, Hydrogenography: An Optical Combinatorial Method To Find New Light-Weight Hydrogen-Storage Materials, Advanced Materials, 19 (2007) 2813-2817.

[89] Q. Zheng, Y. Pivak, L.P.A. Mooij, A.M.J. van der Eerden, H. Schreuders, P.E. de Jongh, J.H. Bitter, B. Dam, EXAFS investigation of the destabilization of the Mg–Ni–Ti (H) system, International Journal of Hydrogen Energy, 37 (2012) 4161-4169.

[90] X. Tan, M. Danaie, W.P. Kalisvaart, D. Mitlin, The influence of Cu substitution on the hydrogen sorption properties of magnesium rich Mg-Ni films, International Journal of Hydrogen Energy, 36 (2011) 2154-2164.

[91] L. Yu, W. Gwo-Ching, Air stability of low-temperature dehydrogenation of Pd-decorated Mg blades, Nanotechnology, 23 (2012) 025401.

[92] C. Harrower, E. Poirier, H. Fritzsche, P. Kalisvaart, S. Satija, B. Akgun, D. Mitlin, Early deuteration steps of Pd- and Ta/Pd- catalyzed Mg70Al30 thin films observed at room temperature, International Journal of Hydrogen Energy, 35 (2010) 10343-10348.

[93] E. Poirier, C.T. Harrower, P. Kalisvaart, A. Bird, A. Teichert, D. Wallacher, N. Grimm, R. Steitz, D. Mitlin, H. Fritzsche, Deuterium absorption in Mg70Al30 thin films with bilayer catalysts: A comparative neutron reflectometry study, Journal of Alloys and Compounds, 509 (2011) 5466-5471.

[94] H. Fritzsche, W.P. Kalisvaart, B. Zahiri, R. Flacau, D. Mitlin, The catalytic effect of Fe and Cr on hydrogen and deuterium absorption in Mg thin films, International Journal of Hydrogen Energy, 37 (2012) 3540-3547.

[95] W.P. Kalisvaart, E.J. Luber, E. Poirier, C.T. Harrower, A. Teichert, D. Wallacher, N. Grimm, R. Steitz, H. Fritzsche, D. Mitlin, Probing the Room Temperature Deuterium Absorption Kinetics in Nanoscale Magnesium Based Hydrogen Storage Multilayers Using Neutron Reflectometry, X-ray Diffraction, and Atomic Force Microscopy, The Journal of Physical Chemistry C, 116 (2012) 5868-5880.

[96] P. Kalisvaart, E. Luber, H. Fritzsche, D. Mitlin, Effect of alloying magnesium with chromium and vanadium on hydrogenation kinetics studied with neutron reflectometry, Chemical Communications, 47 (2011) 4294-4296.

[97] A. Baldi, D.M. Borsa, H. Schreuders, J.H. Rector, T. Atmakidis, M. Bakker, H.A. Zondag, W.G.J. van Helden, B. Dam, R. Griessen, Mg–Ti–H thin films as switchable solar absorbers, International Journal of Hydrogen Energy, 33 (2008) 3188-3192.

[98] M. Slaman, B. Dam, M. Pasturel, D.M. Borsa, H. Schreuders, J.H. Rector, R. Griessen, Fiber optic hydrogen detectors containing Mg-based metal hydrides, Sensors and Actuators B: Chemical, 123 (2007) 538-545.

[99] M. Slaman, B. Dam, H. Schreuders, R. Griessen, Optimization of Mg-based fiber optic hydrogen detectors by alloying the catalyst, International Journal of Hydrogen Energy, 33 (2008) 1084-1089.

[100] S. Bao, Y. Yamada, M. Okada, K. Yoshimura, The effect of polymer coatings on switching behavior and cycling durability of Pd/Mg-Ni thin films, Applied Surface Science, 253 (2007) 6268-6272.

[101] K. Yoshimura, Y. Yamada, S. Bao, K. Tajima, M. Okada, Degradation of switchable mirror based on Mg-Ni alloy thin film, Japanese Journal of Applied Physics, Part 1: Regular Papers and Short Notes and Review Papers, 46 (2007) 4260-4264.

[102] S. Bao, K. Tajima, Y. Yamada, M. Okada, K. Yoshimura, Color-neutral switchable mirrors based on magnesium-titanium thin films, Applied Physics A, 87 (2007) 621-624.

[103] H. Wang, L.Z. Ouyang, M.Q. Zeng, M. Zhu, Hydrogen sorption properties of Mg/Mm–Ni multi-layer film prepared by thermal evaporation, Journal of Alloys and Compounds, 375 (2004) 313-317.

[104] H. Wang, L. Ouyang, M. Zeng, M. Zhu, Microstructure and hydrogen sorption properties of Mg–Ni/MmM5 multi-layer film by magnetron sputtering, International Journal of Hydrogen Energy, 29 (2004) 1389-1392.

[105] A. Baldi, V. Palmisano, M. Gonzalez-Silveira, Y. Pivak, M. Slaman, H. Schreuders, B. Dam, R. Griessen, Quasifree Mg--H thin films, Applied Physics Letters, 95 (2009) 071903-071903.

[106] A. Baldi, G.K. Pálsson, M. Gonzalez-Silveira, H. Schreuders, M. Slaman, J.H. Rector, G. Krishnan, B.J. Kooi, G.S. Walker, M.W. Fay, B. Hjörvarsson, R.J. Wijngaarden, B. Dam, R. Griessen, Mg/Ti multilayers: Structural and hydrogen absorption properties, Physical Review B, 81 (2010) 224203.

[107] L.Z. Ouyang, H. Wang, C.Y. Chung, J.H. Ahn, M. Zhu, MgNi/Pd multilayer hydrogen storage thin films prepared by dc magnetron sputtering, Journal of Alloys and Compounds, 422 (2006) 58-61.

[108] Y. Wang, W. Hua, J. Qu, L. Xie, X. Li, Structure changes and optical properties of Mg2Ni switchable mirrors, International Journal of Hydrogen Energy, 33 (2008) 7207-7213.

[109] R. Domènech-Ferrer, M. Gurusamy Sridharan, G. Garcia, F. Pi, J. Rodríguez-Viejo, Hydrogenation properties of pure magnesium and magnesium–aluminium thin films, Journal of Power Sources, 169 (2007) 117-122.

[110] H. Fujii, S.-i. Orimo, Hydrogen storage properties in nano-structured magnesium- and carbon-related materials, Physica B: Condensed Matter, 328 (2003) 77-80.

[111] W.P. Kalisvaart, A. Kubis, M. Danaie, B.S. Amirkhiz, D. Mitlin, Microstructural evolution during hydrogen sorption cycling of Mg–FeTi nanolayered composites, Acta Materialia, 59 (2011) 2083-2095.

[112] L.Z. Ouyang, H. Wang, M. Zhu, J. Zou, C.Y. Chung, Microstructure of MmM_5/Mg multi-layer films prepared by magnetron sputtering, Journal of Alloys and Compounds, 404-406 (2005) 485-489.

[113] J. Paillier, S. Bouhtiyya, G.G. Ross, L. Roué, Influence of the deposition atmosphere on the characteristics of Pd–Mg thin films prepared by pulsed laser deposition, Thin Solid Films, 500 (2006) 117-123.

[114] R. Zahiri, B. Zahiri, A. Kubis, P. Kalisvaart, B. Shalchi Amirkhiz, D. Mitlin, Microstructural evolution during low temperature sorption cycling of Mg-AlTi multilayer nanocomposites, International Journal of Hydrogen Energy, 37 (2012) 4215-4226.

[115] M. Zhu, H. Wang, L.Z. Ouyang, M.Q. Zeng, Composite structure and hydrogen storage properties in Mg-base alloys, International Journal of Hydrogen Energy, 31 (2006) 251-257.

[116] M. Dornheim, A. Pundt, R. Kirchheim, S.J. v. d. Molen, E.S. Kooij, J. Kerssemakers, R. Griessen, H. Harms, U. Geyer, Stress development in thin yttrium films on hard substrates during hydrogen loading, Journal of Applied Physics, 93 (2003) 8958-8965.

[117] A. Pundt, R. Kirchheim, Hydrogen in metals: Microstructural Aspects, Annual Review of Materials Research, 36 (2006) 555-608.

[118] Y. Pivak, R. Gremaud, K. Gross, M. Gonzalez-Silveira, A. Walton, D. Book, H. Schreuders, B. Dam, R. Griessen, Effect of the substrate on the thermodynamic properties of PdH_x films studied by hydrogenography, Scripta Materialia, 60 (2009) 348-351.

[119] A. Misra, J.P. Hirth, H. Kung, Single-dislocation-based strengthening mechanisms in nanoscale metallic multilayers, Philosophical Magazine A, 82 (2002) 2935-2951.

[120] X. Zhang, A. Misra, H. Wang, T.D. Shen, M. Nastasi, T.E. Mitchell, J.P. Hirth, R.G. Hoagland, J.D. Embury, Enhanced hardening in Cu/330 stainless steel multilayers by nanoscale twinning, Acta Materialia, 52 (2004) 995-1002.

[121] X. Zhang, A. Misra, Residual stresses in sputter-deposited copper/330 stainless steel multilayers, Journal of Applied Physics, 96 (2004) 7173-7178.

[122] B.M. Clemens, H. Kung, S.A. Barnett, Structure and strength of multilayers, Mrs Bulletin, 24 (1999) 20-26.

[123] A. Misra, J.P. Hirth, R.G. Hoagland, Length-scale-dependent deformation mechanisms in incoherent metallic multilayered composites, Acta Materialia, 53 (2005) 4817-4824.

[124] G.S. Was, T. Foecke, Deformation and fracture in microlaminates, Thin Solid Films, 286 (1996) 1-31.

[125] A. Misra, J.P. Hirth, H. Kung, Single-dislocation-based strengthening mechanisms in nanoscale metallic multilayers, Philosophical Magazine a-Physics of Condensed Matter Structure Defects and Mechanical Properties, 82 (2002) 2935-2951.

[126] A. Misra, M. Verdier, Y.C. Lu, H. Kung, T.E. Mitchell, M. Nastasi, J.D. Embury, Structure and mechanical properties of Cu-X (X = Nb,Cr,Ni) nanolayered composites, Scripta Materialia, 39 (1998) 555-560.

[127] A. Misra, J. Hirth, R. Hoagland, J. Embury, H. Kung, Dislocation mechanisms and symmetric slip in rolled nano-scale metallic multilayers, Acta Materialia, 52 (2004) 2387-2394.

[128] A. Misra, H. Kung, J. Embury, Preface to the viewpoint set on: deformation and stability of nanoscale metallic multilayers, Scripta Materialia, 50 (2004) 707-710.

[129] J. McKeown, A. Misra, H. Kung, R. Hoagland, M. Nastasi, Microstructures and strength of nanoscale Cu–Ag multilayers, Scripta Materialia, 46 (2002) 593-598.

[130] R.G. Hoagland, R.J. Kurtz, C. Henager Jr, Slip resistance of interfaces and the strength of metallic multilayer composites, Scripta Materialia, 50 (2004) 775-779.

[131] A. Misra, H. Krug, Deformation behavior of nanostructured metallic multilayers, Advanced Engineering Materials, 3 (2001) 217-222.

[132] A. Misra, J. Hirth, R. Hoagland, Length-scale-dependent deformation mechanisms in incoherent metallic multilayered composites, Acta Materialia, 53 (2005) 4817-4824.

[133] A. Misra, M. Verdier, H. Kung, J. Embury, J. Hirth, Deformation mechanism maps for polycrystalline metallic multilayers, Scripta Materialia, 41 (1999).

[134] A. Misra, R. Hoagland, Plastic flow stability of metallic nanolaminate composites, Journal of Materials Science, 42 (2007) 1765-1771.

[135] W.D. Nix, H. Gao, Indentation size effects in crystalline materials: a law for strain gradient plasticity, Journal of the Mechanics and Physics of Solids, 46 (1998) 411-425.

[136] P.M. Anderson, C. Li, Hall-Petch relations for multilayered materials, Nanostructured Materials, 5 (1995) 349-362.

[137] J.S. Koehler, Attempt to Design a Strong Solid, Physical Review B, 2 (1970) 547-551.

[138] S.I. Rao, P.M. Hazzledine, Atomistic simulations of dislocation-interface interactions in the Cu-Ni multilayer system, Philosophical Magazine A, 80 (2000) 2011-2040.

[139] K.O. Schweitz, J. Chevallier, J. B∅ttiger, W. Matz, N. Schell, Hardness in Ag/Ni, Au/Ni and Cu/Ni multilayers, Philosophical Magazine A, 81 (2001) 2021-2032.

[140] R.G. Hoagland, J.P. Hirth, A. Misra, On the role of weak interfaces in blocking slip in nanoscale layered composites, Philosophical Magazine, 86 (2006) 3537-3558.

[141] S.A. Dregia, R. Banerjee, H.L. Fraser, Polymorphic phase stability in thin multilayers, Scripta Materialia, 39 (1998) 217-223.

[142] A.F. Jankowski, M.A. Wall, Formation of face-centered cubic titanium on a Ni single crystal and in Ni/Ti multilayers, Journal of Materials Research, 9 (1994) 31-38.

[143] X. Zhang, M.F. Hundley, A. Malinowski, A. Misra, H. Wang, M. Nastasi, Microstructure and electronic properties of Cu/Mo multilayers and three-dimensional arrays of nanocrystalline Cu precipitates embedded in a Mo matrix, Journal of Applied Physics, 95 (2004) 3644-3648.

[144] H. Kung, Y.C. Lu, A. J. Griffin, Jr., M. Nastasi, T.E. Mitchell, J.D. Embury, Observation of body centered cubic Cu in Cu/Nb nanolayered composites, Applied Physics Letters, 71 (1997) 2103-2105.

[145] P. Anderson, T. Foecke, P. Hazzledine, Dislocation-based deformation mechanisms in metallic nanolaminates, MRS Bulletin-Materials Research Society, 24 (1999) 27-33.

[146] P. Anderson, C. Li, Hall-Petch relations for multilayered materials, Nanostructured materials, 5 (1995) 349-362.

[147] J.P. Hirth, J. Lothe, Theory of Dislocations, 2nd ed., Wiley, New York, 1982.

[148] M.A. Phillips, B.M. Clemens, W.D. Nix, A model for dislocation behavior during deformation of Al/Al3Sc (fcc/L12) metallic multilayers, Acta Materialia, 51 (2003) 3157-3170.

[149] J.D. Embury, J.P. Hirth, On dislocation storage and the mechanical response of fine scale microstructures, Acta Metallurgica et Materialia, 42 (1994) 2051-2056.

[150] M. Shinn, L. Hultman, S.A. Barnett, Growth, structure, and microhardness of epitaxial TiN/NbN superlattices, Journal of Materials Research, 7 (1992) 901-911.

[151] J.A. Thornton, The microstructure of sputter-deposited coatings, Journal of Vacuum Science & Technology A: Vacuum, Surfaces, and Films, 4 (1986) 3059-3065.

[152] J.A. Venables, G.D.T. Spiller, M. Hanbucken, Nucleation and growth of thin films, Reports on Progress in Physics, 47 (1984) 399.

[153] C. Thompson, Structure evolution during processing of polycrystalline films, Annual review of materials science, 30 (2000) 159-190.

[154] M. Ohring, The materials Science of Thin films, Academic Press, San Diego, 2002.

[155] J. Narayan, B.C. Larson, Domain epitaxy: A unified paradigm for thin film growth, Journal of Applied Physics, 93 (2003) 278-285.

[156] Y.J. Liu, H.Y. Chu, Y.P. Zhao, Silver Nanorod Array Substrates Fabricated by Oblique Angle Deposition: Morphological, Optical, and SERS Characterizations, The Journal of Physical Chemistry C, 114 (2010) 8176-8183.

[157] M.M. Hawkeye, M.J. Brett, Glancing angle deposition: Fabrication, properties, and applications of micro-and nanostructured thin films, Journal of Vacuum Science & Technology A: Vacuum, Surfaces, and Films, 25 (2007) 1317-1335.

[158] M.F. Cansizoglu, R. Engelken, H.-W. Seo, T. Karabacak, High Optical Absorption of Indium Sulfide Nanorod Arrays Formed by Glancing Angle Deposition, ACS Nano, 4 (2010) 733-740.

[159] A. Yamashita, Z. Horita, T.G. Langdon, Improving the mechanical properties of magnesium and a magnesium alloy through severe plastic deformation, Materials Science and Engineering A, 300 (2001) 142-147.

[160] H.Q. Sun, Y.N. Shi, M.X. Zhang, K. Lu, Plastic strain-induced grain refinement in the nanometer scale in a Mg alloy, Acta Materialia, 55 (2007) 975-982.

[161] K. Wu, H. Chang, E. Maawad, W.M. Gan, H.G. Brokmeier, M.Y. Zheng, Microstructure and mechanical properties of the Mg/Al laminated composite fabricated by accumulative roll bonding (ARB), Materials Science and Engineering: A, 527 3073-3078.

[162] X. Chu, S.A. Barnett, Model of superlattice yield stress and hardness enhancements, Journal of Applied Physics, 77 (1995) 4403-4411.

[163] W.C. Oliver, G.M. Pharr, Improved technique for determining hardness and elastic modulus using load and displacement sensing indentation experiments, Journal of Materials Research, 7 (1992) 1564-1583.

[164] N. Ono, R. Nowak, S. Miura, Effect of deformation temperature on Hall-Petch relationship registered for polycrystalline magnesium, Materials Letters, 58 (2004) 39-43.

[165] W.M. Gan, M.Y. Zheng, H. Chang, X.J. Wang, X.G. Qiao, K. Wu, B. Schwebke, H.G. Brokmeier, Microstructure and tensile property of the ECAPed pure magnesium, Journal of Alloys and Compounds, 470 (2009) 256-262.

[166] I.K. Schuller, New Class of Layered Materials, Physical Review Letters, 44 (1980) 1597.

[167] E.E. Fullerton, I.K. Schuller, H. Vanderstraeten, Y. Bruynseraede, Structural refinement of superlattices from x-ray diffraction, Physical Review B, 45 (1992) 9292.

[168] N. Li, K.Y. Yu, J. Lee, H. Wang, X. Zhang, Size dependent strengthening mechanisms in sputtered Fe/W multilayers, Journal of Applied Physics, 107 093503.

[169] C. Kim, S.B. Qadri, M.R. Scanlon, R.C. Cammarata, Low-dimension structural properties and microindentation studies of ion-beam-sputtered multilayers of Ag/Al films, Thin Solid Films, 240 (1994) 52-55.

[170] E.G. Fu, N. Li, A. Misra, R.G. Hoagland, H. Wang, X. Zhang, Mechanical properties of sputtered Cu/V and Al/Nb multilayer films, Materials Science and Engineering: A, 493 (2008) 283-287.

[171] R. Banerjee, S.A. Dregia, H.L. Fraser, Stability of f.c.c. titanium in titanium/aluminum multilayers, Acta Materialia, 47 (1999) 4225-4231.

[172] J.G. Sevillano, R. Cahn, P. Hassen, E. Kramer, Materials Science and Technology, a Comprehensive Treatment, vol. 6VCH, Weinheim, New York, 1993.

[173] M. Mata, M. Anglada, J. Alcalá, Contact deformation regimes around sharp indentations and the concept of the characteristic strain, Journal of Materials Research, 17 (2002) 964-976.

[174] Basic Research Needs for the Hydrogen Economy. Report of the Basic Energy Sciences Workshop on Hydrogen Production, Storage and Use: Department of Energy, 2003.

[175] W. Grochala, P.P. Edwards, Thermal Decomposition of the Non-Interstitial Hydrides for the Storage and Production of Hydrogen, Chemical Reviews, 104 (2004) 1283-1315.

[176] D. Pukazhselvan, V. Kumar, S.K. Singh, High capacity hydrogen storage: Basic aspects, new developments and milestones, Nano Energy, 1 (2012) 566-589.

[177] B. Bogdanović, A. Ritter, B. Spliethoff, Active MgH2-Mg Systems for Reversible Chemical Energy Storage, Angewandte Chemie International Edition in English, 29 (1990) 223-234.

[178] H. Shao, G. Xin, J. Zheng, X. Li, E. Akiba, Nanotechnology in Mg-based materials for hydrogen storage, Nano Energy, 1 (2012) 590-601.

[179] J.S. Han, M. Pezat, J.-Y. Lee, A study of the decomposition of magnesium hydride by thermal analysis, Journal of the Less Common Metals, 130 (1987) 395-402.

[180] D.R. Petersen, H.W. Rinn, A new phase in the zinc-zirconium system, Acta Crystallographica, 14 (1961) 328-329.

[181] J. Renner, H.J. Grabke, Determination of Diffusion Coefficients in the Hydriding of Alloys, Zeitschrift fuer Metallkunde, 69 (1978) 639-642.

[182] M. Stioui, A. Grayevsky, A. Resnik, D. Shaltiel, N. Kaplan, Macroscopic and microscopic kinetics of hydrogen in magnesium-rich compounds, Journal of the Less Common Metals, 123 (1986) 9-24.

[183] M. Fichtner, Properties of nanoscale metal hydrides, Nanotechnology, 20 (2009) 204009.

[184] A. Pundt, Hydrogen in Nano-sized Metals, Advanced Engineering Materials, 6 (2004) 11-21.

[185] A.S. Arico, P. Bruce, B. Scrosati, J.-M. Tarascon, W. van Schalkwijk, Nanostructured materials for advanced energy conversion and storage devices, Nature Materials, 4 (2005) 366-377.

[186] A. Baldi, B. Dam, Thin film metal hydrides for hydrogen storage applications, Journal of Materials Chemistry, 21 (2011) 4021-4026.

[187] R. Gremaud, J.L.M. van Mechelen, H. Schreuders, M. Slaman, B. Dam, R. Griessen, Structural and optical properties of $Mg_yNi_{1-y}H_x$ gradient thin films in relation to the as-deposited metallic state, International Journal of Hydrogen Energy, 34 (2009) 8951-8957.

[188] D.M. Borsa, A. Baldi, M. Pasturel, H. Schreuders, B. Dam, R. Griessen, P. Vermeulen, P.H.L. Notten, Mg--Ti--H thin films for smart solar collectors, Applied Physics Letters, 88 (2006) 241910-241913.

[189] X. Tan, B. Zahiri, C.M.B. Holt, A. Kubis, D. Mitlin, A TEM based study of the microstructure during room temperature and low temperature hydrogen storage cycling in MgH_2 promoted by Nb–V, Acta Materialia, 60 (2012) 5646-5661.

[190] B. Zahiri, M. Danaie, X. Tan, B.S. Amirkhiz, G.A. Botton, D. Mitlin, Stable Hydrogen Storage Cycling in Magnesium Hydride, in the Range of Room Temperature to 300 °C, Achieved Using a New Bimetallic Cr-V Nanoscale Catalyst, The Journal of Physical Chemistry C, 116 (2011) 3188-3199.

[191] L.G. Parratt, Surface Studies of Solids by Total Reflection of X-Rays, Physical Review, 95 (1954) 359-369.

[192] T.P. Russell, The Characterization of Polymer Interfaces, Annual Review of Materials Science, 21 (1991) 249-268.

[193] T.P. Russell, On the reflectivity of polymers: Neutrons and X-rays, Physica B: Condensed Matter, 221 (1996) 267-283.

[194] T. Schober, The niobium-hydrogen system – an electron microscope study. I. Room temperature results, physica status solidi (a), 29 (1975) 395-406.

[195] B. Paik, I.P. Jones, A. Walton, V. Mann, D. Book, I.R. Harris, $MgH_2 \rightarrow Mg$ phase transformation driven by a high-energy electron beam: An in situ transmission electron microscopy study, Philosophical Magazine Letters, 90 (2010) 1-7.

[196] P. Vajeeston, P. Ravindran, A. Kjekshus, H. Fjellvåg, Pressure-Induced Structural Transitions in MgH_2, Physical Review Letters, 89 (2002) 175506.

[197] W. Kraus, G. Nolze, POWDER CELL - a program for the representation and manipulation of crystal structures and calculation of the resulting X-ray powder patterns, Journal of Applied Crystallography, 29 (1996) 301-303.

[198] H. Peisl, Lattice strains due to hydrogen in metals, Hydrogen in Metals I, in: G. Alefeld, J. Völkl (Eds.), Springer Berlin / Heidelberg, 1978, pp. 53-74.

[199] P. Mengucci, G. Barucca, G. Majni, N. Bazzanella, R. Checchetto, A. Miotello, Structure modification of Mg–Nb films under hydrogen sorption cycles, Journal of Alloys and Compounds, 509, Supplement 2 (2011) S572-S575.

[200] L. Schlapbach, P. Fischer, R. Bowman, Hydrogen in Intermetallic Compounds-I, Springer-Verlag, 1988.

[201] I.P. Jain, Y.K. Vijay, L.K. Malhotra, K.S. Uppadhyay, Hydrogen storage in thin film metal hydride—a review, International Journal of Hydrogen Energy, 13 (1988) 15-23.

[202] G. Barkhordarian, T. Klassen, R. Bormann, Catalytic Mechanism of Transition-Metal Compounds on Mg Hydrogen Sorption Reaction, The Journal of Physical Chemistry B, 110 (2006) 11020-11024.

[203] A. Zaluska, L. Zaluski, J.O. Ström–Olsen, Nanocrystalline magnesium for hydrogen storage, Journal of Alloys and Compounds, 288 (1999) 217-225.

[204] K.F. Aguey-Zinsou, J.R. Ares Fernandez, T. Klassen, R. Bormann, Effect of Nb2O5 on MgH2 properties during mechanical milling, International Journal of Hydrogen Energy, 32 (2007) 2400-2407.

[205] S.V. Alapati, J.K. Johnson, D.S. Sholl, Identification of Destabilized Metal Hydrides for Hydrogen Storage Using First Principles Calculations, The Journal of Physical Chemistry B, 110 (2006) 8769-8776.

[206] J.J. Vajo, T.T. Salguero, A.F. Gross, S.L. Skeith, G.L. Olson, Thermodynamic destabilization and reaction kinetics in light metal hydride systems, Journal of Alloys and Compounds, 446 (2007) 409-414.

[207] B. Ham, A. Junkaew, R. Arroyave, J. Chen, H. Wang, P. Wang, J. Majewski, J. Park, H.C. Zhou, R.K. Arvapally, U. Kaipa, M.A. Omary, X.Y. Zhang, Y. Ren, X. Zhang, Hydrogen sorption in orthorhombic Mg hydride at ultra-low temperature, International Journal of Hydrogen Energy, (2013).

[208] B. Ham, X. Zhang, High strength Mg/Nb nanolayer composites, Materials Science and Engineering: A, 528 (2011) 2028-2033.

[209] A. Junkaew, B. Ham, X. Zhang, A. Talapatra, R. Arróyave, REPORT: Stabilization of bcc Mg in Thin Films at Ambient Pressure: Experimental Evidence and ab initio Calculations, Materials Research Letters, (2013) 1-7.

[210] G. Simmons, H. Wang, Single crystal elastic constants and calculated aggregate properties: A handbook, MIT Press (Cambridge, Mass), 1971.

[211] F. Tang, T. Parker, H.F. Li, G.C. Wang, T.M. Lu, The Pd catalyst effect on low temperature hydrogen desorption from hydrided ultrathin Mg nanoblades, Nanotechnology, 19 (2008) 465706.

[212] W. Li, C. Li, H. Ma, J. Chen, Magnesium Nanowires: Enhanced Kinetics for Hydrogen Absorption and Desorption, Journal of the American Chemical Society, 129 (2007) 6710-6711.

[213] K. Zhang, C. Rossi, C. Tenailleau, P. Alphonse, Aligned three-dimensional prismlike magnesium nanostructures realized onto silicon substrate, Applied Physics Letters, 92 (2008) 063123-063123.

[214] J. Erlebacher, M.J. Aziz, A. Karma, N. Dimitrov, K. Sieradzki, Evolution of nanoporosity in dealloying, Nature, 410 (2001) 450-453.

[215] C. Ji, P.C. Searson, Synthesis and Characterization of Nanoporous Gold Nanowires, The Journal of Physical Chemistry B, 107 (2003) 4494-4499.

[216] S. Parida, D. Kramer, C.A. Volkert, H. Rösner, J. Erlebacher, J. Weissmüller, Volume Change during the Formation of Nanoporous Gold by Dealloying, Physical Review Letters, 97 (2006) 035504.

[217] S.E. Skrabalak, J. Chen, Y. Sun, X. Lu, L. Au, C.M. Cobley, Y. Xia, Gold Nanocages: Synthesis, Properties, and Applications, Accounts of Chemical Research, 41 (2008) 1587-1595.

[218] D. Kramer, R.N. Viswanath, J. Weissmüller, Surface-Stress Induced Macroscopic Bending of Nanoporous Gold Cantilevers, Nano Letters, 4 (2004) 793-796.

[219] Z. Zhang, Y. Wang, Z. Qi, W. Zhang, J. Qin, J. Frenzel, Generalized Fabrication of Nanoporous Metals (Au, Pd, Pt, Ag, and Cu) through Chemical Dealloying, The Journal of Physical Chemistry C, 113 (2009) 12629-12636.

[220] Y. Li, Y.-Y. Song, C. Yang, X.-H. Xia, Hydrogen bubble dynamic template synthesis of porous gold for nonenzymatic electrochemical detection of glucose, Electrochemistry Communications, 9 (2007) 981-988.

[221] V. Zielasek, B. Jürgens, C. Schulz, J. Biener, M.M. Biener, A.V. Hamza, M. Bäumer, Gold Catalysts: Nanoporous Gold Foams, Angewandte Chemie International Edition, 45 (2006) 8241-8244.

[222] X. Zhang, A. Misra, H. Wang, A.L. Lima, M.F. Hundley, R.G. Hoagland, Effects of deposition parameters on residual stresses, hardness and electrical resistivity of nanoscale twinned 330 stainless steel thin films, Journal of Applied Physics, 97 (2005) 094302-094305.

[223] O. Kluth, G. Schöpe, B. Rech, R. Menner, M. Oertel, K. Orgassa, H. Werner Schock, Comparative material study on RF and DC magnetron sputtered ZnO:Al films, Thin Solid Films, 502 (2006) 311-316.

[224] R. Cremer, M. Witthaut, D. Neuschütz, G. Erkens, T. Leyendecker, M. Feldhege, Comparative characterization of alumina coatings deposited by RF, DC and pulsed reactive magnetron sputtering, Surface and Coatings Technology, 120–121 (1999) 213-218.

[225] H. Hoche, C. Pusch, R. Riedel, C. Fasel, A. Klein, Properties of SiCN coatings for high temperature applications — Comparison of RF-, DC- and HPPMS-sputtering, Surface and Coatings Technology, 205, Supplement 1 (2010) S21-S27.

[226] Z. Zhang, C. Bao, W. Yao, S. Ma, L. Zhang, S. Hou, Influence of deposition temperature on the crystallinity of Al-doped ZnO thin films at glass substrates prepared by RF magnetron sputtering method, Superlattices and Microstructures, 49 (2011) 644-653.

[227] L. Freund, S. Suresh, Thin film materials: stress, defect formation, and surface evolution, Cambridge University Press, Cambridge, England, 2009.

[228] H. Wang, A. Tiwari, A. Kvit, X. Zhang, J. Narayan, Epitaxial growth of TaN thin films on Si(100) and Si(111) using a TiN buffer layer, Applied Physics Letters, 80 (2002) 2323-2325.

[229] G.G. Stoney, Proceedings of the Royal Society A, Mathematical, Physical and Engineering Sciences, London, United-Kingdom, (1909) 172.

[230] S. Hearne, E. Chason, J. Han, J.A. Floro, J. Figiel, J. Hunter, H. Amano, I.S.T. Tsong, Stress evolution during metalorganic chemical vapor deposition of GaN, Applied Physics Letters, 74 (1999) 356-358.

[231] A.L. Shull, F. Spaepen, Measurements of stress during vapor deposition of copper and silver thin films and multilayers, Journal of Applied Physics, 80 (1996) 6243-6256.

[232] C. Friesen, C.V. Thompson, Reversible Stress Relaxation during Precoalescence Interruptions of Volmer-Weber Thin Film Growth, Physical Review Letters, 89 (2002) 126103.

[233] A.F. Voter, J.D. Doll, Surface self-diffusion constants at low temperature: Monte Carlo transition state theory with importance sampling, American Institute of Physics, Melville, NY, ETATS-UNIS, 1984.

[234] C.L. Liu, J.M. Cohen, J.B. Adams, A.F. Voter, EAM study of surface self-diffusion of single adatoms of fcc metals Ni, Cu, Al, Ag, Au, Pd, and Pt, Surface Science, 253 (1991) 334-344.

[235] J. Combronde, G. Brebec, Anisotropy for self diffusion in magnesium Acta Metallurgica, 19 (1971) 1393-1399.

[236] S. Ganeshan, L.G. Hector Jr, Z.K. Liu, First-principles study of self-diffusion in hcp Mg and Zn, Computational Materials Science, 50 (2010) 301-307.

[237] M.M. Hawkeye, M.J. Brett, Glancing angle deposition: Fabrication, properties, and applications of micro- and nanostructured thin films, Journal of Vacuum Science & Technology A: Vacuum, Surfaces, and Films, 25 (2007) 1317-1335.

[238] D. Vick, L.J. Friedrich, S.K. Dew, M.J. Brett, K. Robbie, M. Seto, T. Smy, Self-shadowing and surface diffusion effects in obliquely deposited thin films, Thin Solid Films, 339 (1999) 88-94.

[239] J.D. Torre, G.H. Gilmer, D.L. Windt, R. Kalyanaraman, F.H. Baumann, P.L. O'Sullivan, J. Sapjeta, T.D. de la Rubia, M.D. Rouhani, Microstructure of thin tantalum films sputtered onto inclined substrates: Experiments and atomistic simulations, Journal of Applied Physics, 94 (2003) 263-271.

[240] M. Suzuki, K. Nagai, S. Kinoshita, K. Nakajima, K. Kimura, T. Okano, K. Sasakawa, Vapor phase growth of Al whiskers induced by glancing angle deposition at high temperature, Applied Physics Letters, 89 (2006) 133103-133103.

[241] K. Robbie, M.J. Brett, Sculptured thin films and glancing angle deposition: Growth mechanics and applications, Journal of Vacuum Science & Technology A: Vacuum, Surfaces, and Films, 15 (1997) 1460-1465.

[242] M. Malac, R.F. Egerton, Observations of the microscopic growth mechanism of pillars and helices formed by glancing-angle thin-film deposition, Journal of Vacuum Science & Technology A: Vacuum, Surfaces, and Films, 19 (2001) 158-166.

[243] M.O. Jensen, M.J. Brett, Periodically structured glancing angle deposition thin films, Nanotechnology, IEEE Transactions on, 4 (2005) 269-277.

[244] P.C.P. Hrudey, K.L. Westra, M.J. Brett, Highly Ordered Organic Alq3 Chiral Luminescent Thin Films Fabricated by Glancing-Angle Deposition, Advanced Materials, 18 (2006) 224-228.

[245] A.G. Dirks, H.J. Leamy, Columnar microstructure in vapor-deposited thin films, Thin Solid Films, 47 (1977) 219-233.

[246] Z. Dohnálek, G.A. Kimmel, D.E. McCready, J.S. Young, A. Dohnálková, R.S. Smith, B.D. Kay, Structural and Chemical Characterization of Aligned Crystalline Nanoporous MgO Films Grown via Reactive Ballistic Deposition, The Journal of Physical Chemistry B, 106 (2002) 3526-3529.